2012

High-Sensitivity Temperature-Independent Silicon Photonic Microfluidic Biosensors

Kangbaek Kim
Lehigh University

High-Sensitivity Temperature-Independent Silicon Photonic Microfluidic Biosensors

by

Kangbaek Kim

Presented to the Graduate and Research Committee

of Lehigh University

in Candidacy for the Degree of

Doctor of Philosophy

in

Electrical Engineering

Lehigh University

May 2012

This dissertation is accepted and approved in partial fulfillment of the requirements for the Degree of Doctor of Philosophy.

_____
Date

_____
Prof. Thomas L. Koch (Dissertation Director)

_____
Accepted Date

Committee Members:

_____
Prof. Thomas L. Koch (Chairman and Advisor)

_____
Prof. Yujie Ding

_____
Prof. Ivan Biaggio

_____
Prof. Dmitri Vezenov

Acknowledgments

I wish to express my gratitude to my advisor Prof. Thomas L. Koch for his support, inspiration, and guidance during my Ph.D. research at Lehigh University. I am happy that I was able to achieve many pioneering results in biophotonics field with Prof. Koch. I would also like to appreciate the members of my doctoral committee, Prof. Yujie Ding, Ivan Biaggio, and Dmitri Vezenov for their advice.

All the works presented in this dissertation would not have been possible without support and collaboration from Dr. Robert M. Pafchek and Dr. Ravi S. Tummidi. The biosensor is a beautiful collaboration between optical engineering and biology. Without help and advice in biomolecular science and surface functionalization from Prof. Dmitri Vezenov and Dr. Piercen M. Oliver, I could not have achieved the results presented here. I would also like to acknowledge the assistance of Prof. James F. Gilchrist in helping us develop the PDMS microfluidic fabrication used in our biosensor evaluation.

I wish to also offer my thanks to all members of the Center for Optical Technologies (COT) past five years for priceless discussion and assistance. Many thanks to Dr. Chee-loon Tan, Dr. Vitchanetra Hongpinyo, Dr. Yun-Hsiang Ding, and Anthony Jeffers, and especially to Anne Nierer for her support making me focus on my research.

I also wish to express my gratitude to Prof. Dong-Soo Shin at Hanyang University who encouraged me to study in the United States and gave me heart advice. He was a trigger that made me stand here.

Finally, I also owe thanks to the support of the National Science Foundation under Grant No. ECCS-0824082, and to the Commonwealth of Pennsylvania Ben Franklin Technology Authority for partial support of the projects reported here

To my wife

Olivia H. Park

Table of Contents

List of Figures

Abstract

Optical biosensors that can precisely quantify the presence of specific molecular species in real time without the need for labeling have seen increased use in in the drug discovery industry and molecular biology in general. Of the many possible optical biosensors, the TM mode Si biosensor is shown to be very attractive in the sensing application because of large field amplitude on the surface and cost effective CMOS VLSI fabrication.

Noise is the most fundamental factor that limits the performance of sensors in development of high-sensitivity biosensors, and noise reduction techniques require precise studies and analysis. One such example stems from thermal fluctuations. Generally SOI biosensors are vulnerable to ambient temperature fluctuations because of large thermo-optic coefficient of silicon (~2×10^{-4} RIU/K), typically requiring another reference ring and readout sequence to compensate temperature induced noise. To address this problem, we designed sensors with a novel TM-mode shallow-ridge waveguide that provides both large surface amplitude for bulk and surface sensing. With proper design, this also provides large optical confinement in the aqueous cladding that renders the device athermal using the negative thermo-optic coefficient of water (~ -1×10^{-4} RIU/K), demonstrating cancellation of thermo-optic effects for aqueous solution operation near 300K.

Additional limitations resulting from mechanical actuator fluctuations, stability of tunable lasers, and large *1/f* noise of lasers and sensor electronics can limit biosensor performance.

Here we also present a simple harmonic feedback readout technique that obviates the need for spectrometers and tunable lasers. This feedback technique reduces the impact of *1/f* noise to enable high-sensitivity, and a DSP lock-in with 256 kHz sampling rate can provide down to μs time scale monitoring for fast transitions in biomolecular concentration with potential for small volume and low cost.

In this dissertation, a novel high-sensitivity, athermal biosensor on a TM-mode SOI resonator was designed, fabricated, and evaluated High-performance biosensing for bulk and surface detection limits of 1×10^{-7} RIU and 24 fg/mm^2 was demonstrated.

Chapter 1

Introduction

1.1 Motivation

Dramatic development of molecular chemistry and biology has been a compelling driving force of demands for analytical diagnostic apparatus to characterize molecular interactions, with higher throughput or/and lower sample consumption [1], [2]. In Figure 1.1 the global market for biosensors is forecast to reach $12 billion by 2015 [3] with their vast application area such as biomedical research, healthcare, pharmaceuticals, environmental monitoring, homeland security, and battlefield [1]-[4].

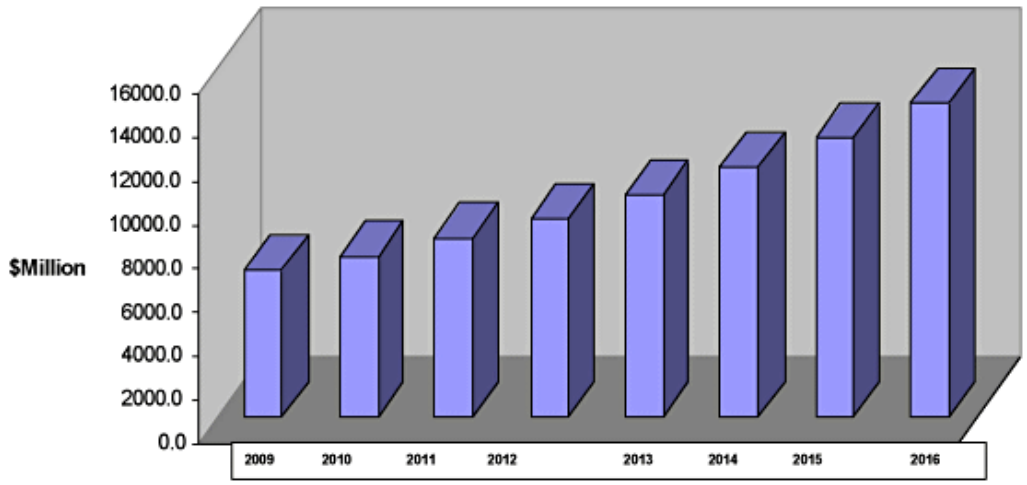

Figure 1.1. The total biosensors market showing the world revenue forecast [3]

One of big potential markets is diabetic sensors [5]. Over the past decade the prevalence of type 2 diabetes has increased dramatically and is still increasing, and World Health Organization (WHO) predicted that diabetic patients worldwide will increase up to 350 million people by 2030, which is double the current number [6]. Reflecting these concerns, the social interest in diabetes and demands for diagnostics and treatments are increasing.

In detection of complex interaction between antibody and antigen quantitatively and accurately, biosensors have huge therapeutic potential [1], [2], [7]. However it is difficult to sense small molecular interactions [8], such as drug compounds which are usually less than 500 Dalton molecular weight because of small affinity and interaction area, and this motivates the development of very highly sensitive methods [9].

Recent reports on biosensors show outstanding performance [8], [10], [12] but optical biosensors show several advantages: robustness to vibration, compact device size, and insensitivity to electromagnetic interference with excellent performance down to single molecule detection [11], [12]. In particular, label-free detection techniques draw more attention because target molecules are detected in their natural forms; instead the sensor surface is modified to bind with target molecules [1], [2], [4], [8], [12], [13]. These label-free techniques provide opportunities to explore biomolecular interactions without unwanted side effects of labeling techniques such as spatial-interference, autofluorescent, or quenching effects [4], [13].

High-density and high-yield CMOS VLSI technology with to the capability of achieving deep submicron feature sizes (0.5 μm and below) allows for progress toward higher speed and lower power consumption [14], [15]. A CMOS process compatible silicon-on-insulator (SOI) waveguide technologies promises optoelectronic integrated circuits that encompass optical and electronic functions together on a small-scale silicon chip at a low cost [15], [16]. The advantageous use of SOI waveguide technology on a CMOS process for evanescent wave chemical and biological sensing of both thin adsorbed biomolecular layers and bulk homogeneous solutions has been firmly established following the pioneering work of Densmore, *et al.*[17]. In particular, SOI was shown to provide an order of magnitude increase in sensitivity compared to other material systems [17]. This allows for high-performance interferometric sensors using folded Mach-Zehnder and ring resonator configurations, and practical, low detection limit devices have already been demonstrated [18]-[20]. The increased sensitivity resulting from the electric field amplitude jump upon entering the low-index cladding in transverse magnetic (TM) operation has been previously documented [17]. SOI wafers provide very tight vertical confinement of optical power in the waveguide due to the large refractive index difference ($\Delta n \approx 2$) between Si core and buried-oxide (BOX) cladding, and enable low loss and compact optical components to be fabricated. The large Δn also maximizes the sensitivity of waveguides to the small perturbation of refractive index in cladding when we use TM mode. Optimally utilizing this effect requires the use of thin layer shallow-ridge TM guides carefully designed at “magic widths” to avoid fundamental leakage to

lateral transverse electric (TE) radiation modes [21]. It is widely acknowledged that the scattering loss from side-wall roughness is a dominant loss in optical devices, and scales in magnitude as $(\Delta n)^2$ where Δn is the index difference between the two media [22]. We minimize scattering loss by etching the silicon field only 13 nm with additional oxidation process, and this waveguide geometry leaves room for electrical access for photonic integration with active devices.

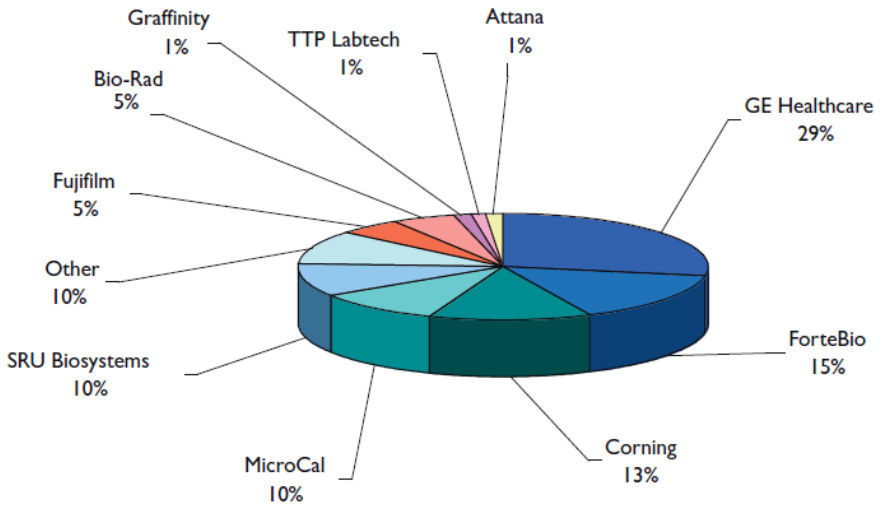

Figure 1.2. Estimated vendor market share for label-free binding analysis instruments (2008 to 2010) [23]

As shown in Figure 1.2 [23], current label-free biosensor market is dominated by surface plasmon resonance (SPR) based technology because of its high sensitivity [24], and also due to successful marketing by Biacore (GE Healthcare, UK [25]) [26], [27]. SPR detects the dip in the reflected light from the surface at a specific resonance angle as a function of refractive index change on the surface as shown in Figure 1.3. The resonance

angle shifts from I to II when molecular interaction is detected. However the relatively low quality factors (*Q*s) due to the large absorption by metal films and prism coupling method limits performance and instrument size.

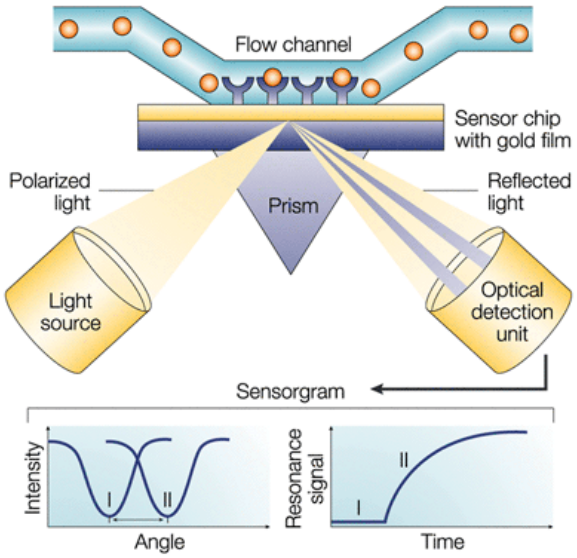

Figure 1.3. Conceptual setup diagram for an SPR biosensor [27]

Other silicon photonic biosensors have been demonstrated based on microspheres [28], [29], [30] microdisks [31], [32], microtoroids [12], [33], and photonic crystal cavities [34]. Microspheres, microdisks, and microtoroids exhibit extremely high *Q*s ($>10^6$) which would enhance the sensitivity, but these configurations also have many higher order whispering gallery modes (WGMs) which are not necessary for sensing [18]. Also it is hard selectively excite only the fundamental mode in these configurations, and it is also particularly difficult to couple light in and out of the microspheres in a practical and reproducible manner. Typically photonic crystals have relatively low *Q*s which limit the sensitivity compare to the other structures listed above. In this sense, ring resonators

provide promising solutions for biosensors due to their high *Q*s, single mode operation, simplicity of light coupling, and reproducible manufacture [18], and commercially available in the marketplace [35].

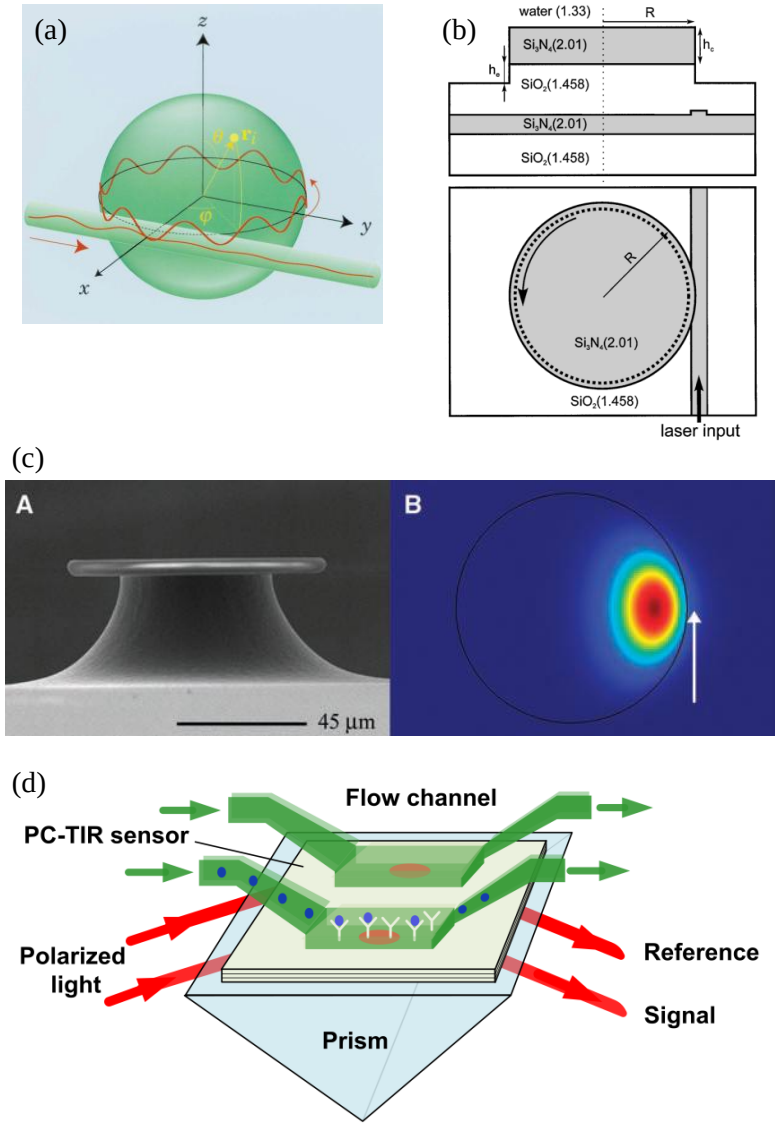

Figure 1.4. Basic biosensor configurations of (a) microsphere [28], (b) microdisk [32], (c) microtoroid [12], and (d) photonic crystal [34]

1.2 Detection Limit

Detection limit is an important parameter that captures the performance of a biosensor and represents the minimum resoluble signal [1], [4]. To determine the detection limit of a biosensor, the noise of the sensor must first be characterized which can be easily accomplished by measuring the time-resolved signal output to determine the standard deviation σ of the signal measurement. The smallest measurable signal S_{min} is usually defined as a signal S whose magnitude is the same as the noise σ, i.e., signal-to-noise ratio (SNR) of 1.

$$S_{min} = \sigma \tag{1.1}$$

The detection limit is then a measure of the index change, or concentration change, or mass deposition of detected species, that results in the signal S_{min}. The units of detection limit are refractive index unit (RIU) for bulk homogeneous index sensing, or either surface mass density in units of $\mathrm{fg/mm^2}$ or mass in units of ag (attogram) for surface sensing. The surface mass density or mass, however, are difficult to directly measure, so it is usually obtained by relating them to the effective refractive index or thickness change that could be determined experimentally. Another way to measure interaction is to use the concentration of analyte in units of ng/mL or molarity.

It is obvious from Eq. (1.1), that an improvement in the detection limit can be made by increasing the magnitude of signal of sensor for a given index change, and our use of the

thin, shallow-ridge SOI structure targets this approach. However, reducing noise is also critical, these noise sources are discussed next.

1.3 Diagnostics of Current Limitations for Optical Biosensors

A biosensor is the transducer that converts the complex biochemical parameters into quantitatively measurable signals [36]. In optical biosensors, biochemical parameters in the cladding cause a modal index perturbation within an evanescent field of the propagating optical mode in the waveguide, and the resulting phase change is typically interferometrically converted into an intensity change in some fashion, and the intensity change is detected and the resulting electrical signal is analyzed. Biosensors however pick up many unwanted signals, for example, thermal effects in waveguide, adding onto the output signal, thereby reducing the sensitivity [19], [37]. In addition to thermal-induced ambient noise, noises from the transmitter and receiver reduce the sensitivity. In the development of high-sensitive biosensors, noise is the fundamental factor that limits their performance. Three standard deviation (3σ) value is often used to describe overall system performance [18], [38], where σ represents the totality of temperature induced noise, optical intensity noise, and a variety of electronic noise sources, and we will demonstrate ways to minimize these contributions throughout this work.

Due to the large thermo-optic coefficient of silicon (~2×10^{-4} RIU/℃), these sensors typically exhibit a strong temperature dependence [19], [37]. This requires, for example, the use of reference rings [37] or additional temperature measurement [33], to allow for nullification of false reading or noise due to resonance shifts from unavoidable small

environmental temperature fluctuations. In an aqueous sensing environment, the negative thermo-optic coefficient of H_2O (~ -1×10^{-4} RIU/°C) can reduce the temperature dependence slightly, but standard wire waveguide designs are still dominated by the silicon index shift because of the strong confinement of optical power in silicon. In this work we illustrate that thin shallow-ridge waveguides provide sufficient confinement in an upper H_2O cladding to completely athermalize sensor operation, while still providing a near-ideal large field amplitude for homogenous and surface sensing.

Current method for signal readout in ring biosensors relies on scanning devices [18]-[20], [33], [37] such as high-precision tunable lasers, which are usually very expensive. Furthermore, this method is inherently prone to *1/f* noise in the amplification electronics, even when great care has been taken to match the electronic (and noise) bandwidth to the desired system response times. We demonstrate a feedback technique using a digital signal processing (DSP) lock-in amplifier without a scanning tunable laser that can provide narrow detection bandwidth at a high frequency, thereby reducing *1/f* noise in the biosensor system at a low cost.

1.4 Thesis Outline

Chapter 1 provides an introduction.

Chapter 2 starts with design and fabrication of low loss quasi planar ridge waveguide for TM mode operation which is important in achieving highly our sensitive biosensor. Our TM mode shallow-ridge waveguide technology is designed on a “Magic Width”

phenomenon that minimizes the severe lateral leakage losses into TE mode because of the mode conversion at the waveguide boundary. Also our novel waveguide fabrication techniques are discussed which enable smooth waveguide surfaces that noticeably reduce the scattering induced propagation losses in SOI high index contrast system. In our work 400 μm ring resonator with water absorption loss limited *Q*'s of 47,000 for the TM mode in H_2O were achieved as a result and integrated with the microfluidic channel.

In **Chapter 3**, we consider all noises in a system which degrade the performance of biosensors. Firstly, we study and measure intrinsic electronic and photonic noises in the system and discuss how to engineer low noise detection systems. Lastly, we discuss the ambient temperature induced noise because of thermo-optic coefficients in a waveguide and point out need for athermal waveguides.

In **Chapter 4** we theoretically and experimentally examine the athermal performance of novel TM mode SOI waveguide for aqueous biosensing application by taking advantage of opposite thermo-optic coefficients of water and silicon. Temperature independent operations of TM mode SOI waveguides that have slightly different thicknesses were measured and compared with TE mode.

Chapter 5 demonstrates the harmonic dithering technique which ensures low-noise, real-time, and low-cost biosensing using a single frequency distributed feedback (DFB) laser diode and a DSP lock-in amplifier. This is dithering technique similar to those developed for the laser frequency stabilization to an atomic resonance in a vapor cell, but we use the

Lorentzian lineshape drop port signal of ring resonator. We could successfully achieve reduced electronic *1/f* noise operation by harmonically dithering the laser frequency at high frequency, and complementing this with the standard low-pass filter of lock-in amplifier matched to the desired system response time to minimize broadband noise effectively. Also the performance of feedback loop is evaluated and compared with the more conventional DC detection method.

Finally in **Chapter 6,** both refractive index sensing and surface sensing are demonstrated to evaluate the biosensor performance using the introduced works in chapter 4 and 5, and we discuss the results of biosensing.

Chapter 7 draws the thesis conclusions and proposes future work.

Chapter 2

Low Loss Shallow-Ridge Waveguide on SOI Wafers

Sensitivity of ring resonator is proportional to $Q(=\nu/\Delta\nu)$ of resonator for intensity-noise limited operation [38]. To evaluate the relationship between sensitivity and *Q* following the formulation given in [39], assume resonant transmission of a ring resonator has full width at half maximum (FWHM) of $\Delta\nu_{FWHM} \approx \frac{1}{2\pi\tau_{ph}}$ where τ_{ph} is photon lifetime in a ring resonator. Frequency shift $\Delta\nu$ from center frequency *v* by small perturbation of modal effective index change Δn_{eff} is

$$-\frac{\Delta\nu}{\nu} \approx \frac{\Delta\lambda}{\lambda} \approx \frac{\Delta n_{eff}}{n_g} \tag{2.1}$$

where n_g is group index of waveguide. As a reference point, a full dynamic range signal would be obtained when the resonator shifts its peak location by $\Delta\nu_{FWHM}$, and corresponding index change is, from Eq. (2.1),

$$\Delta n_{eff} \approx \frac{n_g}{2\pi\nu\tau_{ph}} = \frac{n_g}{Q} \tag{2.2}$$

A resonator that has high *Q* clearly needs very small Δn to shift the peak by $\Delta\nu_{FWHM}$.

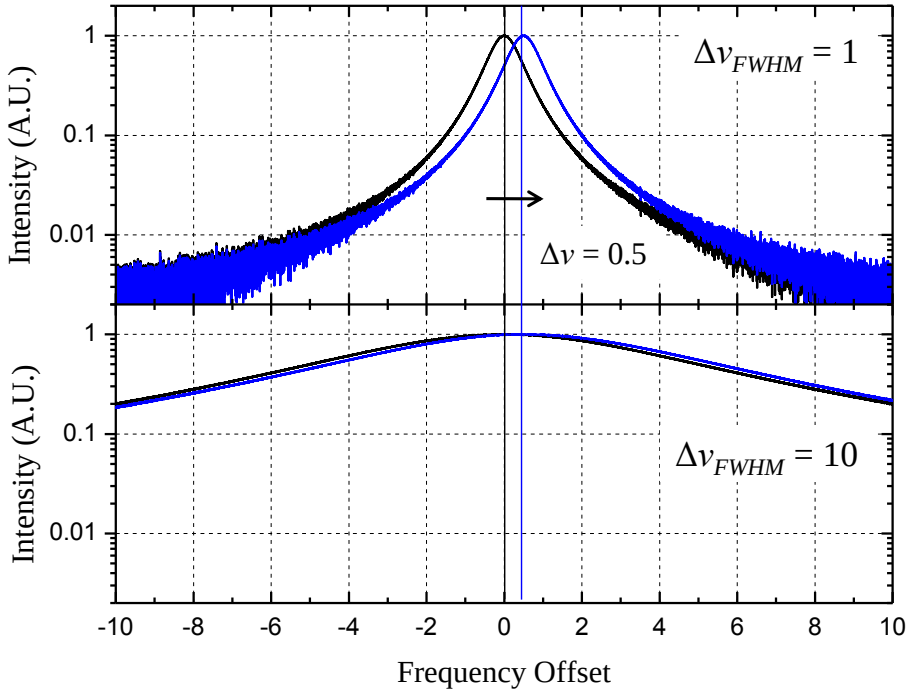

Figure 2.1. An example that shows why using a low loss device is beneficial for high-sensitivity biosensing.

Suppose that we have two drop port signals from two identical ring resonators with a signal-to-noise ratio of 60 dB, but the *Q*s are different by factor of 10 respectively, for example one has $\Delta\nu_{FWHM} = 1$ and the other one has $\Delta\nu_{FWHM} = 10$. For the reference if there is a frequency shift by $\Delta\nu = 0.5$ as illustrated in Figure 2.1, obviously it is easier to read the signal change from the higher *Q* ring resonator (upper plot in Figure 2.1). I. M. White *et al*. also theoretically estimated detection limits for different *Q* values in [38].

Sensitivity of Mach-Zehnder sensors can be enhanced by increasing the arm length as shown in Figure 2.2 [40], but in the aspect of device size, ring resonator provides better potential. The accompanying requirement of strongly frequency-dependent operation provides both constraints in the laser used for sensor readout, but also opportunities for simplification of detection techniques as shall be illustrated later.

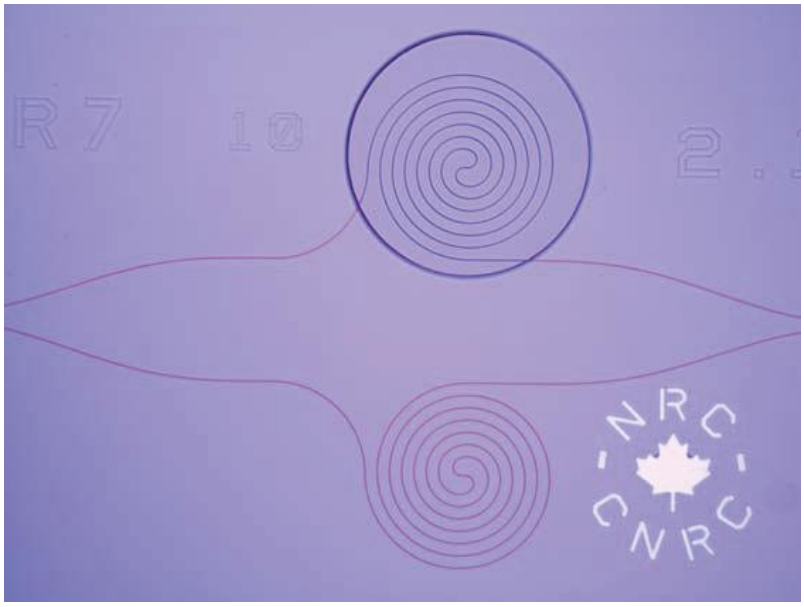

Figure 2.2. Image of spiral Mach-Zehnder biosensor to maintain a small footprint [40]. The arm length is 2 mm.

Our group has demonstrated high Q ring resonators of 1.6×10^6 for TE and 7.5×10^5 for TM which corresponds to waveguide propagation losses of 0.36 dB/cm and 0.94 dB/cm respectively [41], and when Q is larger than 10^6, the phase noise of laser starts play a bigger role in noise [38]. However there is a fundamental limitation of Q in TM mode aqueous biosensors. 1.55 μm is the very common wavelength in modern

telecommunications because of erbium-doped fiber amplifiers (EDFAs) and low-loss of single-mode optical fibers [42], but water has a large intensity absorption coefficient $\alpha_{1.55\mu m} = 11.67 cm^{-1}$ [43] which will cause the propagation loss of ~30 dB/cm for TM mode operation of silicon waveguide. The absorption is almost ten times smaller, $\alpha_{1.31\mu m} = 1.49 cm^{-1}$ [43], at 1.31 μm the original telecommunication wavelength which still limits the minimum propagation loss of ~ 3 dB/cm, $Q \approx 10^5$ for TM mode. This nevertheless represents a 10-fold improvement, and all measurement use 1.31 μm wavelength through this thesis. The absorption spectrum of water in near infrared range is plotted in Figure 2.3, and we can clearly see absorption coefficient decreases as wavelength approaches to visible range.

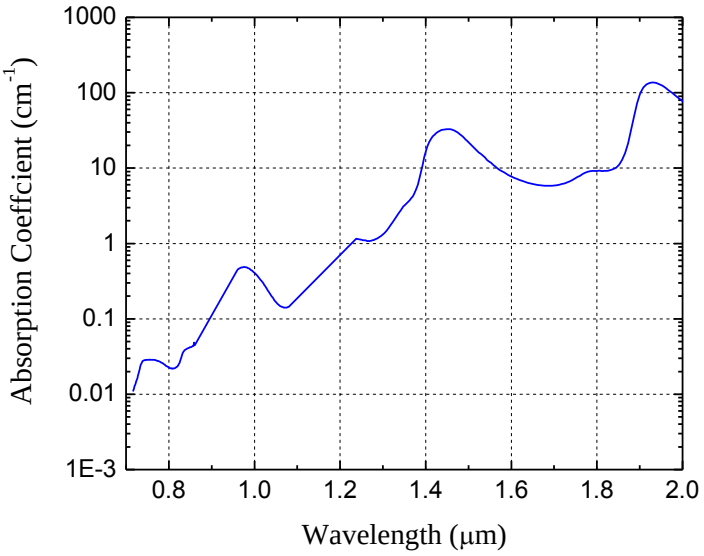

Figure 2.3. Absorption coefficient spectrum of water at 22 ℃ for near infrared wavelength

Conventional SOI wire waveguide, in Figure 2.4, typically uses reactive ion etching (RIE) to form the waveguide core. The high vertical and lateral confinements in silicon provide excellent bend radii down to the µm scale, but significant (multi-nanometer scale) sidewall roughness is commonly encountered from standard lithographic and etching processes. This suggests alternative fabrication techniques for highly smooth waveguides that minimize exposure of the mode to etched interfaces. Our goal of achieving high-sensitivity, low loss waveguides can be achieved by using the shallow ridge waveguide on the "magic width" technique [21]. It is known that shallow ridge waveguides do not support TM mode in general because of lateral leakage into cladding by TE mode. However there is "magic width" that eliminates the leakage loss of TM mode by using destructive interference of TE mode.

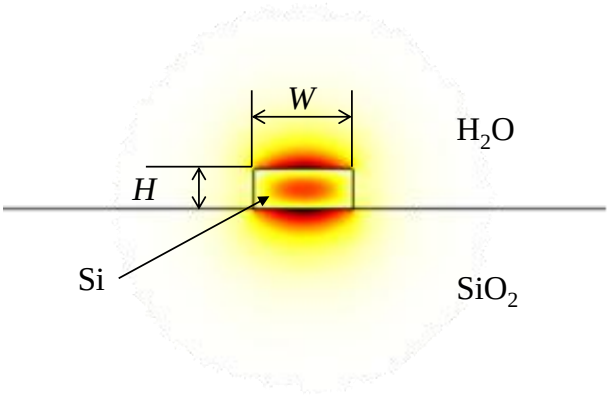

Figure 2.4 TM-mode electric field profile for conventional Si wire waveguide. Waveguide shown here has W = 500 nm and H = 200 nm.

In this chapter, we describe our strategies to minimize the propagation loss to achieve high *Q* devices suitable for high-sensitivity sensors, including physics, design, fabrication, and characterization of the SOI waveguide we elected to use.

2.1 Theory of Lateral Leakage Loss in Shallow Ridge Waveguides

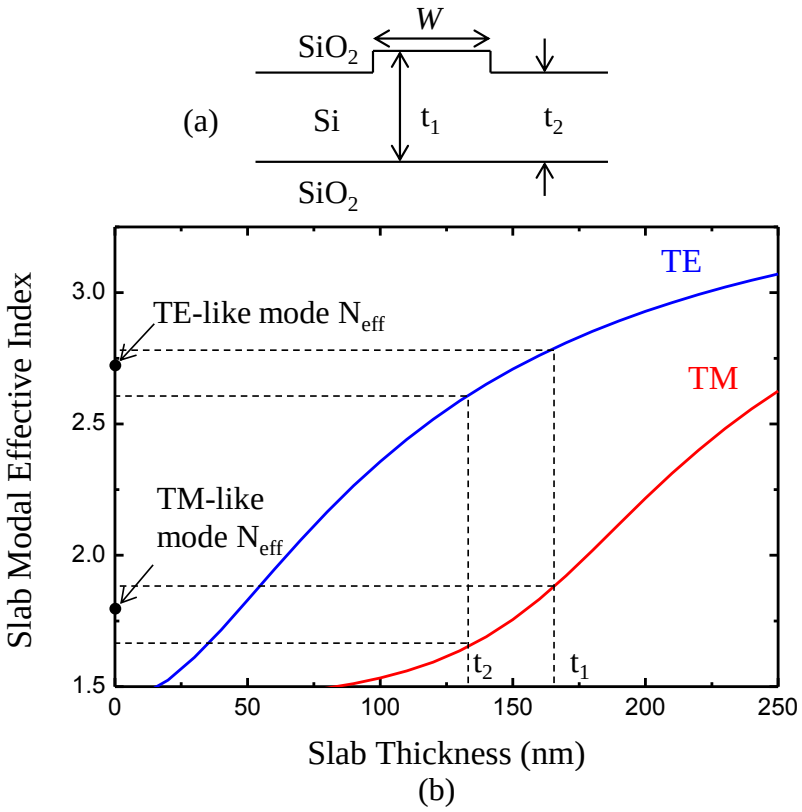

Figure 2.5. (a) Ridge waveguide geometry (b) Slab mode indexes used in effective index calculations. The modal indexes for the guided TE-like and TM-like modes, respectively, lie intermediate between their slab values for slab thicknesses t_1 and t_2. We use index values of $n_{Si}=3.50$ and $n_{SiO_2}=1.45$ at 1.31 μm wavelength.

Under an equivalent slab model for the ridge waveguide geometry (Figure 2.5 (a)), the lateral leakage loss for the TM-like mode is due to TM/TE mode conversion at the ridge boundary [21],[44]-[47]. It should be emphasized that this effect is not caused by any surface or side-wall roughness. With reference to slab waveguide dispersion curves in Figure 2.5 (b), for the case of TE-like modes, this mode conversion at the boundary cannot lead to any propagating field or leakage loss in the lateral cladding since longitudinal phase-matching requires that any fields generated at the ridge boundaries be laterally evanescent in the slab lateral cladding for both the TE and TM generated fields. However, in the case of the TM-like mode, while phase-matching requires that the lateral TM slab mode be evanescent in the lateral cladding, any TE slab field component generated at the boundary is phase-matched to a laterally propagating TE slab mode at some angle θ in the lateral slab cladding region.

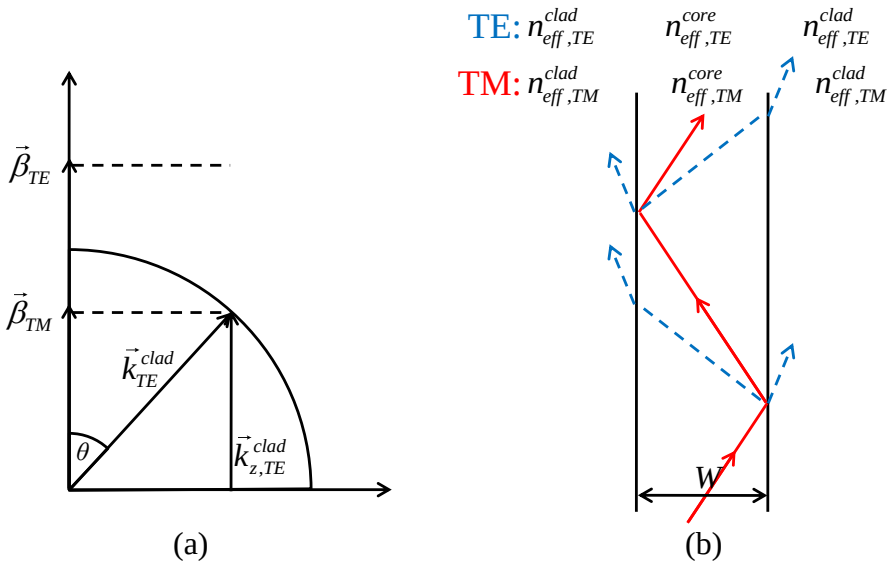

Figure 2.6. (a) Phase-matching diagram showing TM-like waveguide mode phase matched to a propagating TE slab mode in the lateral cladding (b) Ray picture of the TM mode lateral leakage

This phase-matching is illustrated in Figure 2.6 (a). Here β_{TE} and β_{TM} represent the propagation constants of the TE-like and TM-like modes of the ridge waveguide, respectively. This diagram illustrates that the propagation constant of the TM-like mode is much less than that of the TE-like mode, and for many practical rib guides may also lie below the propagation constant of the unguided TE slab mode k_{TE}^{clad}. Since this slab mode is unguided by the rib, it may propagate at any angle and if $\beta_{TM} < k_{TE}^{clad}$, it is possible to rotate k_{TE}^{clad} by an angle θ such that the TE-slab and TM-guided mode are phase-matched in the z direction. Since the guided mode is then phase-matched to a radiation mode, it is possible that leakage may occur if there is some means for mode conversion.

For a thin enough lateral slab thickness, and certainly in the case of a strip or wire waveguide where, the TE slab effective index can lie below the TM-like mode effective index, and hence, avoid this phase-matched leakage. However, for electrical access, these designs may not be practical, and thus, this leakage loss must be well understood.

The leakage process is illustrated in Figure 2.6 (b). Since the *z* components of all propagation constants are conserved, all waves develop the same relative phase along the length of guide and we can discuss phase in the lateral direction only.

Starting at the bottom, a TM mode is guided by the rib and is represented as the solid ray incident on the right wall, where the angle of incidence is such that TM total internal reflection occurs. However, due to the step discontinuity at the rib wall, mode conversion from TM to TE can occur, and it can be shown from mode-matching calculations [47] that TE transmitted and reflected propagating waves are produced that are approximately equal in magnitude, but are ~π radians out of phase. The reflected TE radiation mode traverses across the core as shown by a dashed line. Upon total internal reflection, the TM mode experiences a negative phase shift ϕ_{TIR} and the combination of ϕ_{TIR} with the phase from a single traverse of the guide to the left is zero for the fundamental mode.

At the left rib wall, the TM mode generates additional small reflected and transmitted TE propagating waves. The new transmitted TE wave, with a relative phase of π radians as noted above, combines with the previous reflected TE wave that has traversed the guide

with a phase shift of $k_{x,TE}^{clad} \cdot W$. Thus, if this phase shift across a single traverse for the TE in the core is a multiple of *2π*, the TE waves will interfere destructively. This leads to a width dependence for the leakage minima that satisfies a resonance-like condition [46] of $k_{x,TE}^{clad} \cdot W = m \cdot 2\pi$, or alternatively stated [21], [44],

$$W = \frac{m \cdot \lambda}{\sqrt{(n_{eff,TE}^{core})^2 - N_{eff,TM}^2}}, \qquad m = 1, 2, 3... \tag{2.3}$$

where $n_{eff,TE}^{core}$, is the two-dimensional slab effective index of the TE mode in the core while $N_{eff,TM}$ is the full three-dimensional effective index of the TM-like mode for the structure. $N_{eff,TM}$ has a weak *W* dependence, so some care must be used if precision is required. From this argument, we would expect to see significant leakage loss for TM propagation, except at precise, specific waveguide widths – "magic widths" satisfying the resonance condition in Eq. (2.3), where the leakage loss would be greatly reduced due to destructive interference of radiating TE waves. It is also interesting to note that the next higher order mode will be lossy at these widths, since the radiated fields add in phase for this mode. This may allow relatively wider guides with effectively single-mode behavior.

2.2 Experimental Demonstration of Magic Widths

A series of ridge waveguides with widths varying from 0.8 to 2.4 μm in 25 nm increments with slab thickness t_1=144 nm and t_2 =131 nm (i.e. a 13 nm ridge height) were fabricated on an SOI wafer with a 3 μm BOX layer thickness. These waveguides

were formed by wet etching, followed by oxidation to thin the device and passivated by 1.5 μm thick oxide using the plasma-enhanced chemical vapor deposition (PECVD).

The upper plot in Figure 2.7 shows calculated waveguide loss for TM mode waveguide using COMSOL [48] with a finite element model (FEM) with perfectly matched layer (PML) boundary conditions when the waveguide width varies from 0.8 to 2.4 μm. The calculated magic widths are both 1.27 and 1.91 μm for the structure shown in Figure 2.7.

Measured waveguide transmissions using the tapered fiber coupling method is shown in lower plot of Figure 2.7 for both TE (black closed square) and TM (red opened circle) mode as a function of waveguide width on the mask file. There is about 50 nm difference in width between two plots due to combination of shrinking in waveguide width because of oxidation and underexposure in lithography. For single mode operation, using narrower waveguide width is preferred. Waveguide widths for biosensor were designed to be 1.23 and 1.27 μm for SiO_2 and H_2O cladding respectively.

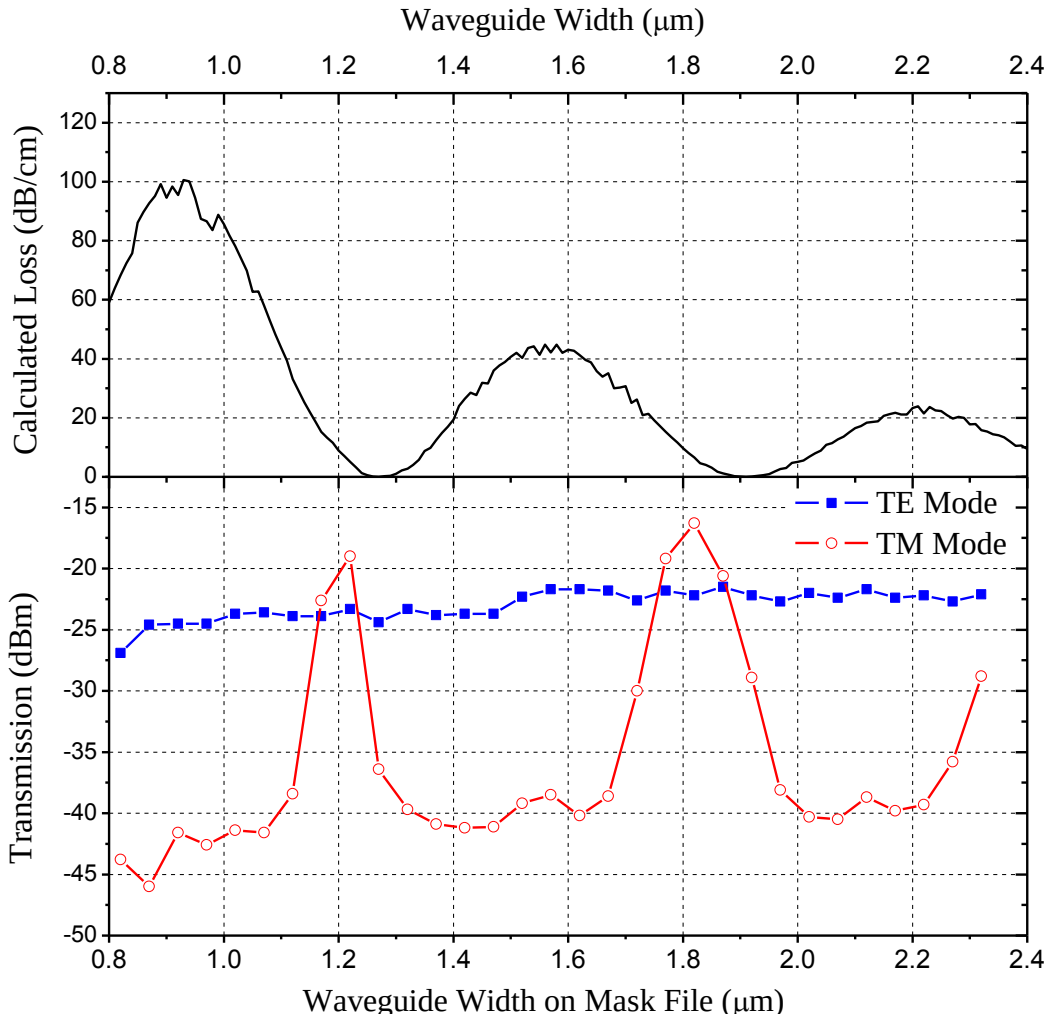

Figure 2.7. TM-mode waveguide width dependent loss from simulation using COMSOL in upper plot and measured waveguide transmission for both polarizations in lower plot.

2.3 Fabrication of Shallow-Ridge Waveguides Using a CMOS Process

The waveguides are patterned on 6" Soitec [49] SOI wafer via lithography which provides uniform linewidth control. Two different masks were used to form waveguides

and to open circular windows around rings for sensing. The fabrication process flow is illustrated in Figure 2.8.

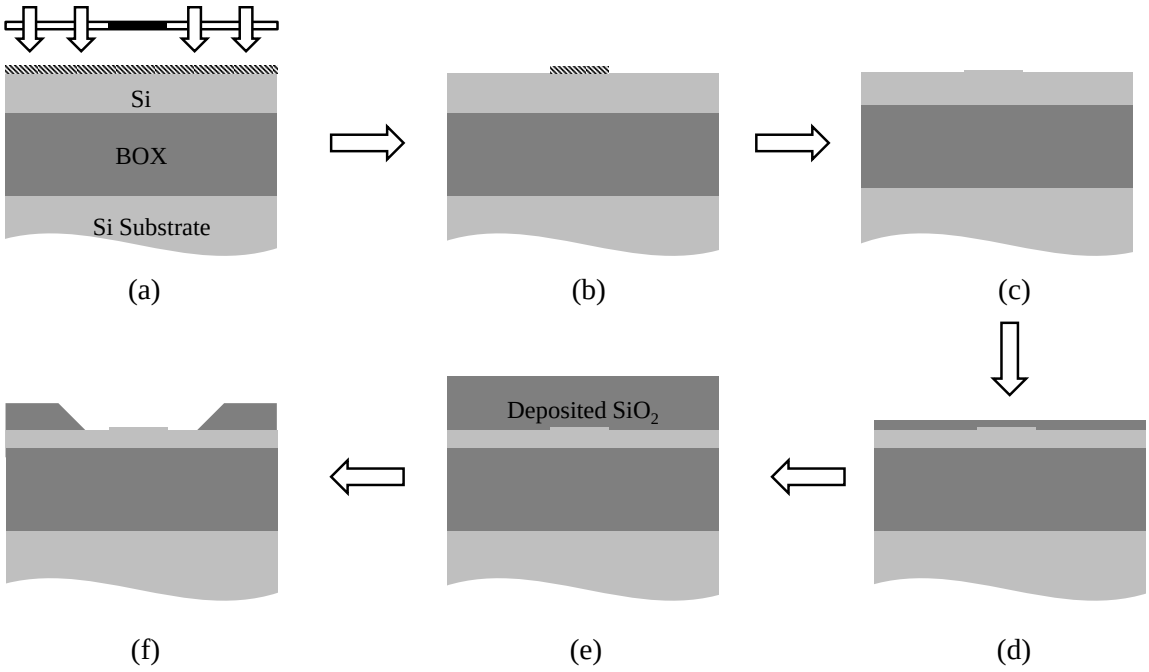

Figure 2.8. Fabrication flow of the Si waveguide on SOI wafer

The SOI wafers used have 3 μm BOX and 220 nm silicon on it, and a 1 μm thick AZ703 photoresist coated SOI wafer was exposed by ultraviolet light through the Cr mask (Figure 2.8 (a)) and developed (Figure 2.8 (b)). The BOX is thick enough to prevent the field associated with the optical modes from penetrating the silicon substrate below. Waveguide widths were defined by using an isotropic wet etchant of silicon consisting of nitric acid, ammonium fluoride, and de-ionized water in the ratio of $HNO_3 : H_2O : NH_4F$ of 1000:800:20 to etch the field as illustrated in Figure 2.8 (c), using "magic width" designs. We thinned the silicon via thermal oxidation as show in Figure 2.8 (d) to have

cancellation of the thermo-optic effect which will be discussed in Chapter 4. This process not only guarantees a high-quality oxide suitable for integration with electrical components on the same chip, but has the benefit of smoothing silicon surface roughness [50].

We deposited additional 1.5 μm thick SiO_2 , in Figure 2.8 (e), using the PECVD to protect the bus waveguides from the absorption of water, and the oxide layer was removed locally in a circular region around the ring resonator to expose the sample to a flowing aqueous solution within microfluidic chamber as illustrated in Figure 2.8 (f). Figure 2.9 (a) illustrates the electric field profile in shallow-ridge silicon waveguide for TM mode obtained from COMSOL with PML. The geometry of waveguide is the one used for this thesis, and we can see strong confinement of electric field in cladding that increases the sensitivity of sensors. Figure 2.9 (b) is schematic view of 400 μm radius ring resonator sensor.

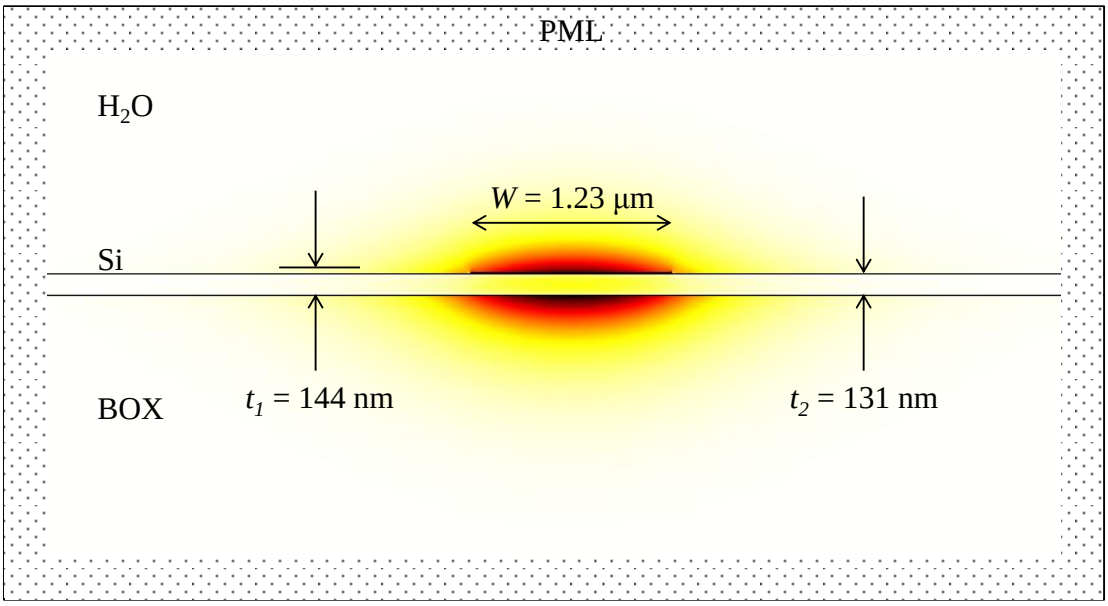

(a)

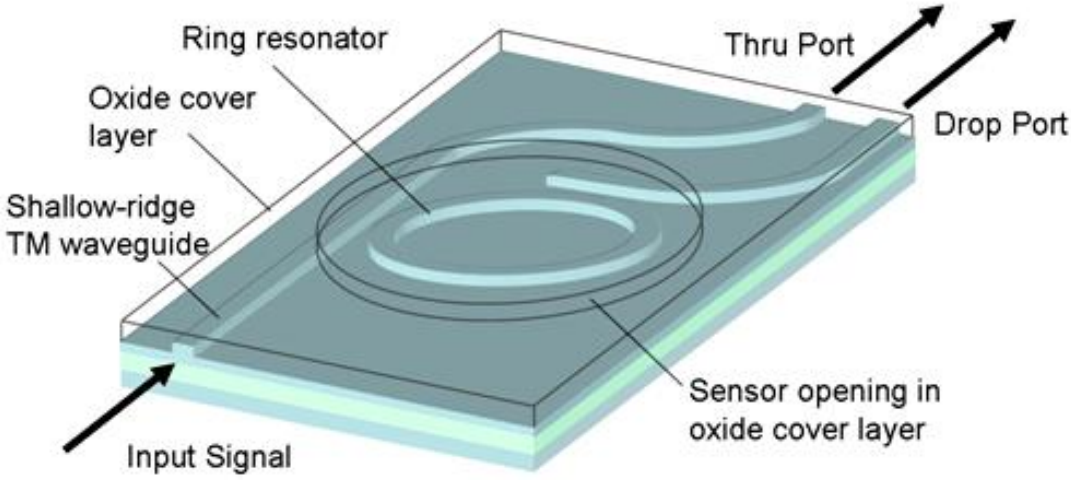

(b)

Figure 2.9. (a) Simulated 3D electric field profile for a fundamental TM mode in the Si waveguide and (b) schematic of fabricated ring resonator silicon chip

Fabricated 6" SOI wafer was diced into 54 pieces of 16×9 mm silicon chip (American Dicing, NY [51]), and the end-facet of each chip was mechanically polished to 0.1 μm for good light coupling between tapered fibers and waveguides. All chips were washed in piranha solution (1:3 mixture of H_2O_2 and H_2SO_4) for ten minutes to clean any residual photoresist and to render the hydrophobic silicon surface into hydrophilic by forming a monolayer of oxide on surface, resulting better wetting of sensor surface to aqueous medium. The micro fluidic cell was made of Polydimethylsiloxane (PDMS) on the silicon wafer mold and integrated with silicon ring biosensors as can be seen in Figure 2.10 (a). The PDMS microfluidic channel was designed to be 0.05 mm in height × 1 mm in width. And then we annealed PDMS cells in the convection oven for three days at 120 ℃ to decrease the hydrophobic recovery time [52]. The bottom side of PDMS was then treated in piranha solution to make its inherent hydrophobic surface into hydrophilic. Figure 2.10 (b) shows the ring resonators in the PDMS microfluidic channel. A spring-loaded plastic fixture was developed to provide a gentle pressure onto PDMS cell to prevent possible fall-off of chip during the measurement. After the measurement, both chip and PDMS were washed by piranha solution to be reused again.

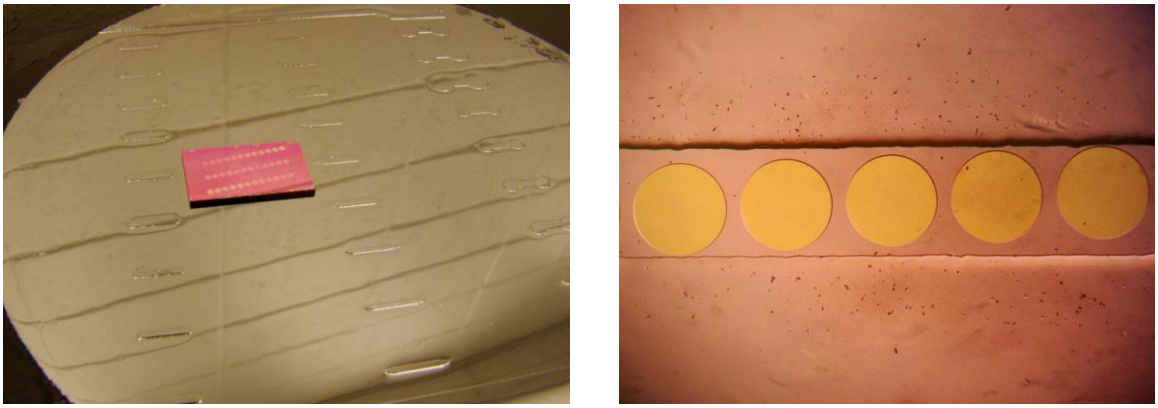

(a) (b)

Figure 2.10. (a) Silicon mold for PDMS microfluidic channel and fabricated silicon photonic biosensor chip. Each circular pattern on the chip is the ring biosensor after the oxide etching. (b) Array of ring biosensors in the microfluidic channel.

2.4 Waveguide Loss Measurement Technique

Considering the contributions due to both loss and coupling efficiency, it is not easy to accurately measure the propagation loss using the straight waveguide. Several techniques are available for waveguide loss measurement such as cut-back or Fabry-Perot resonance methods, but these methods do not provide accurate results because of variation in fiber coupling loss and end-facet reflectivity [50]. For accurate and reliable quantization of propagation losses, we use the resonance characteristics of under-coupled ring resonators.

To characterize ring resonators, we used the resonance condition of resonator by measuring $\Delta\nu_{FWHM}$ of drop port transmission and free-spectral range. The normalized Lorentzian lineshape for $\Delta\nu_{FWHM}$, when transmission peak is centered at ν_0, is

$$f(\nu) = \frac{(\Delta\nu_{FWHM}/2)^2}{(\nu-\nu_0)^2 + (\Delta\nu_{FWHM}/2)^2} \tag{2.4}$$

Ideal lossless resonator has transmission peak of delta function lineshape ($\Delta\nu_{FWHM}$ = 0), but due to material absorption, imperfection of fabrication, bending loss, radiation, and finite waveguide input-output coupling loss, we have finite value of $\Delta\nu_{FWHM}$.

The ring configuration in Figure 2.9 (b) has separate through and drop ports and consists of two directional couplers that are designed to be under-coupled so that the ring losses are dominated by the waveguide losses rather than the input/output coupling of the ring to the thru-port and drop-port waveguides. Using the nomenclature of Yariv [53], the expression for line width for our structure is

$$\Delta\nu_{FWHM} = \frac{v_g}{\pi L_{rt}}\left(\frac{1-|\tau t_1 t_2|}{\sqrt{|\tau t_1 t_2|}}\right) \tag{2.5}$$

where v_g is the group velocity, L_{rt} is the round-trip length, τ is the field transmission of the waveguide for one round trip of the ring, and t_1, t_2 are the field transmission coefficients of the directional couplers. The couplers are assumed to be lossless, giving $|t|^2 + |\kappa|^2 = 1$ where κ is the field coupling coefficient. To simplify the expression in Eq. (2.5), we can write $|\tau| = \exp(-\alpha L_{rt}/2)$ with α being the waveguide intensity attenuation coefficient and if we let $|t_1| = \exp(-\alpha_1 L_{rt}/2)$ and $|t_2| = \exp(-\alpha_2 L_{rt}/2)$, then for the case of low loss ($|\tau| \approx 1$) and weak coupling ($|t_1| \approx |t_2| \approx 1$), we obtain the simple expression

$$\Delta\nu_{FWHM} = \frac{\alpha_{rt} v_g}{2\pi} \tag{2.6}$$

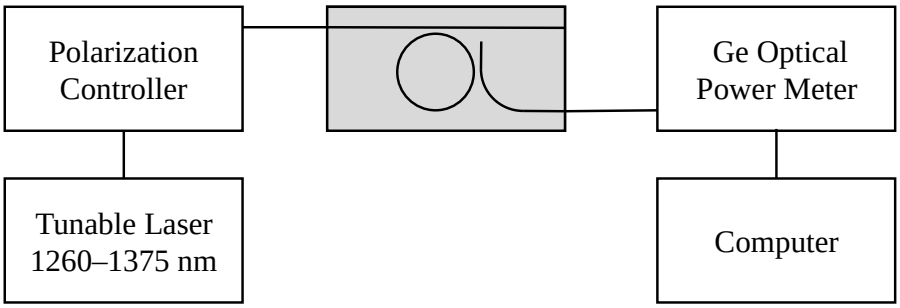

Figure 2.11 Experimental setup for the ring resonator (gray colored) measurement using the tunable laser instrumentation. 125 μm tapered fibers are used to couple the light in and out.

The round-trip loss α_{rt} is the sum of the waveguide propagation losses α and the coupling losses from the two directional couplers (α_1 and α_2), but, if the ring is designed to be weakly coupled, then $\Delta\nu_{FWHM} = \alpha v_g / 2\pi$. Since precision frequency scans allow for an accurate determination of resonance width, this provides an unambiguous and conservative figure for waveguide transmission losses.

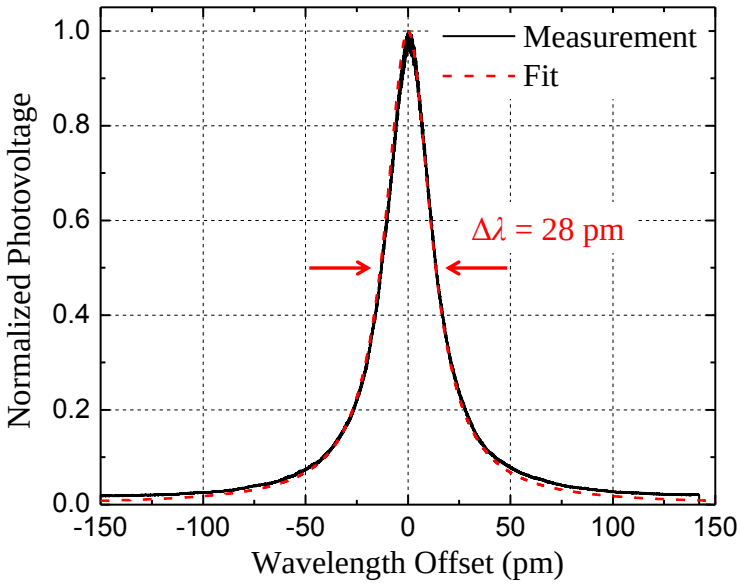

Figure 2.12. Measured black line and Lorentzian fitted red dashed line from the 400 μm ring resonator at 1310 nm using the tunable laser

For the loss measurement with the setup shown in Figure 2.11, the external cavity tunable laser scanned wavelength λ from 1310 to 1312 nm, and we fitted the photovoltage response using a Lorentzian fitting method. We employed a InGaAsP Fabry-Perot external cavity tunable laser (Agilent, CA) with a narrow linewidth of < 10 MHz and slow λ tuning speed of 0.5 nm/s, and the 1 kHz bandwidth of power meter was large enough not to distort drop port signals in our measurement. A polarization controller is implemented between single mode and polarization maintaining fibers to avoid launching the TE mode. The extinction ratio between TE and TM mode was ~ 23 dB.

Figure 2.12 shows measured (black sold line) and fitted (red dashed line) drop port spectrum of 400 μm ring resonator with magic width of 1.23 μm for TM mode. From

fitted curves, we obtained free spectral range of 0.3 nm, total loss of 9.5 dB/cm, and $Q = 4.7 \times 10^4$.

Each diced silicon chip had dimension of 16×9 mm and 36 different unique 400 μm ring biosensors. Two different masks for the lithography of waveguides and sensing windows are shown in Figure 2.13 (a) with blue and purple colors respectively. The ring resonator used for the biosensing is highlighted with black circle among 36 ring biosensors. The coupling gap *G* between ring and bus waveguides was 1.85 μm as shown in Figure 2.13 (b), and two dimensional simulations using RSOFT [54] result in a predicted coupling power of 1.3 % for each coupler. Since there are two couplers for the ring resonator, the overall contribution of coupling loss is 0.45 dB/cm, and thereby the propagation loss is estimated to be 9 dB/cm after the coupling correction. We observed 5.5 dB excess loss in addition to the estimated loss of 3.5 dB/cm (absorption of water and fabrication loss), and we suspect that it is caused by HF defects while opening sensing windows.

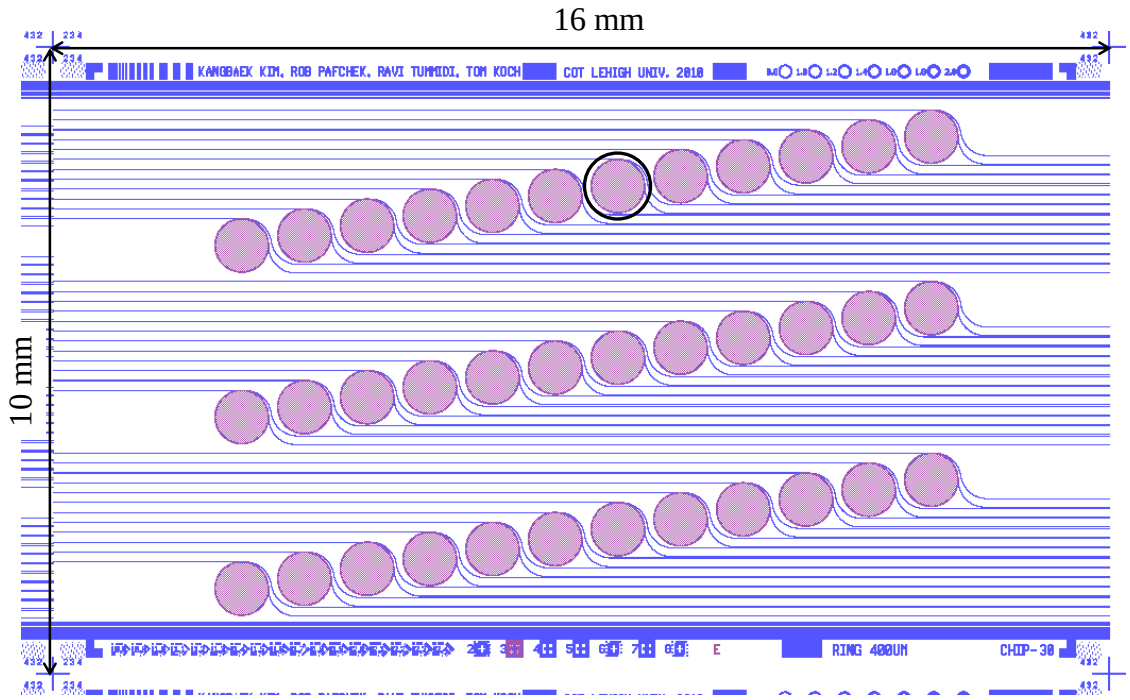

(a)

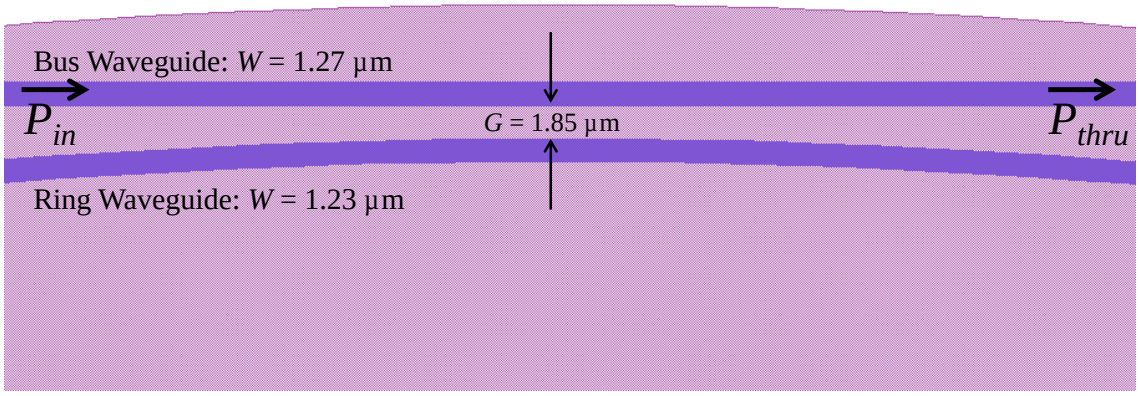

(b)

Figure 2.13 (a) Overlapped two mask images of the silicon biosensor chip. The blue layer is the waveguide level, and the purple is for oxide etching. The actual ring

resonator used for the measurement is highlighted with the black circle. (b) Coupler between bus and ring waveguides.

2.5 Principles of a Silicon Photonic Biosensor

While an electromagnetic field propagates along a waveguide, its evanescent wave interacts with biomolecules adsorbed on the sensor surface or homogeneous index change in cladding, thereby causing change in the modal effective index. To increase the surface sensitivity, maximizing the filed overlap with thin adsorbed layer is required.

This surface sensitivity was calculated for a thin biological layer (n=1.5) on the silicon surface using the weighting function [55]. The modal index change in a slab waveguide due to the adsorbed biolayer can be expressed

$$\Delta n_{eff} = \int_{biolayer} \Delta n(y) f(y) dy \tag{2.7}$$

$f(y)$ is the weighting function that implies structural sensitivity of waveguide to refractive index perturbation $\Delta n(y)$ and defined by

$$f(y) = \frac{2c\varepsilon_0 n(y)\vec{E}\cdot\vec{E}^*}{\int_{-\infty}^{\infty}(\vec{E}\times\vec{H}^* + \vec{E}^*\times\vec{H})\cdot\hat{z}dy} \tag{2.8}$$

where c is the speed of light, ε_0 is permittivity in vacuum, $n(y)$ is the distribution of refractive index in y axis, $\vec{E}$ and $\vec{H}$ denotes electric and magnetic fields respectively, and $\hat{z}$ is the normalized vector of propagation axis of light. The calculation of electric field is detailed in Chapter 3.

Use of a high *Q* ring resonator for biosensors is advantageous over a Mach-Zehnder configuration. A Mach-Zehnder interferometer that has *L* arm length requires an index shift of [39]

$$\Delta n = \frac{\lambda}{2L} \tag{2.9}$$

for V_π, and to have the same sensitivity to a ring resonator

$$L = Q\frac{\lambda}{2n_g} \tag{2.10}$$

The *Q* we can achieve for 1.31 μm operation is $\sim 10^5$ in an aqueous environment, and this leads to a 22 mm long arm for a Mach-Zehnder interferometer of comparable sensitivity. In this sense, a ring resonator configuration provides benefits because of small size and simplicity.

When a ring resonator experiences index change, the wavelength of resonantly coupled drop port signal shifts according to Eq. (2.1)

$$\Delta\lambda = \lambda\frac{\Delta n_{eff}}{n_g} \tag{2.11}$$

To convert adsorption of molecules on a sensor surface, we can effectively think that the thickness is uniformly increasing over the 2μm lateral optical field. And Δn_{eff} due to the thickness change can be easily obtained by separate calculations.

The area of 400 µm ring biosensor surface is 5026.6 μm^2, and in contrast 251.3 μm^2 for 20 µm ring resonator. This indicates, for the same absolute number of adsorbed molecules, that the smaller ring biosensor would provide fundamentally higher sensitivity if the molecules could be directed specifically to the smaller ring structure

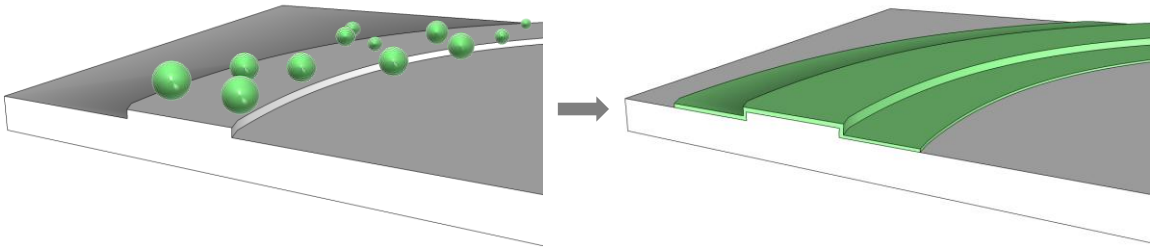

Figure 2.14. Adsorbed molecules near the ring waveguide can be regarded as a thickness increase of thin film on the waveguide across the lateral optical field.

Chapter 3

Athermal Silicon Waveguides for Aqueous Evanescent Biosensor

High-sensitivity optical biosensor can accurately measure any index changes within its evanescent field, but they also sensitively interact with any environmental noises such as microfluidic turbulence, ambient temperature fluctuation, electronic noises, and mechanical noises which are not desirable.

However there are always unavoidable fluctuations in the environmental temperature induced by equipment, air circulation, or body heat of users. Even at a thermal equilibrium, introducing another aqueous solution during the measurement can break the steady state, thereby leading a false reading of signal. Not only the instruments, but also silicon based optical sensors themselves exhibit strong temperature dependence because of index shift with temperature. For example, the thermo-optic coefficient of silicon at 1.31 μm is 2×10^{-4} RIU/℃ near room temperature [56]. This is also a challenging part in development of silicon photonic components for wavelength division multiplexing (WDM) applications. Room temperature was continually monitored over four hours and

plotted in Figure 3.1, and it has ~ 0.1℃ root mean square (rms) fluctuations in temperature.

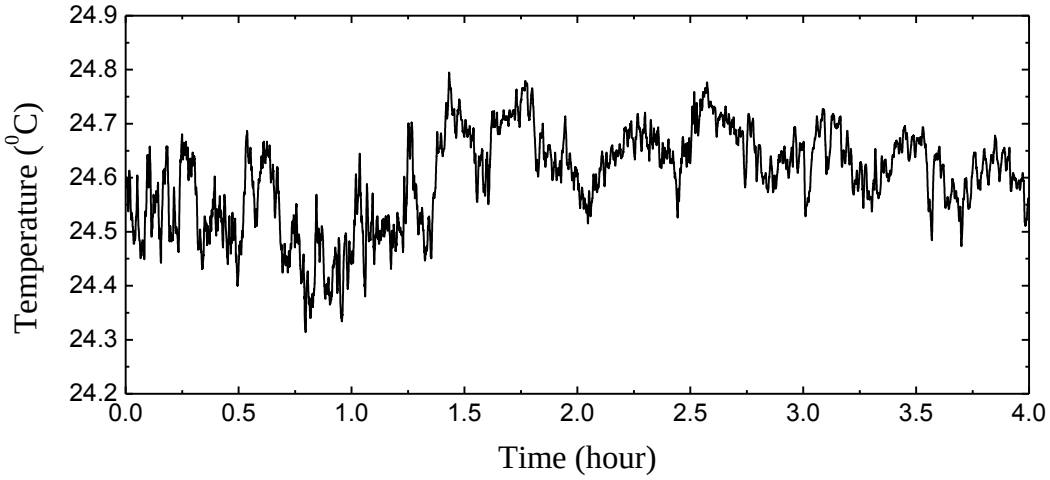

Figure 3.1. Fluctuation of room temperature over 4 hours

An optical biosensor that uses an aqueous medium as a cladding experiences the index change of H_2O with temperature according to the thermo-optic coefficient of -1×10^{-4} RIU/℃ [57] in both visible and near-infrared ranges at a room temperature. For silicon wire waveguide based biosensors in aqueous medium that have typical geometries of 500 nm width and 200 nm height, the fluctuation shown in Figure 3.1 causes the refractive index noise of 1.3×10^{-5} RIU which is orders of magnitude larger than detection limit typically in the range of 10^{-7} RIU for bulk refractive index sensing [18], [29], [58]-[62]. Therefore the temperature effects must be avoided. TM mode silicon microring resonators on wire waveguide geometry have slightly mitigated temperature effects because silicon and water have opposite thermal effects each other, but still large optical

confinement in silicon requires precisely temperature controls. This is a less desirable solution because it takes additional space and power consumption.

There have been several demonstrations of reference techniques to compensate the temperature induced signal change by using a reference ring [40] or ice water [33] as shown in Figure 3.2. These two techniques require additional calculation steps to compensate the relative wavelength shift using obtained data, and thereby hinder the efficacy of real-time measurements. Particularly the use of an ice water, in Figure 3.2 (b), adds major complexity in the experimental setup and does not provide a practical engineering solution.

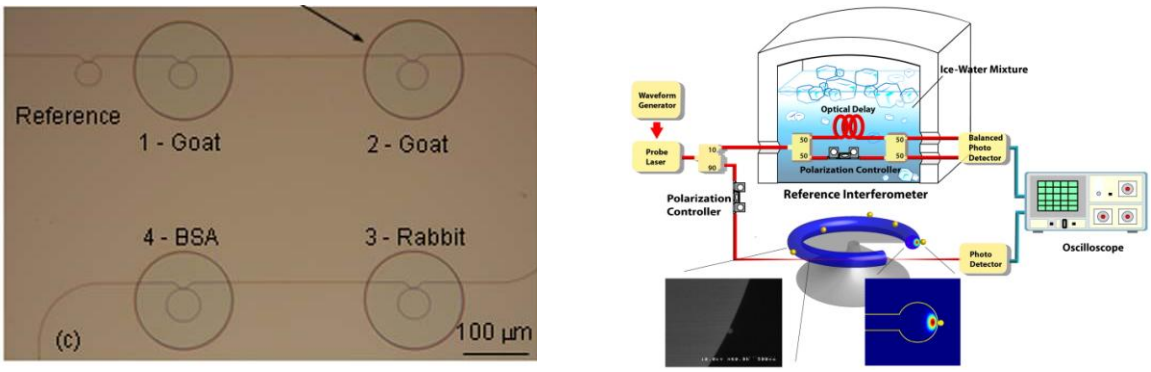

(a) (b)

Figure 3.2 (a) On-chip temperature cancellation using a reference ring [40] and (b) schematic experimental setup using an ice-water bath as a reference [33]

In this chapter, we focus on the large optical confinement of shallow-ridge waveguide geometries which can provide an embedded solution for athermal waveguide biosensors without requiring any reference techniques.

3.1 Calculation for Athermal Silicon Waveguides

The performance of the biosensor is numerically modeled using exact slab values combined with lateral effective index methods [56] suitable for the shallow ridge waveguide, with published index of refraction values for Si [56], H_2O [57], and SiO_2 [63] for 1.31 μm wavelength. Refractive indices used for calculations are detailed in Appendix A.

3.1.1 Effective Index Methods via a Transfer Matrix Method

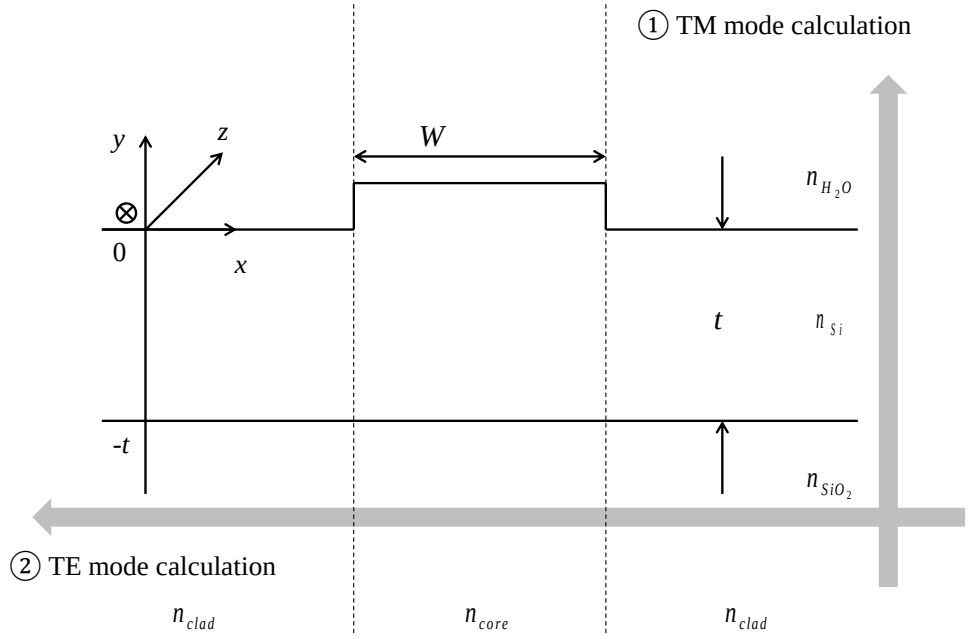

Figure 3.3. Decomposition of ridge waveguide into two imaginary slab waveguides for the effective index calculation.

For the calculation of effective index of ridge waveguide shown in Figure 3.3, we first consider the propagation of TM mode in a multilayer slab waveguide along the vertical

direction using a transfer matrix method [64]. And then repeat the lateral slab mode calculation for TE mode using the obtained TM-mode slab values from the previous step to find the root. The effective index method provides a very accurate solution for the shallow-ridge waveguide model because of small index contrast between n_{core} and n_{clad}.

This sub-section closely follows the formulation given in [64].

The interface matrix for TE polarization

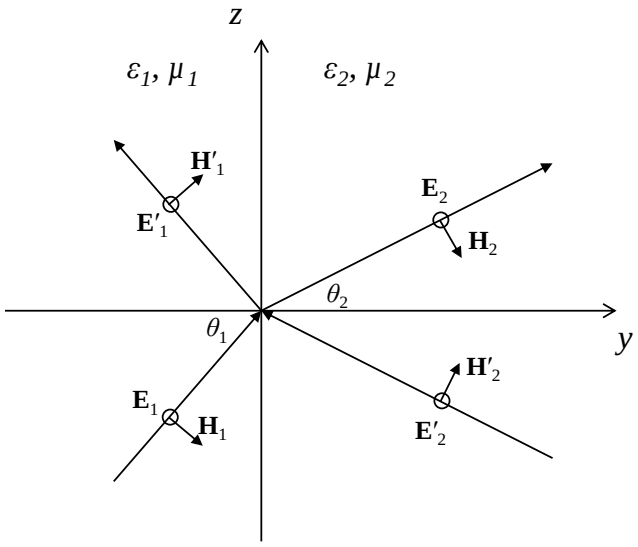

Figure 3.4 Reflection and refraction at the interface for TE polarization

Figure 3.4 illustrates the interface between two media for TE polarization. All electric field vectors are perpendicular to the plane of incidence, and magnetic field vectors are determined to have a positive energy flow along the direction of wave vectors. Due to the continuity of E_x and H_z fields at *y=0*

$$\begin{aligned} E_{1s} + E_{1s}^{'} &= E_{2s} + E_{2s}^{'} \\ \sqrt{\frac{\varepsilon_1}{\mu_1}}(E_{1s} - E_{1s}^{'})\cos\theta_1 &= \sqrt{\frac{\varepsilon_2}{\mu_2}}(E_{2s} - E_{2s}^{'})\cos\theta_2 \end{aligned} \tag{3.1}$$

where $H = \sqrt{\frac{\varepsilon_i}{\mu_i}}E$ and *i* denotes medium 1 or 2.

We can rewrite the Eq. (3.1) using a matrix equation

$$D_{TE}(1)\begin{pmatrix} E_{1s} \\ E_{1s}^{'} \end{pmatrix} = D_{TE}(2)\begin{pmatrix} E_{2s} \\ E_{2s}^{'} \end{pmatrix} \tag{3.2}$$

where

$$D_{TE}(i) = \begin{pmatrix} 1 & 1 \\ \sqrt{\frac{\varepsilon_i}{\mu_i}}\cos\theta_i & -\sqrt{\frac{\varepsilon_i}{\mu_i}}\cos\theta_i \end{pmatrix} \tag{3.3}$$

We define the matrix $D_{TE}(i)$ the interface matrix for TE polarization. When a light comes from medium 1, reflection and transmission coefficients are at the interface

$$\begin{aligned} r_{TE} &= \left(\frac{E_{1s}^{'}}{E_{1s}}\right) = \frac{n_1\cos\theta_1 - n_2\cos\theta_2}{n_1\cos\theta_1 + n_2\cos\theta_2} \\ t_{TE} &= \left(\frac{E_{2s}}{E_{1s}}\right) = \frac{2n_1\cos\theta_1}{n_1\cos\theta_1 + n_2\cos\theta_2} \end{aligned} \tag{3.4}$$

under the assumption of $\mu_1 = \mu_2$, which is acceptable for most of optical material. The refractive index of media 1 and 2 are n_1 and n_2 respectively.

The interface matrix for TM polarization

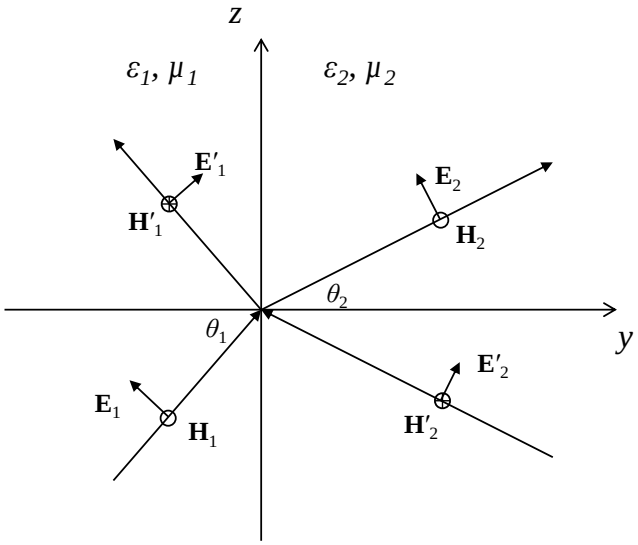

Figure 3.5 Reflection and refraction at the interface for TE polarization

TM mode has perpendicular magnetic field vectors to the plane of incidence as shown in Figure 3.5. Imposing the continuity of E_z and H_x leads to

$$\begin{aligned}(E_{1p} + E_{1p}^{'})\cos\theta_1 &= (E_{2p} + E_{2p}^{'})\cos\theta_2 \\ \sqrt{\frac{\varepsilon_1}{\mu_1}}(E_{1p} - E_{1p}^{'}) &= \sqrt{\frac{\varepsilon_2}{\mu_2}}(E_{2p} - E_{2p}^{'})\end{aligned} \tag{3.5}$$

We can rewrite the Eq. (3.5) using a matrix equation

$$D_{TM}(1)\begin{pmatrix} E_{1p} \\ E_{1p}^{'} \end{pmatrix} = D_{TM}(2)\begin{pmatrix} E_{2p} \\ E_{2p}^{'} \end{pmatrix} \tag{3.6}$$

and the interface matrix for TM polarization is

$$D_{TM}(i) = \begin{pmatrix} \cos\theta_i & \cos\theta_i \\ \sqrt{\frac{\varepsilon_i}{\mu_i}} & -\sqrt{\frac{\varepsilon_i}{\mu_i}} \end{pmatrix} \tag{3.7}$$

If a light is incident from medium 1, reflection and transmission coefficients are

$$\begin{aligned} r_{TM} &= \begin{pmatrix} E'_{1p} \\ E_{1p} \end{pmatrix} = \frac{n_1\cos\theta_2 - n_2\cos\theta_1}{n_1\cos\theta_2 + n_2\cos\theta_1} \\ t_{TM} &= \begin{pmatrix} E_{2p} \\ E_{1p} \end{pmatrix} = \frac{2n_1\cos\theta_1}{n_1\cos\theta_2 + n_2\cos\theta_1} \end{aligned} \tag{3.8}$$

and again assuming $\mu_1 = \mu_2$.

Transfer Matrix Method for Multilayer Structure

For the calculation of effective index of ridge waveguide shown in Figure 3.3, we first consider the propagation of TM mode in a multilayer slab waveguide, for more practical approach, with index profiles given by

$$n(y) = \begin{cases} n_0, & y < y_0 \\ n_1, & y_0 < y < y_1 \\ n_2, & y_1 < y < y_2 \\ \vdots & \vdots \\ n_N, & y_{N-1} < y < y_N \\ n_s, & y_N < y \end{cases} \tag{3.9}$$

where n_l is the refractive index of the *l*-th layer, y_l is the position of interface between the *l*-th layer and the (*l+1*)-th layer, and n_s and n_0 are refractive index of substrate and top cladding materials as shown in Figure 3.6.

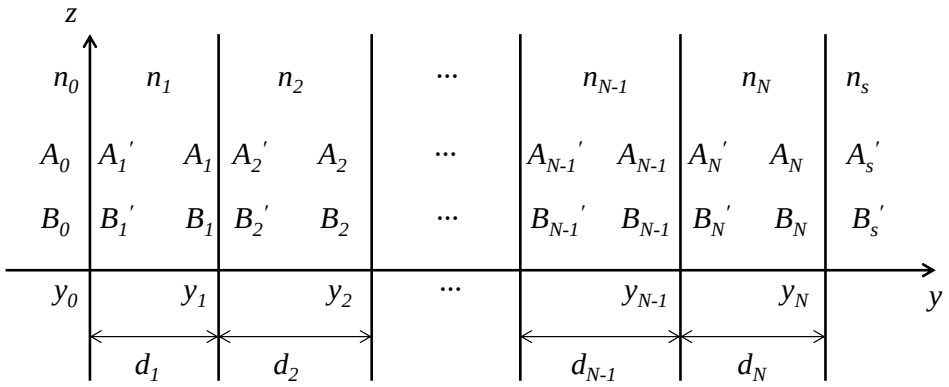

Figure 3.6 A multilayer medium system

The thickness d_N of each layer is

$$\begin{aligned} d_1 &= y_1 - y_0 \\ d_2 &= y_2 - y_1 \\ &\vdots \\ d_N &= y_N - y_{N-1} \end{aligned} \tag{3.10}$$

The wave equation with the electric field can be obtained from Maxwell's equations

$$\left[\frac{d^2}{dy^2} + \left(\frac{\omega}{c} n \right)^2 - \beta^2 \right] \vec{E}_m(y) = 0 \tag{3.11}$$

where β is a propagation constant what we are looking for, and *m* denotes mode number, and these modes are mutually orthogonal.

The electric field of a general plane-wave solution of the above equation is

$$E = E(y) e^{i(\omega t - \beta z)} \tag{3.12}$$

Note that the mode number is dropped since we are interested in the fundamental mode. The electric field distribution $E(y)$ can be expressed as

$$E(y)=\begin{cases} A_0 e^{-ik_{0y}(y-y_0)}+B_0 e^{ik_{0y}(y-y_0)}, & y<y_0 \\ A_N e^{-ik_{Ny}(y-y_N)}+B_N e^{ik_{Ny}(y-y_N)}, & y_{N-1}<y<y_N \\ A_s' e^{-ik_{sy}(y-y_N)}+B_s' e^{ik_{sy}(y-y_N)}, & y_N<y \end{cases} \tag{3.13}$$

where k_{ly} is the *y* component of the wave vectors given by

$$k_{ly}=\left[\left(n_l\frac{\omega}{c}\right)^2-\beta^2\right]^{1/2} \tag{3.14}$$

and is related to the propagation angle θ_l by geometric optics treatment

$$k_{ly}=n_l\frac{\omega}{c}\cos\theta_l \tag{3.15}$$

The electric field *E*(*y*) consists of a right- and left-travelling wave in each layer as

$$E(y)=A_l e^{-ik_{ly}(y-y_l)}+B_l e^{ik_{ly}(y-yl)}=A_l(y_l)+B_l(y_l) \tag{3.16}$$

For the matrix method, we define

$$\begin{aligned} &A_1=A(y_0^-),\ B_1=B(y_0^-), \\ &A_2'=A(y_0^+),\ B_2'=B(y_0^+), \\ &A_2=A(y_1^-),\ B_2=B(y_1^-), \\ &\qquad\vdots \\ &A_N'=A(y_{N-1}^+),\ B_N'=B(y_{N-1}^+), \\ &A_N=A(y_N^-),\ B_N=B(y_N^-), \\ &A_s'=A(y_N^+),\ B_s'=B(y_N^+), \end{aligned} \tag{3.17}$$

where y_N^- represent the left side of the interface, $y=y_N$, and y_N^+ represent the right side of the same interface.

Using the Eq. (3.2) and (3.6), we can write

$$\begin{pmatrix} A_0 \\ B_0 \end{pmatrix} = D_0^{-1} D_1 \begin{pmatrix} A_1 \\ B_1 \end{pmatrix}, \\ \begin{pmatrix} A_l \\ B_l \end{pmatrix} = P_l D_l^{-1} D_{l+1} \begin{pmatrix} A_{l+1} \\ B_{l+1} \end{pmatrix}, \tag{3.18}$$

where P_l is layer matrix which is

$$P_l = \begin{pmatrix} e^{i\phi_l} & 0 \\ 0 & e^{-i\phi_l} \end{pmatrix} \tag{3.19}$$

with

$$\phi_l = k_{ly} d_l \tag{3.20}$$

Now the relation between top cladding and substrate field amplitude, A_0, B_0 and $A_s^{'}$, $B_s^{'}$, can thus be expressed as

$$\begin{pmatrix} A_0 \\ B_0 \end{pmatrix} = \begin{pmatrix} M_{11} & M_{12} \\ M_{21} & M_{22} \end{pmatrix} \begin{pmatrix} A_s^{'} \\ B_s^{'} \end{pmatrix} \tag{3.21}$$

and the matrix M is given by

$$\begin{pmatrix} M_{11} & M_{12} \\ M_{21} & M_{22} \end{pmatrix} = D_0^{-1} \left[\prod_{l=1}^{N} D_l P_l D_l^{-1} \right] D_s \tag{3.22}$$

In medium 0, the right-travelling wave A_0 would go zero when *y* approaches to -∞, and likewise in medium *s*, the left-travelling wave $B_s^{'}$ would go zero when *y* approaches to ∞. Then the new relation between amplitudes in the waveguide is

$$\begin{pmatrix} 0 \\ B_0 \end{pmatrix} = \begin{pmatrix} M_{11} & M_{12} \\ M_{21} & M_{22} \end{pmatrix} \begin{pmatrix} A_s^{'} \\ 0 \end{pmatrix} \tag{3.23}$$

which indicates

$$M_{11}(\beta) = 0 \tag{3.24}$$

Roots that satisfy the Eq. (3.24) are the propagation constants in the waveguide.

3.1.2 Optimization of Shallow Ridge Waveguide for Athermal Performance

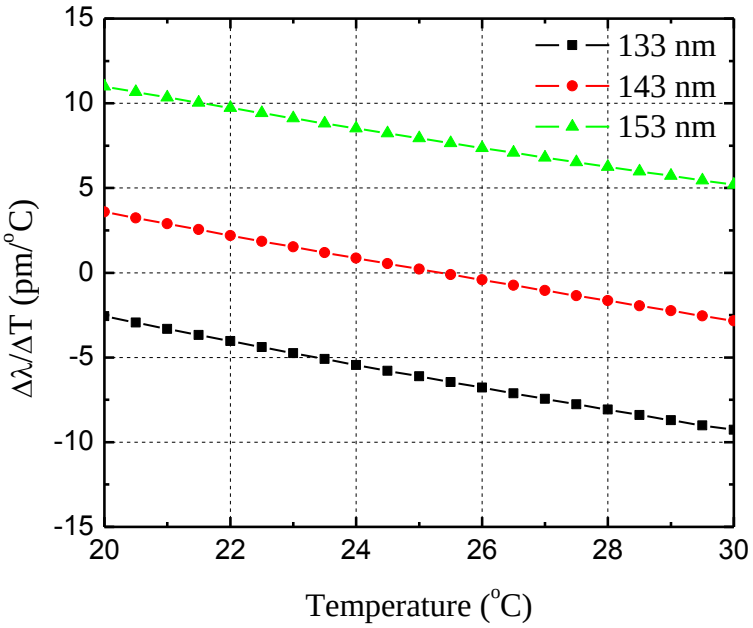

Figure 3.7. Temperature derivation of effective index of TM mode for three different core thickness; 133, 143, and 153 nm

Typical 200 nm silicon thickness on an SOI wafer provides tight vertical confinement in silicon for a TM mode waveguide, and therefore the thermal effect in waveguide is dominated by silicon. The thermo-optic coefficient of H_2O is nearly a half of Si but negative. This means the thermal effect in silicon can be eliminated if the optical confinement in H_2O is doubled than in Si. For shallow-ridge waveguide, the optical

confinement can be precisely controlled by using different silicon thicknesses via thermal oxidation technique [65].

Figure 3.7 shows the calculated derivative of the ring resonator resonant frequency shift as a function of temperature for TM mode operation using three different Si core thicknesses which are 133, 143, and 153 nm. It is seen that the value of 143 nm predicts a zero temperature derivative at a room temperature of ~ 25 ℃. The athermal relationship between waveguide modal index change Δn and resonant wavelength shift is

$$0 = \frac{\Delta\lambda}{\Delta T} = \frac{\lambda}{n_g}\frac{\Delta n_{eff}}{\Delta T} \tag{3.25}$$

If we miss the target thickness by ± 1 nm, we can simply shift operation temperature by ± 1 ℃. We thinned the Si thickness by oxidation in the furnace at 975 ℃ to a target value of ~144 nm, and removed the resulting oxide with HF. Using a microscope, the cross section image was obtained after the fabrication and shown in Figure 3.8. The bright yellow is Si, light brown is SiO_2, and top brown layer is air. We can see the thin Si device layer is sandwiched by SiO_2 claddings.

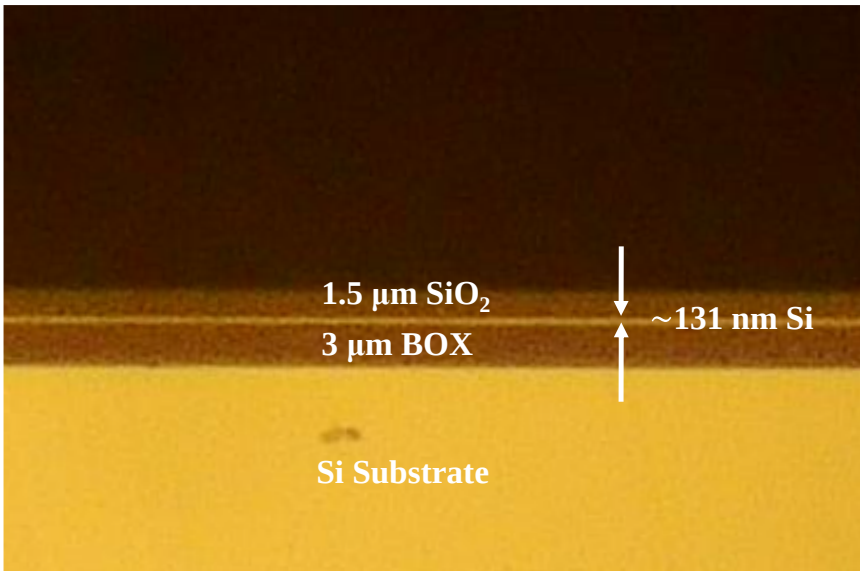

Figure 3.8. Cross section of fabricated silicon chip

For the optimization of waveguide structure, we plot the calculated weighting function in Figure 3.9 (a) within a 5 nm biological layer while varying the silicon slab thickness in water for both TE and TM modes at 1.31 µm wavelength. And we can clearly see the TM mode has higher surface sensitivity than TE mode overall, and especially at the optimum thickness of 183 nm for TM mode, it has 4.4 times higher sensitivity than TE mode. For this particular structure this means that the TM mode will see 4.4 times larger modal change for any events in the biological layer. In addition, this thickness ensures the single mode operation for both TE and TM mode.

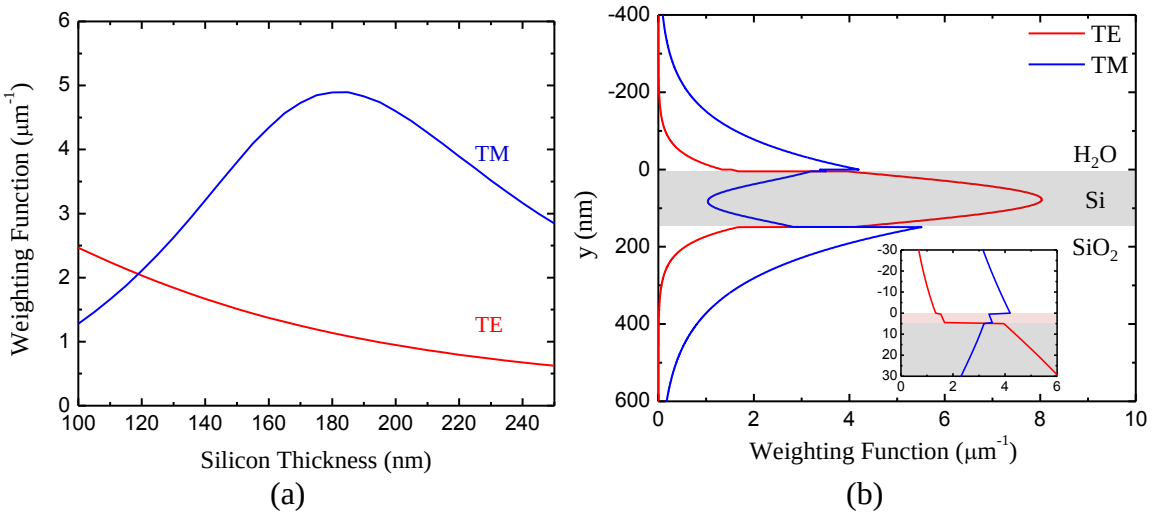

Figure 3.9. (a) Magnitude of weighting function of TE and TM modes denoted with red and blue lines respectively for a 5 nm biolayer above the silicon waveguide surface in H_2O as a function of silicon slab thickness and (b) weighting functions for 144 nm silicon waveguide. The inset is zoomed weighting functions near the biological layer for both polarizations.

Figure 3.9 (b) illustrates the weighting function *f*(*y*) for TE and TM mode with red and blue lines respectively when the silicon waveguide is 144 nm, and also a close-up plot of weighting functions above the silicon surface are plotted together in the inset. We can see in the inset that TM mode has 2.1 times higher sensitivity to the index change of thin biolayer than that of TE mode which makes TM mode very attractive for the surface sensing.

It is important to note that, for the 1.31 μm operation, our calculations indicate that this 143 nm thickness only results in a 30 % reduction in sensitivity for surface bound species

for the 143 nm thickness relative to the optimum thickness of 183 nm as shown in Figure 3.9 (b).

3.2 Verification of Athermal Performance

For the examination of athermal performance of SOI waveguide, we used 400 μm ring resonators thinned to a target thickness of 143 nm.

The samples were exposed to an aqueous solution with the local microfluidic chamber temperature controlled by a thermoelectric cooler (TEC), and a tunable laser tracks the resonant wavelength shift while scanning temperature. The experimental blue squares of Figure 3.10 show near-perfect cancellation of thermo-optic effect of the TM mode near 28 ℃ for a fitted silicon thickness of 145 nm, in very good agreement with the modeled predictions (blue line) based on the Eq. (2.11). Note that this very high degree of temperature independence is in stark contrast to the very high temperature dependence for TE mode operation, which is shown theoretically (red dashed line) and experimentally (red triangles). We have also measured waveguides with slightly different core thicknesses by 13 Å which confirm the predictions shown in Figure 3.7 and this is shown in Figure 3.11. Red circular points are measured data and solid line is calculated fit from the measurement which indicates the silicon thickness is 143.7 nm, and blue data are from Figure 3.10 of TM mode. Both red and blue lines which are numerically calculated fits using Eq. (2.11) show very close matching with experimental data.

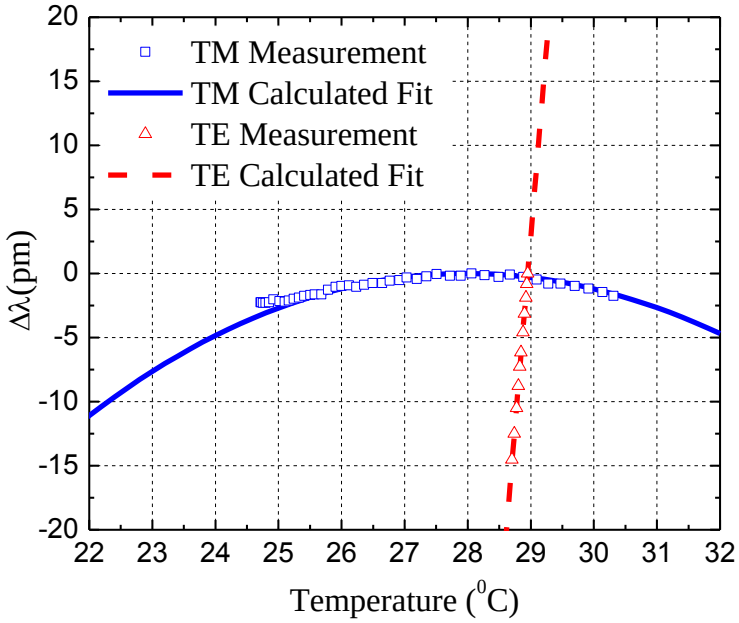

Figure 3.10. Experimental and theoretical curves of resonator wavelength shift with temperature for TM (blue) and TE (red)

Temperature fluctuation of ± 0.1℃ at the optimum operation temperature of 26.1℃, for 143.7 nm thick waveguides, causes wavelength shift of ± 6 pm for TE mode, but TM mode only shows ± 0.02 pm which is very high degree of athermal operation.

We believe the magnitude of noise seen in the experimental data, which is much larger than our system noise and ultimate sensitivity, results from mechanical drift of setup due to the thermal expansion.

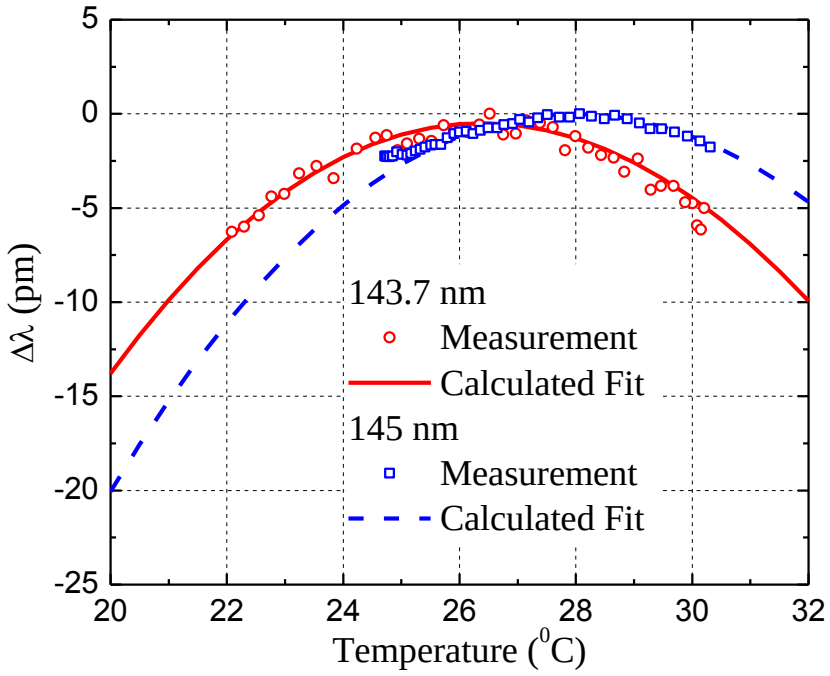

Figure 3.11. Comparison of two chips with slightly different thicknesses

3.3 Summary

We have presented nearly perfect athermal operation of silicon waveguides for aqueous solution around 300 K. A high degree of temperature independence for shallow ridge waveguide operating in TM mode promises lower ambient noise for biosensor application and improvement in performance. While active temperature control of SOI waveguides can be realized by embedding thin-film Pt surface heaters [39], this still poses difficulties in accurate temperature monitoring and low-noise, stable active control servo circuits. An athermal SOI waveguide, on the other hand, has an intrinsic property of temperature independence based on material or design engineering and is an ideal approach for the optical integration. This configuration may be advantageous in enabling

simpler, faster, lower-cost sensor readout methods than are possible using reference techniques.

There have been approaches to athermalize SOI ring resonator using polymer claddings for WDM optical communication [66], [67], but using H_2O as a cladding may provide simple and cost effective manners, especially when the sensed species is anticipated to be in an aqueous environment.

Chapter 4

Harmonic Dithering Feedback Technique for a High-Sensitivity Biosensor

A large evanescent electric field on a silicon surface for TM mode SOI biosensors allows for high-sensitivity chemical and biological sensing of both thin adsorbed biomolecular layers and bulk homogeneous solutions. SOI waveguide biosensors on a ring resonator configuration with the low detection limit are reported [18], [19], but their expensive and large tunable laser instrumentation is problematic, and also their maximum performance is limited because of the large, unavoidable *1/f* noise contributions.

These techniques also typically require a reference ring to read relative wavelength shift because of the instability from the mechanical actuator in external cavity tunable laser system [18]. Finally, the slow wavelength scanning speed for the high-precision data acquisition limits the measurement speed to several seconds [18],[19].

We propose a simple and inexpensive dithering technique with a DFB laser and a lock-in amplifier based on the TM-mode SOI shallow-ridge waveguide ring resonator [68]. In this chapter, the dithering technique is detailed based on the SOI ring waveguide, and we analyze the system noise in frequency domain.

4.1 Harmonic Dithering Feedback Technique

At low modulation frequencies, for example below 1 MHz, the current modulation of laser diode renders the optical frequency modulation because of the thermal modulation of laser [69]. Specifically, changing the injection current induces change in refractive index of gain medium due to the temperature and causes optical frequency shift. The frequency response of DFB laser at DC is typically 1 GHz/mA, but when we increase the modulation frequency, the frequency response starts to decrease because of slow thermal response [70].

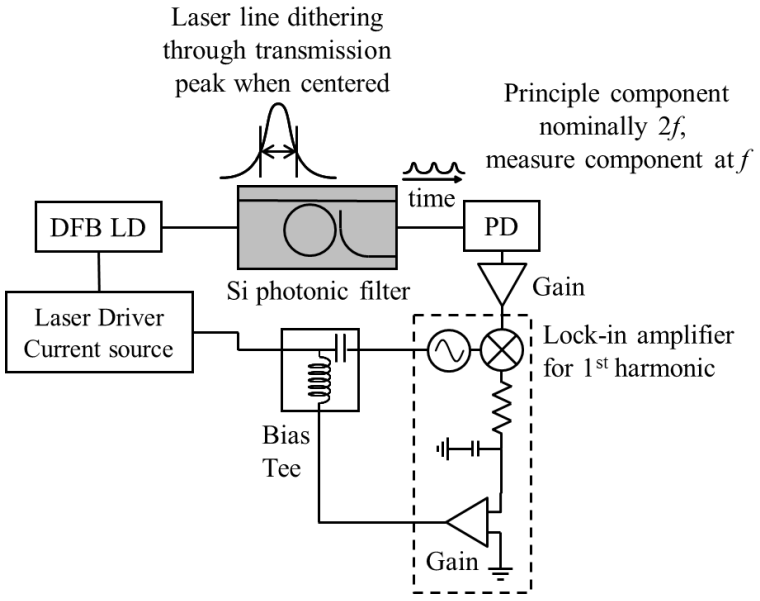

Figure 4.1. Experimental setup for the harmonic dithering technique

We harmonically dither the laser drive current on the Lorentzian shape resonator signal of SOI ring waveguide at high enough frequency to minimize the impact of *1/f* noise, and

feed the resulting photodetector signal to the lock-in. The experimental setup for the feedback technique is illustrated in Figure 4.1.

When the position of resonant frequency is exactly in the center of dither amplitude, in Figure 4.2 with the solid line, lock-in gives out nothing because the transmitted signal intensity has no component at the first harmonic. As the resonant frequency deviates from the center by δ due to sensing, the optical signal starts to have odd harmonic signals as shown in Figure 4.2 with the dashed line. The lock-in picks up the first harmonic signal and generates the DC output after a narrow low-pass filter.

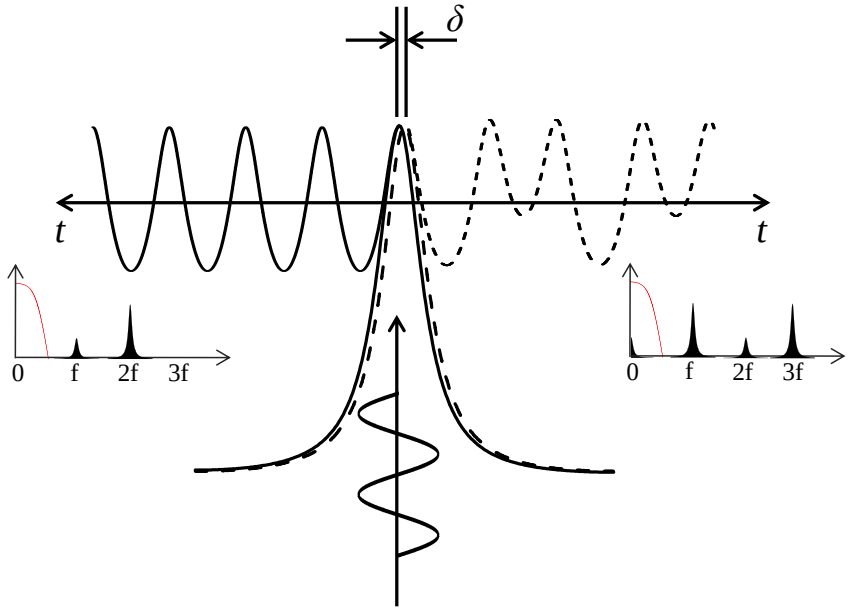

Figure 4.2. Temporal Lorentzian transmission lines and their PSD signal in frequency domain for small frequency deviation δ. A low-pass filter removes higher order signals and broadband noise.

This output signal is further amplified and goes as feedback into the DFB laser through a bias tee to minimize the first harmonic signal. We can reduce noise again by averaging the feedback signal or using additional filtering. When the feedback loop gain is large enough, the optical signal always stays in the same position with zero first harmonic and provides a large dynamic range of measurement. In this circumstance, the feedback signal itself then provides the sensor output as it is a direct measure of the shift required by the DFB laser to stay centered on the Lorentzian transmission curve. The dashed box in Figure 4.1 is the digital part of lock-in amplifier.

4.2 Principle of a Lock-In Amplifier

Lock-in amplifiers are used to measure very small signals buried in noise using phase-sensitive detection (PSD) technique [71]. By measuring the synchronous system response from an incoming AC signal, the DSP lock-in amplifier can detect very small changes. The block diagram DSP lock-in amplifier is shown in Figure 4.1 with internal oscillator, linear multiplier, low-pass filter, and amplifier. The 16-bit analog-to-digital converter (ADC) locates between receiver and lock-in amplifier with a sampling rate of 256 kHz.

Lock-in amplifier can increase the signal-to-noise ratio by narrowing the bandwidth of low-pass filter at an interested frequency. For example, suppose we have a 10 nV sine wave signal. Obviously we need some amplification to see such small signal, and typical voltage amplifier has the input noise of $5\text{nV}/\sqrt{\text{Hz}}$. If we try to measure or see the signal after the amplifier with bandwidth of 100 kHz, our effort turns into vain because of poor

SNR of $\frac{(10\text{nV})^2}{(5\text{nV}/\sqrt{\text{Hz}}\times\sqrt{100\text{kHz}})^2}=0.0004$. However if we could narrow the bandwidth to 1 Hz, SNR increases to 4. With much narrower bandwidth of 0.01 Hz, SNR increases up to 400.

If a signal that we have is

$$v_{in}=v_s\sin(\omega_s t+\theta_s) \tag{4.1}$$

and the lock-in amplifier needs a reference signal which is

$$v_{ref}=v_r\sin(\omega_r t+\theta_r) \tag{4.2}$$

The PSD or linear multiplier in the lock-in amplifier multiplies these two signals together, and the output signal from PSD is

$$\begin{aligned} v_{PSD} &= v_s v_r\sin(\omega_s t+\theta_s)\sin(\omega_r t+\theta_r) \\ &= \frac{1}{2}v_s v_r\cos(\omega_s t-\omega_r t+\theta_s-\theta_r)-\frac{1}{2}v_s v_r\cos(\omega_s t+\omega_r t+\theta_s+\theta_r) \end{aligned} \tag{4.3}$$

We have two different signals in frequency, but ω_s and ω_r are same frequency driven by the internal oscillator

$$v_{PSD}=\frac{1}{2}v_s v_r\cos(\theta_s-\theta_r)-\frac{1}{2}v_s v_r\cos(2\omega t+\theta_s+\theta_r) \tag{4.4}$$

and latter 2ω part will be removed after low-pass filtering. Now what we have the DC signal

$$v_{PSD}=\frac{1}{2}v_s v_r\cos(\theta_s-\theta_r) \tag{4.5}$$

Since θ_s and θ_r do not have time dependence, the output signal from PSD is clean DC signal, and there is a phase shifter that makes the phase difference to be zero for the maximum output. In our application, PSD output is the first harmonic component from the optical transmission from the ring biosensor.

Let us consider a simple RC circuit, a low-pass filter of lock-in, as shown in Figure 4.3. V_{out} is the voltage across the capacitor *C*, and the transfer function is

$$\left|H(\omega)\right| = \left|\frac{V_{out}(\omega)}{V_{in}(\omega)}\right| = \frac{1}{\sqrt{1+\left(RC\omega\right)^2}} \tag{4.6}$$

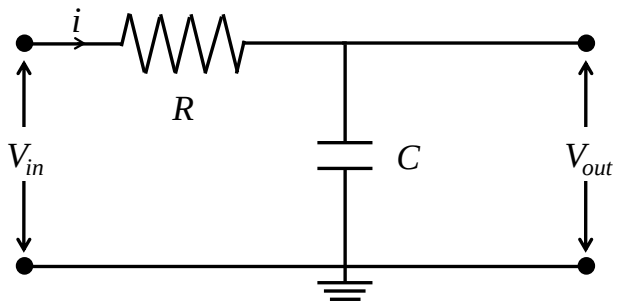

Figure 4.3. Circuit diagram of a low-pass filter

To see the transition of filter output as a function of time, we define a constant input voltage in time $V_{in}(t) = V_0$, and its Laplace transform is

$$\mathcal{L}\{V_{in}(t)\} = \int_0^\infty e^{-st} V_0 dt = \frac{V_0}{s} \tag{4.7}$$

Resulting output voltage of low-pass filter from Eq. (4.6) is

$$V_{out}(s) = \frac{V_0}{s(1+RCs)} \tag{4.8}$$

Inverse Laplace transformation yields

$$\mathcal{L}^{-1}\{V_{out}(s)\} = \frac{1}{2\pi i}\lim_{T\to\infty}\int_{\gamma-i\infty}^{\gamma+i\infty} e^{st}\,\frac{V_0}{s(1+RCs)}ds = V_0(1-e^{-\frac{t}{RC}}) \tag{4.9}$$

And Taylor expansion of output signal in time when $t \approx 0$ will give us the time response of low-pass filter by

$$V_0(1-e^{-\frac{t}{RC}})\Big|_{t=0} = V_0\frac{t}{RC} - V_0\left(\frac{t}{RC}\right)^2 + \ldots \tag{4.10}$$

We can clearly see that the single-pole circuit has linear time response. The time response of *n*-th order RC circuit is

$$V_{out}(t)\big|_{t=0} = \frac{V_0}{n!}\left(\frac{t}{RC}\right)^n = \frac{V_0}{n!}\left(\frac{t}{\tau}\right)^n \tag{4.11}$$

and plotted in Figure 4.4 up to four successive low-pass filters where τ is time constant setting of lock-in. Higher order low-pass filters have nonlinear time response and slowly respond to any change.

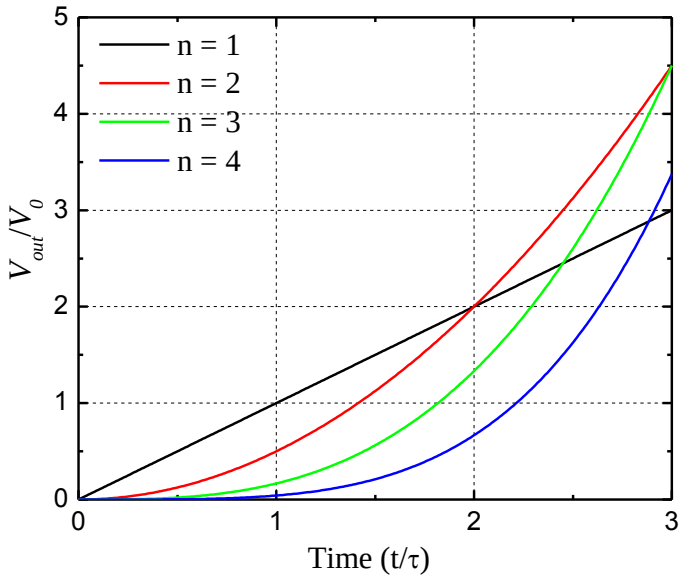

Figure 4.4. Time response of *n*-th order low-pass filter

It is desirable to use 6 dB/oct roll off low-pass filter for feedback because of its fast time response and stability. However, for the measurement in this thesis, 12 dB/oct roll off was used to decrease the noise further. And the voltage gain for feedback loop was ~ 120. When excessively large gain is used, it may cause oscillations in a feedback loop because of its slow time response.

Equivalent noise bandwidth (ENBW) for single-pole and double-pole filters can be easily calculated from Eq. (4.6) by integrating over whole frequency range

$$\begin{aligned} &\text{6dB/oct}: && B = \frac{1}{2\pi}\int_0^\infty |H(\omega)|^2 d\omega = \frac{1}{4RC} = \frac{1}{4\tau} \\ &\text{12dB/oct}: && B = \frac{1}{2\pi}\int_0^\infty |H(\omega)|^4 d\omega = \frac{1}{8RC} = \frac{1}{8\tau} \end{aligned} \tag{4.12}$$

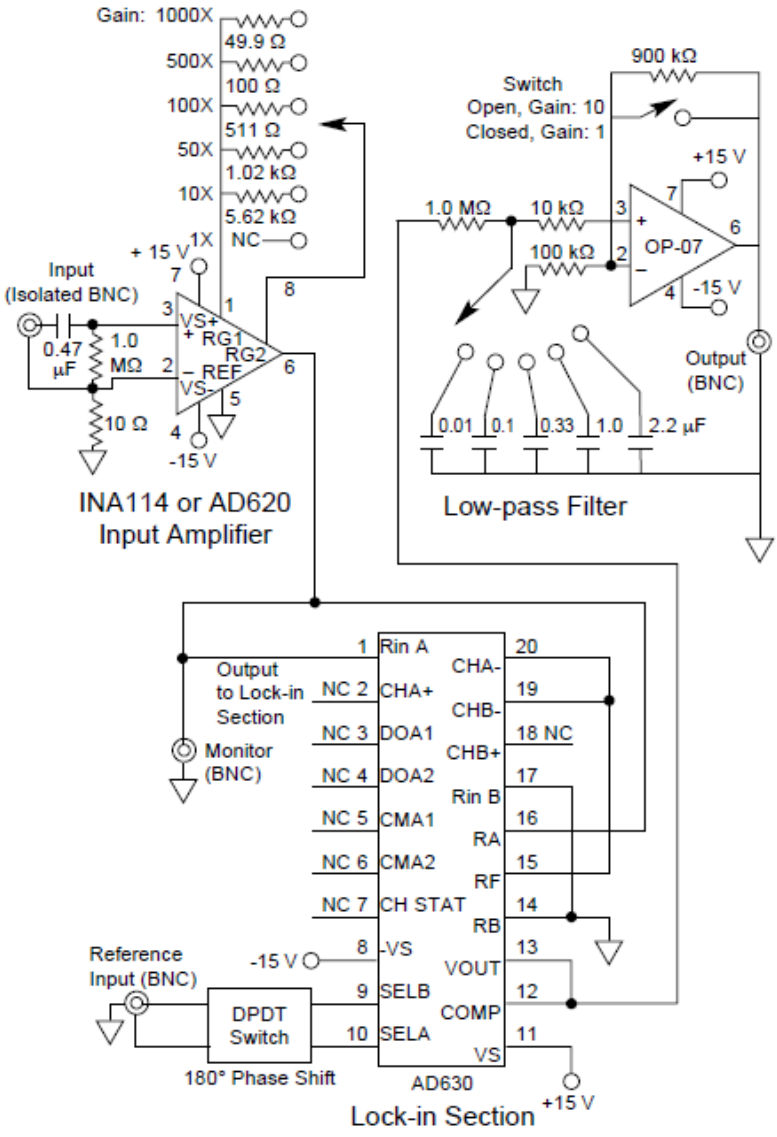

Figure 4.5. The example of DSP lock-in amplifier composed of only three integrate circuits [71]

In the context of a future, commercially-implemented biosensor system, we anticipate that the current bulky lock-in size and relatively high cost, primarily resulting from its high versatility and elaborate user interface, can be avoided by replacing the lock-in by

single Si application-specific integrated circuit (ASIC) chip. This ASIC would comprise a simple microprocessor, the amplifiers and very limited control functions, together with the oscillator and PSD and filters implemented digital signal processor, as illustrated in Figure 4.5 [71]. The fact that SOI technology has complementary metal–oxide–semiconductor (CMOS) compatibility even opens possibility to integrate all optical and electronic functions on a single low-cost chip at the same foundry.

4.3 Dither Theory

The Lorentzian lineshape function is given by

$$F(\nu) = \frac{1}{1 + \frac{4\cdot(\nu-\nu_0)^2}{\Delta\nu_{FWHM}^2}} \tag{4.13}$$

where $\Delta\nu_{FWHM}$ is the Full-Width-To-Half-Maximum of the Lorentzian resonance. Without losing generality, we reference frequency to ν_0, and normalize frequency $\tilde{\nu}$ to be in units of $\Delta\nu_{FWHM}/2$ such that a deviation of one unit takes the lineshape to its 50% point.

In this case the expression becomes simply

$$F(\tilde{\nu}) = \frac{1}{1+\tilde{\nu}^2} \tag{4.14}$$

We now propose to scan this lineshape with a sinusoidal dither with an amplitude A, and we further allow for an offset from the peak of the lineshape by an amount δ such that

$$\tilde{\nu} = \delta + A\sin(\Omega t) \tag{4.15}$$

and a signal passing through a filter with the Lorentzian transmission will have a current or voltage proportional to

$$S(x) \;=\; \frac{1}{1+\left(\delta + A\sin(x)\right)^2} \tag{4.16}$$

where, for further mathematical simplification, we have let $x \equiv \Omega t$.

This signal is to be measured using phase-synchronous detection (PSD) with a lock-in amplifier, which is essentially measuring the Fourier series components of the signal at a harmonic chosen by the lock-in, i.e.,

$$S(x) \;=\; \frac{a_0}{2} + \sum_{n=1}^{\infty}\left[a_n\cos(nx) + b_n\sin(nx)\right] \tag{4.17}$$

Where

$$a_n \;=\; \frac{1}{\pi}\int_{-\pi}^{\pi} S(x)\cos(nx)dx \tag{4.18}$$

and

$$b_n \;=\; \frac{1}{\pi}\int_{-\pi}^{\pi} S(x)\sin(nx)dx \tag{4.19}$$

We will focus our attention on just the first harmonic, $n=1$, and inspection of the symmetry of $S(x)$ reveals that $a_1 = 0$. This can be seen by decomposing the range of integration into two parts,

$$\begin{aligned} a_1 &= \frac{1}{\pi}\int_{-\pi}^{0}\frac{\cos(x)dx}{1+\left(\delta+A\sin(x)\right)^2} + \frac{1}{\pi}\int_{0}^{\pi}\frac{\cos(x)dx}{1+\left(\delta+A\sin(x)\right)^2} \\ &= \frac{1}{\pi}\int_{0}^{\pi}\frac{\cos(x)dx}{1+\left(\delta-A\sin(x)\right)^2} + \frac{1}{\pi}\int_{0}^{\pi}\frac{\cos(x)dx}{1+\left(\delta+A\sin(x)\right)^2} \end{aligned} \tag{4.20}$$

Letting $y = x - \pi/2$ in each term converts this to

$$a_1 = \frac{1}{\pi}\int_{-\frac{\pi}{2}}^{\frac{\pi}{2}}\frac{\sin(x)dx}{1+\left(\delta+A\cos(x)\right)^2} + \frac{1}{\pi}\int_{-\frac{\pi}{2}}^{\frac{\pi}{2}}\frac{\sin(x)dx}{1+\left(\delta-A\cos(x)\right)^2} \tag{4.21}$$

and both integrals can be seen to be an odd function of x over an even range of integration, thus yielding zero.

The coefficient of the $\sin(x)$ term of the series, b_1, does not in general vanish and is given by

$$b_1 = \frac{1}{\pi}\int_{-\pi}^{\pi}\frac{\sin(x)dx}{1+\left(\delta+A\sin(x)\right)^2} \tag{4.22}$$

While at $\delta = 0$ this is also an odd function of *x* over an even range and thus vanishes, for non-zero δ this does not vanish, and inspection of the integral reveals that it is an odd function δ. The concept of the sensor is use the relationship between δ and b_1 to determine δ through a measurement of b_1 using PSD with the lock-in at the fundamental harmonic. While the integral above can be evaluated analytically, the expression is rather complicated and is given in Appendix A. However, because we will be using a feedback

circuit, we will be generally be concerned with small deviations δ, and thus we can use just the derivative of b_1 with respect to δ because

$$\Delta b_1 \quad = \quad \left.\frac{\partial b_1}{\partial \delta}\right|_{\delta=0} \cdot \delta \quad + \quad \ldots \tag{4.23}$$

We can take this derivative directly inside the integral to get

$$\frac{\partial b_1}{\partial \delta} \quad = \quad \frac{1}{\pi}\int_{-\pi}^{\pi} \frac{-2\left(\delta + A\sin(x)\right)\sin(x)dx}{\left(1+\left(\delta + A\sin(x)\right)^2\right)^2} \tag{4.24}$$

and thus

$$\left.\frac{\partial b_1}{\partial \delta}\right|_{\delta=0} \quad = \quad \frac{1}{\pi}\int_{-\pi}^{\pi} \frac{-2A\sin^2(x)dx}{\left(1+A^2\sin^2(x)\right)^2} \quad = \quad \frac{4}{\pi}\int_{0}^{\frac{\pi}{2}} \frac{-2A\sin^2(x)dx}{\left(1+A^2\sin^2(x)\right)^2} \tag{4.25}$$

This integral can be done analytically by noting that we can consider $\left.\frac{\partial b_1}{\partial \delta}\right|_{\delta=0}$ to be a function of A, i.e.,

$$\left.\frac{\partial b_1}{\partial \delta}\right|_{\delta=0} \equiv F(A) \tag{4.26}$$

We can then show that $F(A)$ is perfectly integrable in the variable A and determine (by exchanging the order of integration)

$$\int_0^A F(\tilde{A})d\tilde{A} \quad = \quad \frac{4}{\pi}\int_0^{\frac{\pi}{2}}\int_0^A \frac{-2\tilde{A}\sin^2(x)d\tilde{A}}{\left(1+\tilde{A}^2\sin^2(x)\right)^2}dx \tag{4.27}$$

If we can evaluate this analytically we can then just differentiate the result to get $F(A)$. This integral in $\tilde{A}$ is easily done by letting

$$y = 1 + \tilde{A}^2 \sin^2(x) \tag{4.28}$$

and thus

$$dy = 2\tilde{A}\sin^2(x)\, d\tilde{A} \tag{4.29}$$

and we have

$$\int_0^A F(\tilde{A})d\tilde{A} = \frac{4}{\pi}\int_0^{\frac{\pi}{2}} \int_1^{1+A^2\sin^2(x)} \frac{-dy}{y^2}dx = \frac{4}{\pi}\int_0^{\frac{\pi}{2}} \left[\frac{1}{y}\Big|_1^{1+A^2\sin^2(x)} \right] dx = \frac{4}{\pi}\int_0^{\frac{\pi}{2}} \left[\frac{1}{1+A^2\sin^2(x)} - 1 \right] dx \tag{4.30}$$

Noting that the second term will have no dependence on A, we will have

$$\left.\frac{\partial b_1}{\partial \delta}\right|_{\delta=0} \equiv F(A) = \frac{d}{dA}\left\{ \frac{4}{\pi}\int_0^{\frac{\pi}{2}} \frac{dx}{1+A^2\sin^2(x)} \right\} \tag{4.31}$$

This last definite integral is a common integral, which can also be evaluated with the residue theorem and integration in the complex plane, with the result

$$\int_0^{\frac{\pi}{2}} \frac{dx}{1+A^2\sin^2(x)} = \frac{\pi}{2\sqrt{1+A^2}} \tag{4.32}$$

and then performing the differentiation in A indicated gives the final result

$$\left.\frac{\partial b_1}{\partial \delta}\right|_{\delta=0} \equiv F(A) \quad = \quad \frac{-2A}{\left(1+A^2\right)^{\frac{3}{2}}} \tag{4.33}$$

This gives the desired PSD signal for small deviations δ as noted earlier. We are also in a position to determine analytically what the optimum dither amplitude A is, i.e., by maximizing $\left.\frac{\partial b_1}{\partial \delta}\right|_{\delta=0}$ as a function of A,

$$\frac{\partial}{\partial A}\left(\left.\frac{\partial b_1}{\partial \delta}\right|_{\delta=0}\right) \quad = \quad \frac{\partial}{\partial A}\left(\frac{-2A}{\left(1+A^2\right)^{\frac{3}{2}}}\right) \quad = \quad \frac{4A^2-2}{\left(1+A^2\right)^{\frac{5}{2}}} \quad = \quad 0 \tag{4.34}$$

which requires that $A_{opt} = 1/\sqrt{2} = 0.71$, 71% across the FWHM of the lineshape. The behavior of this derivative as a function of normalized dither amplitude is shown in Figure 4.6.

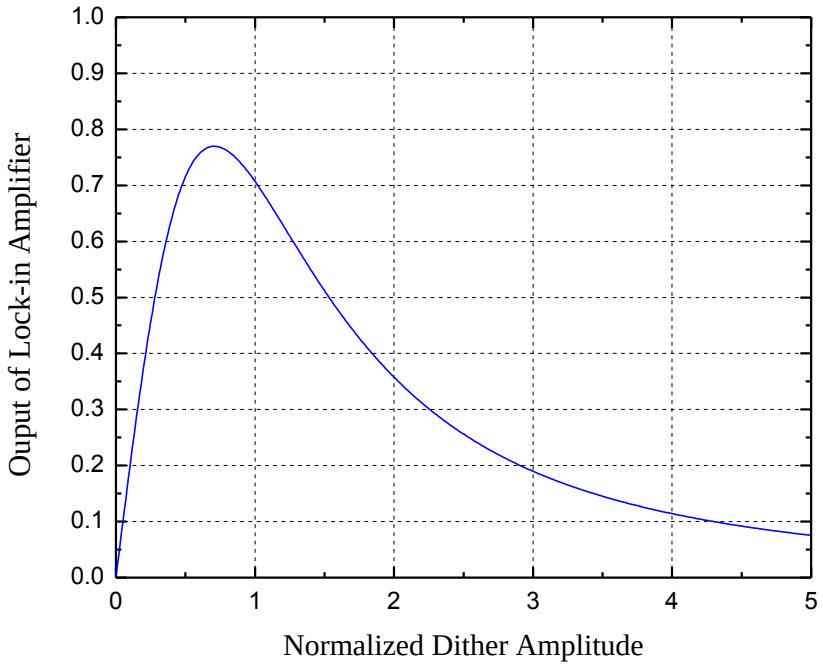

Figure 4.6. Derivative of harmonic amplitude with derivation

The negative sign of (4.33) can be eliminated by properly adjusting the phase information of PSD in a lock-in amplifier before we use. The DC level of $S(x)$ is $a_0 = 2/\sqrt{1+A^2}$ and filtered out by using the AC coupling method of lock-in amplifier.

The time averaged electrical power measured in this fundamental harmonic is then given at this optimized dither by

$$\left\langle P_{signal} \right\rangle_{harmonic} \quad \propto \quad \frac{1}{2}\left(\Delta b_1\right)^2 = \frac{8}{27}\cdot\delta^2 \tag{4.35}$$

We can compare this with the "direct measurement" DC method, biased at the 50% transmission point, where the signal change results trivially from the transmission change

with the deviation δ . It is easy to show that, for deviations δ from this bias point, the signal is

$$S(\delta) = \frac{1}{1+(\delta+1)^2} \tag{4.36}$$

and at this 50% transmission point the first derivative is evaluated as $S'(\delta=0)=-1/2$ so for a small deviation of δ the power of the deviation signal becomes

$$\left\langle P_{signal} \right\rangle_{DC} \propto (\Delta S)^2 = \frac{1}{4}\delta^2 \tag{4.37}$$

We thus see that we have actually increased the measured signal power by using the harmonic dither method, for small values of δ, by the ratio of 32/27 or an 18.5% improvement.

4.4 Analysis of Noise for Harmonic Dithering Feedback Technique

In this section, we examine the effectiveness of harmonic dithering technique for low-noise biosensor measurement methodology by using a data acquisition technique introduced in Appendix B.5.

Front-end of photodetector and lock-in for floating ground is illustrated in Figure 4.7, and with given parameters of instruments, the measurement bandwidth, for R_L << 10 MΩ, is

$$\Delta\nu_{3dB} = \frac{1}{2\pi \times R_L \times 26\,pF} \tag{4.38}$$

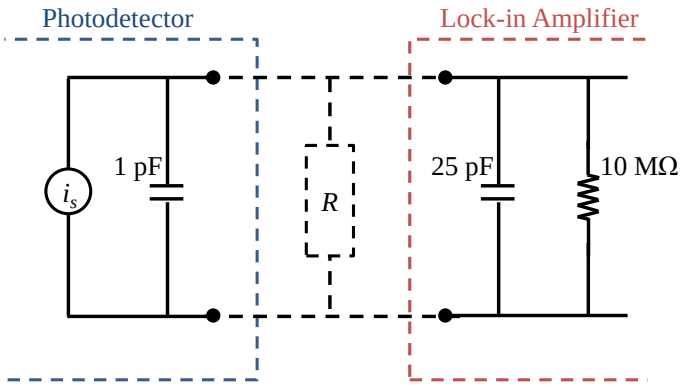

Figure 4.7. Front-end diagram of photodetector and lock-in with instrument specifications

With current setting of P_L = 30 mW, R_L = 50 kΩ, 30 dB loss in total, and RIN = -135 dBc/Hz at 20 kHz modulation frequency, we can estimate the noise before the preamplifier is $\langle v_n \rangle = 256.1\text{nV}/\sqrt{\text{Hz}}$ from Eq. (B.32). We can also observe that RIN and shot noise are dominant noise sources in the harmonic dithering measurement system; $\langle v_{RIN} \rangle = 213.4\text{nV}/\sqrt{\text{Hz}}$, $\langle v_{Shot} \rangle = 138.6\text{nV}/\sqrt{\text{Hz}}$, and $\langle v_{Them} \rangle = 28.6\text{nV}/\sqrt{\text{Hz}}$. The 50 kΩ input impedance limits the photodetector bandwidth to 118 kHz which is large enough not to attenuate first harmonic signal.

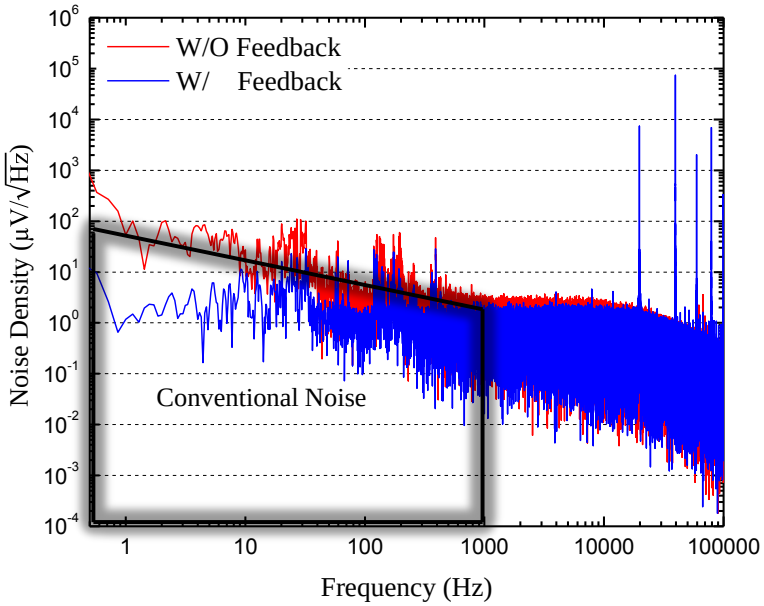

(a)

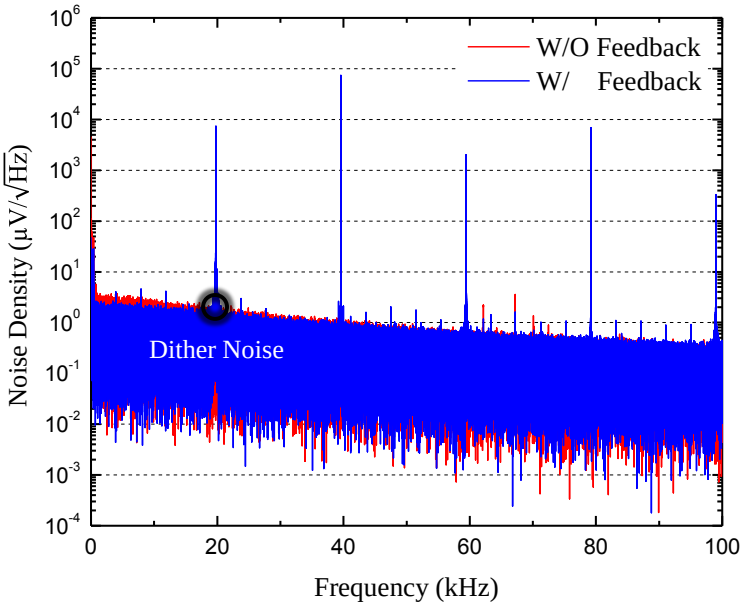

(b)

Figure 4.8. Photovoltage noise spectra with and without the feedback for the harmonic dithering technique in (a) log and (b) linear scales. The noise bandwidth of dithering technique is below 1 Hz while that of conventional method is typically 1000 Hz.

Figure 4.8 shows the photovoltage density spectra after calculating power spectral density of sensor signal in both linear and log scales for *x* axis. The DC conventional tunable laser instrumentation has a large noise bandwidth up to 1 kHz that includes *1/f* and many in-line noises. However the low-pass filter setting (12 dB/oct filter with 300 ms) used for the AC dithering technique guarantees the bandwidth slightly below 0.5 Hz from Eq. (4.12). During the spectral analysis, H_2O was continuously flowing on the sensor surface. The strong peak at 40 kHz is because dithering transmission has *2f* component, but we still see the signal at 20 kHz because of the current modulation of DFB laser. The flat noise floor for both measured spectra shows close match to the estimated noise floor of $\langle v_n \rangle = 256.1\text{nV}/\sqrt{\text{Hz}}$ at high frequency.

4.4 Revisiting Athermal Operation

Athermal operation of waveguides demonstrated using a tunable laser in Chapter 4 was confirmed again using the feedback technique and shown in Figure 4.9 for two different chips. Both upper plot from tunable laser and lower plot from feedback technique show the same trends for temperature change and the optimum operation at (a) 26.1℃ for 143.7 nm thick waveguide and (b) 28 ℃ for 145 nm. We believe that noise shown in Figure 4.9 is caused by drifts of optical fibers due to thermal expansion of mechanical setup while scanning the temperature, and significantly larger than our system noise and ultimate sensitivity.

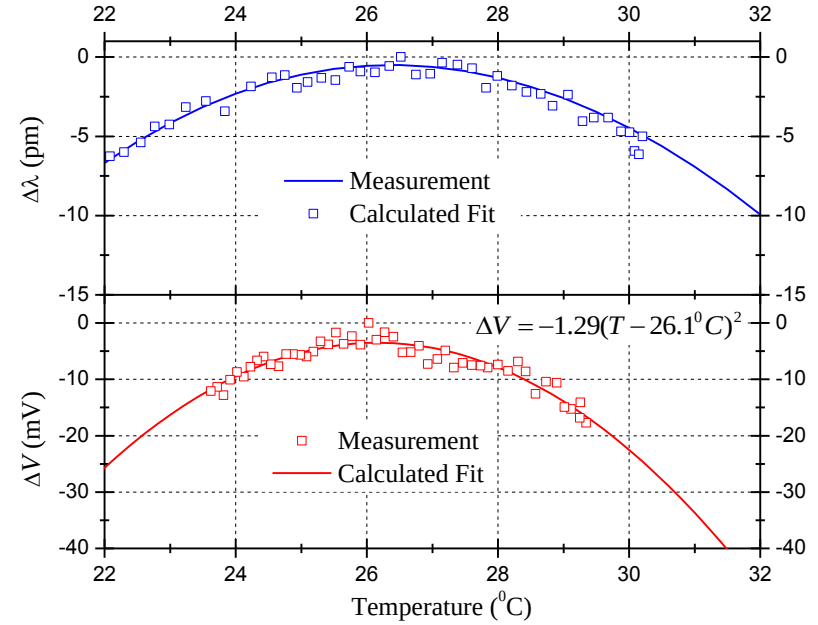

(a)

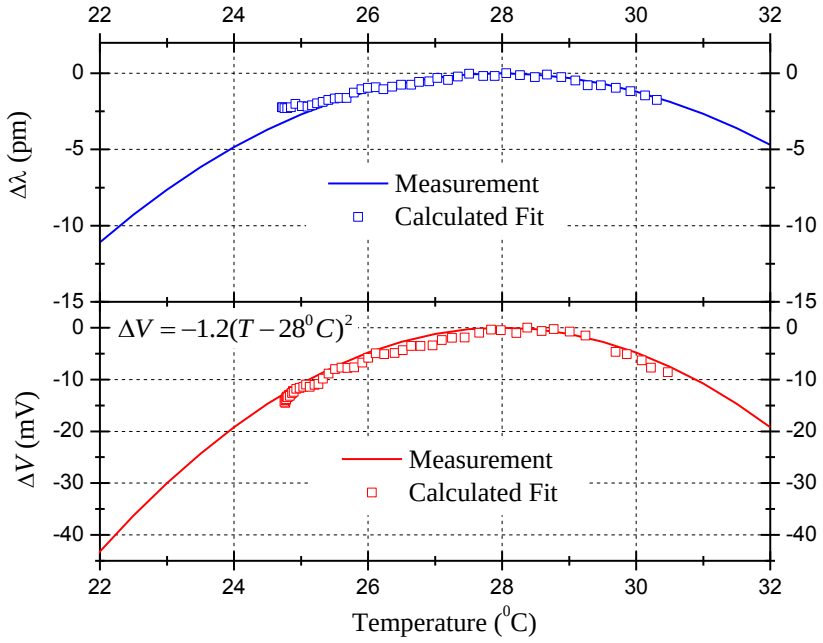

(b)

Figure 4.9. Comparison of athermal operation between tunable laser (upper plot) and feedback technique (lower plot) for (a) waveguide of 143.7 nm thickness that has the

optimum operation temperature of 26.1℃ and (b) 145 nm for 28℃ operation. Square experimental data and fitted line are shown together.

4.5 Summary

We have presented and analyzed the performance of a new signal readout method for high-sensitivity SOI waveguide biosensors that minimizes the *1/f* noise and easily allows for narrowing the noise bandwidth to a few hertz. Another feature of the harmonic dithering technique is that it does not forfeit the potential for real-time monitoring ability in microsecond level because of the high sampling rate of lock-in amplifier. The fact that SOI waveguide biosensors could ultimately be realized on a small silicon chip cost-effectively with a DSP lock-in and other electronic functions based on an ASIC technology makes our approach very attractive.

Chapter 5

High-Sensitivity and Label-Free Detection of Biomolecular Binding

Studies of the binding kinetics of chemical or bio molecular interactions using a biosensor with its real-time monitoring ability provide information about biological processes and rapid diagnostics for drug discovery applications [1], [13], [73]. For measurements of very small molecules < 500 Daltons or very low concentrations typically within the fM ~ nM range, fluorescently labeled is a common detection approach [74]. However, conjugating these tags may alter or deform the inherent characteristic of analytes or target molecules. In contrast, the label-free detection technique offers quantitative measurement and kinetic aspects of these interactions at a high accuracy by monitoring the binding of target molecules in their natural forms [75].

In previous chapters, developments of novel waveguide biosensors and techniques of low-noise detection were demonstrated. Herein we use both for high-sensitivity biosensing. First, bulk homogeneous refractive index sensing is demonstrated to provide calibrated results for the biomolecular interaction, and then surface sensing is presented

including the step-by-step procedure for experimental preparation. Lastly, we analyze the performance of the biosensor and discuss what our fundamental limits are.

5.1 Flow Control in Microfluidic System

Keeping constant flow rate is important in fluid delivery because change in the flow rate can disturb the thermal equilibrium in a biosensor, and thereby cause noise or drift in the sensor signal.

At the beginning, syringe pumps (New Era Pump Systems, Inc. [76]) were used to impose a flow rate directly to a biosensor. The significant advantage of using syringe pumps is accurate flow control across a microfluidic channel [77]. In contrast, one drawback of syringe pumps is the pulsation in flows especially at low flow rates [78], and this appears as a noise in signal. Another problem in syringe pump system occurs when we want to inject several different sample solutions to a microfluidic channel individually because they can be mixed at a manifold.

To prevent noise from syringe pumps, the use of hydrostatic pressure to control flow was devised. A computer-controlled mechanical fluid selector (Valco Instrument Co. Inc. [79]) was implemented between biosensor and sample to choose which solution to inject. The pressure difference is obtained by varying the height of sample solutions in different reservoirs. For water based aqueous solution, the height difference of 10 mm corresponds to 1 mBar. But a few tens of μBars in large reservoirs can unpredictably transform several mBars for microfluidic channels because of their small dimensions.

And another limitation is the continuous decrease in pressure as the liquid flow through a microchannel to the dump, resulting in a decrease in flow rate with time [80]. This phenomenon will cause a drift in biosensor output signal as time goes by.

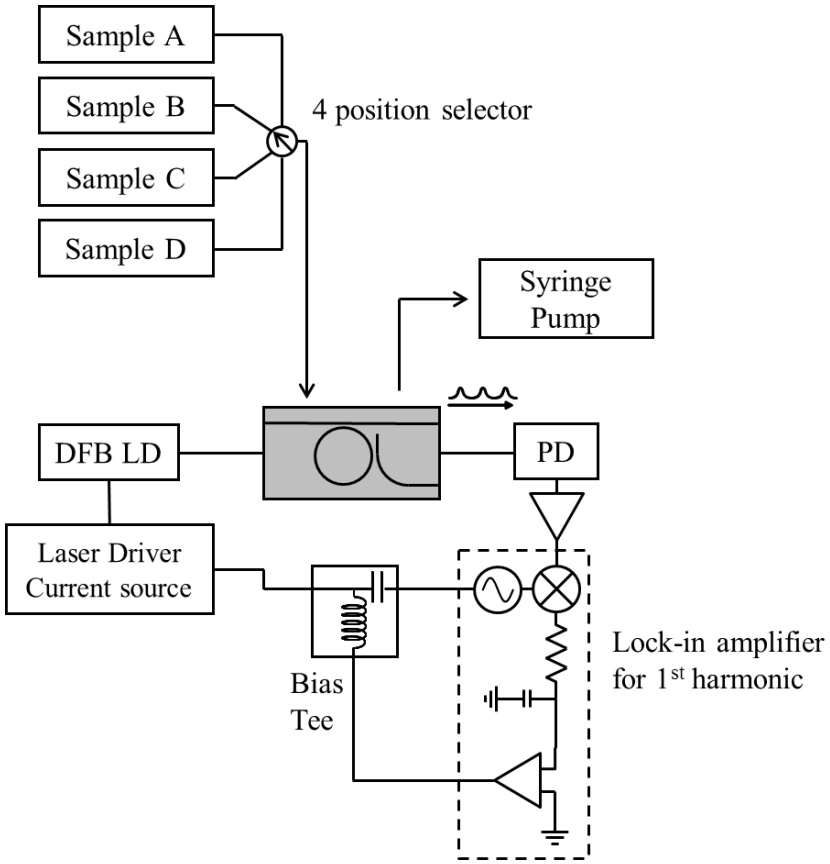

Figure 5.1. Schematic diagram of experimental setup for silicon ring biosensor with the hybrid flow control using the harmonic dithering technique

As a solution for problems found in both methods, both syringe pump and 4 position selector were used together. Based on the hydrostatic pressure injection system, a syringe pump for fluid withdrawal is added. The height difference between reservoirs and syringe pump was 1 m which is high enough to induce pressure in the microfluidic

channel. Not only is this advantageous from the perspective of low noise fluid delivery system, but also this configuration reduces cost of setup compare to a syringe pump system which requires the same number of syringe pumps as the number of sample solutions to be pumped.

5.2 Bulk Refractive Index Sensing

Using the feedback technique, we demonstrate the homogeneous sensing in aqueous solution for the calibration. We prepared weak NaCl solution that has slightly higher refractive index (Δn = 0.0019) than H_2O, and the Δn between two solutions was measured using an ellipsometer (VASE32, J.A. Woollam Co. [81]) at room temperature. During the measurement, no active temperature control loop was used for biosensor.

Initially H_2O was flowed continuously over chip surface until the baseline stabilized while optimizing the flow rate. After reaching a steady state, the feedback signal, which has become the proxy for the sensor readout in the harmonic dithering feedback technique, was measured using a low-noise voltmeter ($\sigma_V = 1.5\ \mu V$), and the result is shown in Figure 5.2. The rms deviation of the signal was measured to be $\sigma_V = 0.07 mV$.

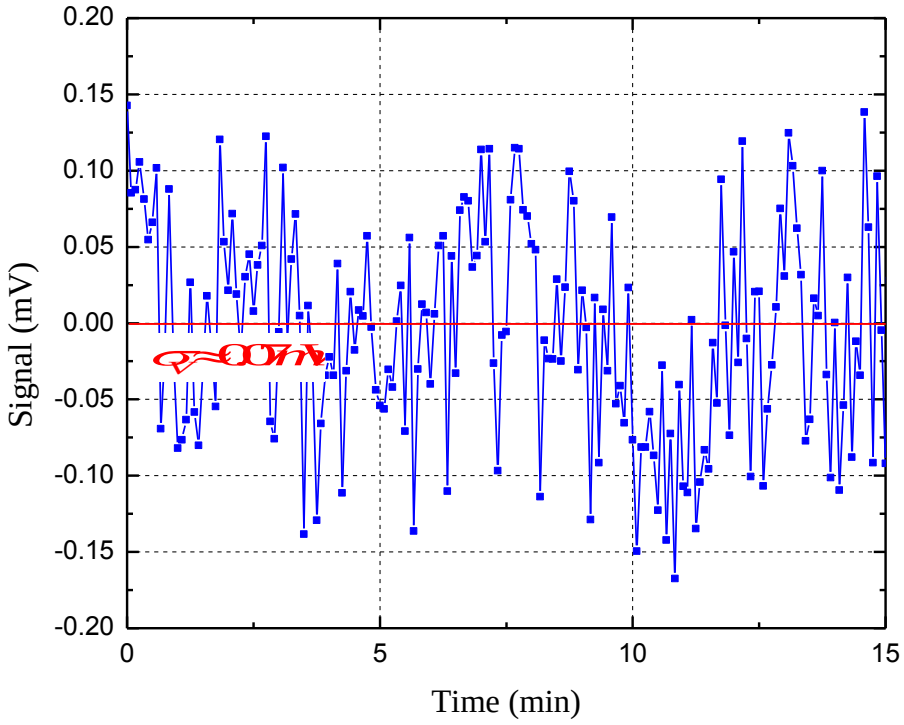

Figure 5.2. Temporal feedback voltage fluctuation with rms error of 0.07 mV.

A mechanical fluid selector was located after the two reservoirs for both H_2O and salt water and was computer-controlled, and the flow alternated every 10 minutes with a flow rate of 5.5 µl/min. The feedback signal coming from the lock-in was averaged every five seconds after the sampling using the voltmeter and the result of sensing for TM mode is plotted in Figure 5.3 (a). Note Δn=0.0019 in upper cladding gives the output signal of 1300 mV.

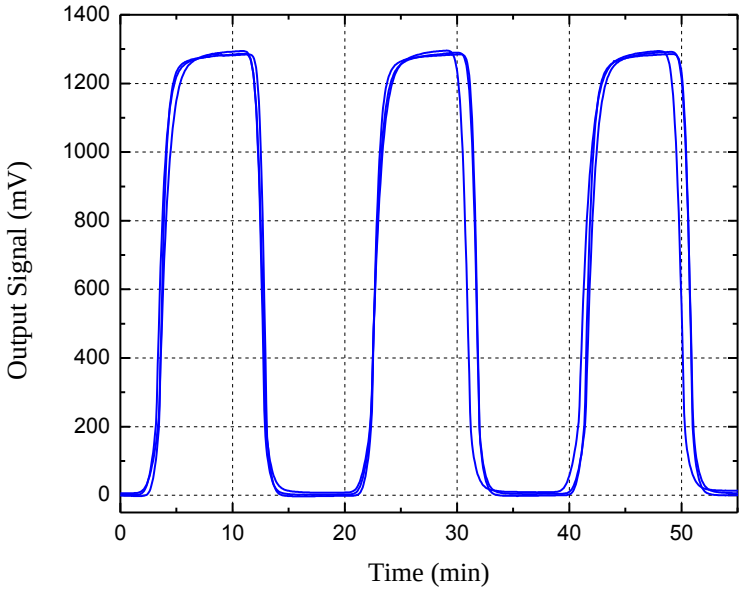

(a)

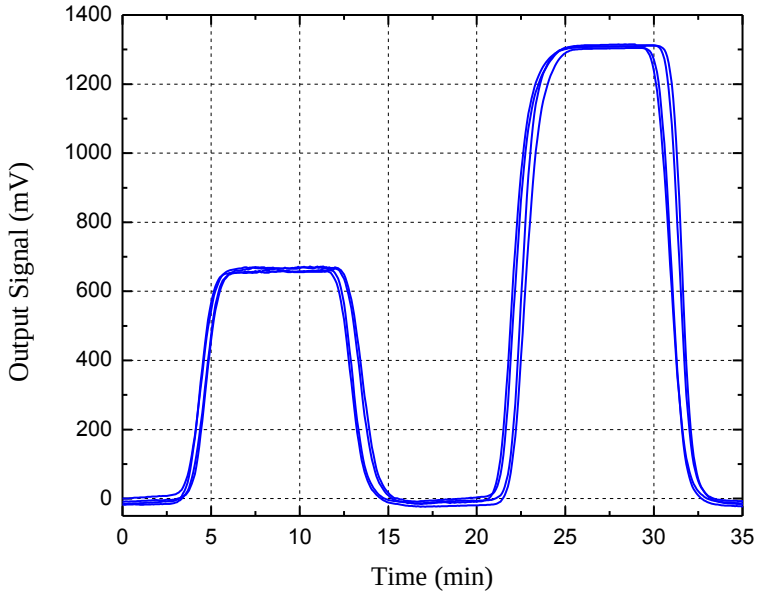

(b)

Figure 5.3. Homogeneous refractive index sensing results for the TM mode with (a) the NaCl solution with Δn=0.0019 and (b) Δn and 0.5 Δn

To investigate linear sensor response for bulk refractive index sensing, the NaCl solution was diluted by a factor of two, and we repeated the same experiment for many cycles as shown in Figure 5.3 (b). We can see the output signal of biosensor is 650 mV for the diluted NaCl concentration is halved.

In Figure 5.3, we can see that the output signal for index sensing drifts as the cycle repeats. We believe that this is cause by a hysteresis of active temperature control loops for DFB laser. Measurement results reveal a homogeneous refractive index response of 684 V/RIU with a sensitivity of 10^{-7} RIU. The calculation of detection limit is

$$\text{Detection Limit} = 0.0019\text{RIU} \div \frac{1300\text{mV}}{0.07\text{mV}} = 1.02 \times 10^{-7}\,\text{RIU}$$

5.3 Real-Time Monitoring of Binding Curves

5.3.1 Avidin-Biotin Interaction and Surface Immobilization

To illustrate the biomolecular recognition performance of label-free silicon biosensor we developed, we chose avidin-biotin system because it is well-studied system that has high binding affinity. The bond formation between biotin and avidin is very rapid, and once combined, is unaffected by extremes of pH, temperature, organic solvents and other denaturing agents [82]. These features of avidin-biotin system make it an ideal candidate for the demonstration of biosensor performance.

Streptavidin

Streptavidin is a 60,000 Dalton tetrameric protein that has four binding sites for biotin produced by Streptomyces avidinii and has a very high affinity to biotin (dissociation constant: $K_d = 10^{-14} \sim 10^{-15}$ M) [83]. Commercial streptavidin used in this thesis is recombinant form with a mass of 53,000 Daltons and has near-neutral isoelectric point (pI = 6.8 to 7.5) [82]. The charge neutrality of streptavidin significantly reduces the possibility of non-specific binding to other biological molecules due to the electrostatic forces. The reported thickness of a monolayer of streptavidin is in the range of 5-6 nm [84],[85].

Biotin

Biotin is a vitamin known as Vitamin H or Coenzyme R and is relatively small (244.3 Daltons) hydrophobic molecule. It can be conjugated to many proteins and other molecules without significantly altering their biological properties [87]. The highly specific interaction of biotin-binding proteins with biotin makes it a useful tool in biosensor development [18], [30], [34], [82], [86].

Biotin-labeled antibodies and other molecules are available commercially. For this study, biotinylated bovine serum albumin (b-BSA) or BSA-biotin was used in solid-phase assays as a coating on the silicon surface. The molar ratio of commercial BSA-biotin products is usually in the range of 1:8-12 (BSA:biotin) [82]. BSA is a large molecule (66,500 Daltons) and has a monolayer thickness of 3 nm [88].

Immobilization of BSA-Biotin on the Sensor Surface

A piranha cleaned chip was coated with 50 μg/ml BSA-biotin in pH 5.5 buffer for 6 hours, allowing attachment due to Van der Waals forces to immobilize BSA-biotin on a monolayer on top of the silicon oxide on silicon. This is because the effective charge of BSA depends on pH and is neutral at a near pH 5 [89].

5.3.2 Molecular Kinetics

To study the molecular adsorption, Langmuir adsorption models are employed [90]. The single isotherm describes the rate of surface reaction by

$$\frac{d\theta}{dt} = k_a(1-\theta)C - k_d\theta \tag{5.1}$$

where θ is the fraction of the available sites that are covered ($0 \le \theta \le 1$), k_a and k_d are the association and dissociation rate constants, and C is the concentration of streptavidin. The integration of Eq. (5.1) then yields the time dependent binding function given by [90]

$$\theta(t) = \frac{C}{C + (k_d / k_a)}[1 - e^{-(k_a C + k_d)t}] \tag{5.2}$$

However, analysis of Eq. (5.2) is not straightforward and it takes a very long time to reach to the saturation, especially when the target solution has a low concentration. When $C \gg k_d / k_a$, regardless of concentration C, the saturated signal $\theta(t = \infty)$ would be same. Instead of using signal saturation of Eq. (5.2), we use the initial slope of binding curve of Eq. (5.1) as a read out signal, which provides fast and linear response when

binding sites are initially unpopulated ($\theta = 0$). The initial binding curve is simply proportional to the concentration of target molecules:

$$\frac{d\theta}{dt} = k_a C \tag{5.3}$$

The schematic of functionalized sensor surface and biomolecular interaction is illustrated in Figure 5.4. Typical molar ratio is 1:10 between BSA and biotin [82], the shape of BSA-biotin molecule is simplified to help understanding.

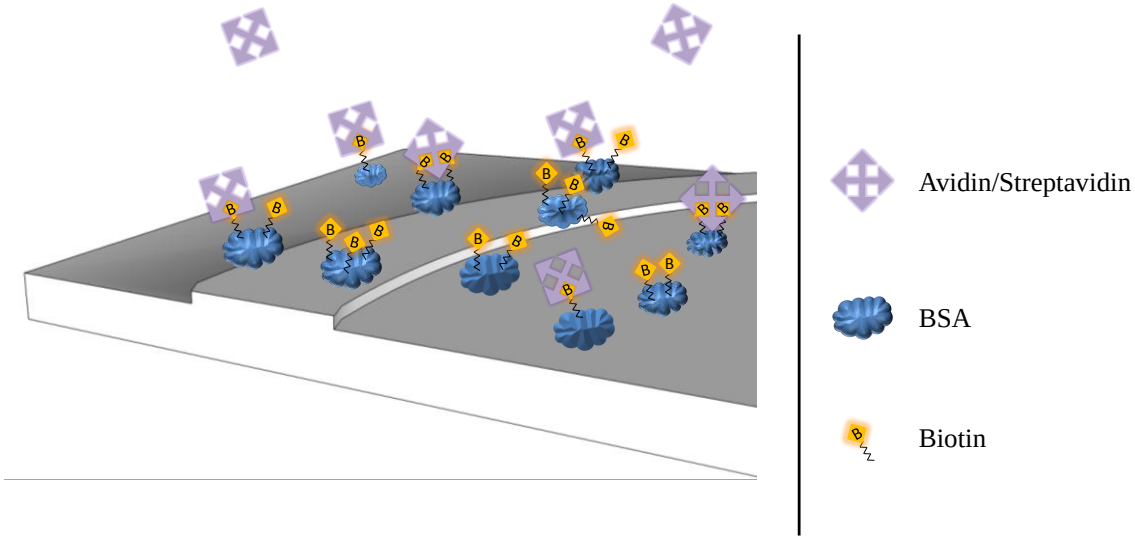

Figure 5.4. Schematic representation of the avidin/streptavidin-biotin interaction

5.3.3 Detection of Protein: Streptavidin

We first analyzed the real-time binding kinetics of 100 ng/ml streptavidin solution by looking at both association and dissociation curves plotted in Figure 5.5.

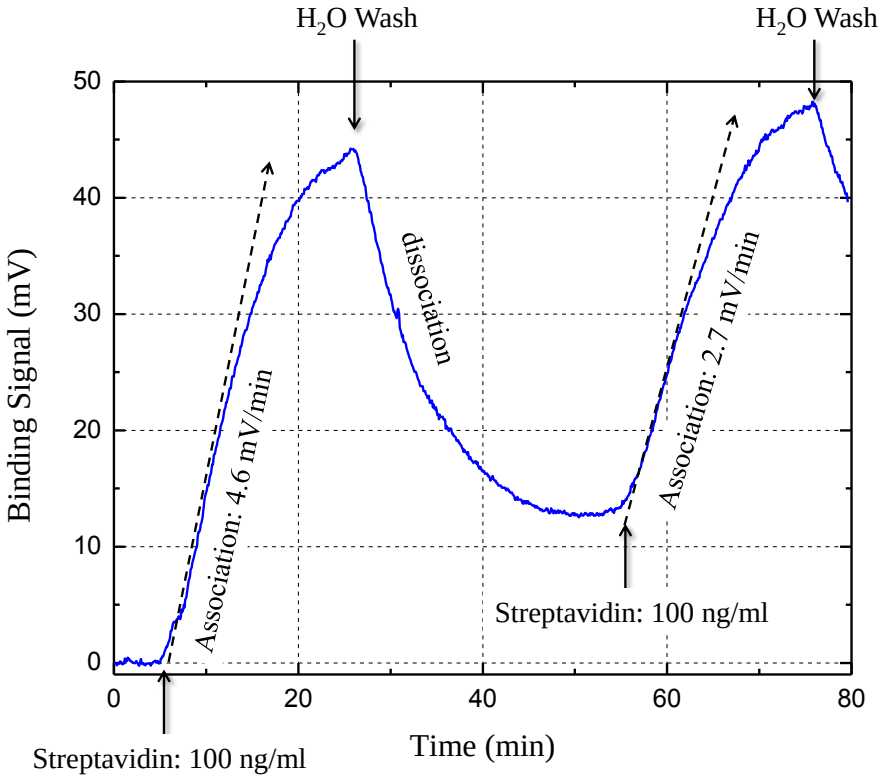

Figure 5.5. Real-time monitoring of the biotin-streptavidin binding curve by repeated the sample injection.

We can see that the feedback voltage increases with streptavidin molecules binding to the BSA-biotin sensing surface. When streptavidin was injected for the first time, the initial binding slope was measured to be 4.6 mV/min. At a time 20 minutes after the sample injection the flow of streptavidin solution was stopped, and H_2O was injected for 30 minutes to dissociate the biotin-streptavidin. The voltage difference between the initial baseline and the new baseline was 13 mV, which was due to the adsorption of streptavidin onto the surface via specific binding. The second injection of the same

streptavidin solution showed the lower binding slope of 2.7 mV/min because binding sites were partially populated ($\theta \neq 0$).

For statistical analysis, 6 different streptavidin concentrations were prepared: 10000, 1000, 100, 10, 1, and 0.1 ng/ml in H_2O corresponding to 200, 20, 2, 0.2, 0.02, and 0.002 nM respectively. These solutions were injected into the PDMS cell integrated with the biosensor. Figure 5.6 (a) shows binding curves for the first three concentrations of streptavidin, and the each concentration has the binding slope of 358, 96, and 5 mV/min respectively. The initial binding slope for 100 ng/ml is slightly different from the result shown in Figure 5.5, and this could be contributed by different BSA-biotin immobilization conditions on the sensor surface or drifts in the signal. A large concentration of streptavidin solution such as 10 μg/ml can cause a bulk refractive index sensing effect in surface sensing. A simple calculation based on the concentration ratio between water and streptavidin yields

$$\begin{aligned}\Delta n &= n_{streptavidin} - n_{H_2O} \\ &= \left(\frac{999.99 mg/ml}{1 g/ml} n_{H_2O} + \frac{0.01 mg/ml}{1 g/ml} n_{protein} \right) - n_{H_2O} \\ &= 1.8 \times 10^{-6} \text{RIU}\end{aligned} \tag{5.4}$$

For the consistency, $n_{protein}$ = 1.5 was assumed same as Section 3.1.2. The calculated refractive index difference between streptavidin solution and water corresponds to the 18 times of the detection limit for the bulk refractive index sensing in the ring biosensor shown in Section 5.2 and brings + 1.26 mV offset in the final binding signal. However,

for the measurement of streptavidin concentrations below 1 µg/ml, we do not have to consider the bulk refractive index sensing effect because it would be below the noise limit.

For low concentration solution of 200, 20, and 2 pM in Figure 5.6 (b), it seems binding curves are not linearly increasing because there are still small amounts of drift in signal, and we believe this is caused by thermal frequency stability of DFB laser when the feedback signal was changing due to the sensing. Obtained initial binding slopes were 2.4, 0.53, 0.16 mV/min respectively The measurement of the streptavidin concentration below 0.1 ng/ml (2 pM) was not conducted because of the poor SNR. The amount of sample solutions dispensed for each 10 minute measurement was typically 60 µl in volume.

The time constant setting used for measurements was 300 ms, except for the 10 µg/ml case where a time constant of 30 ms was used because the slow 300 ms closed loop cannot follow a very fast transition in binding curve.

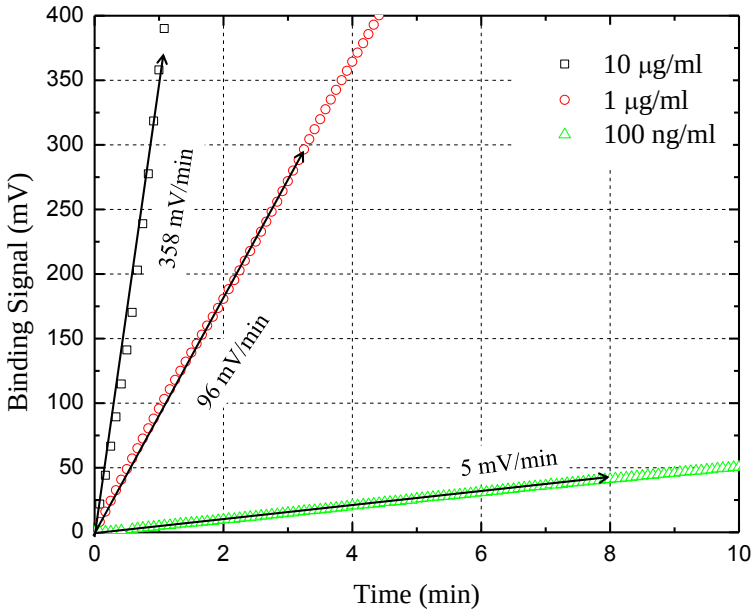

(a)

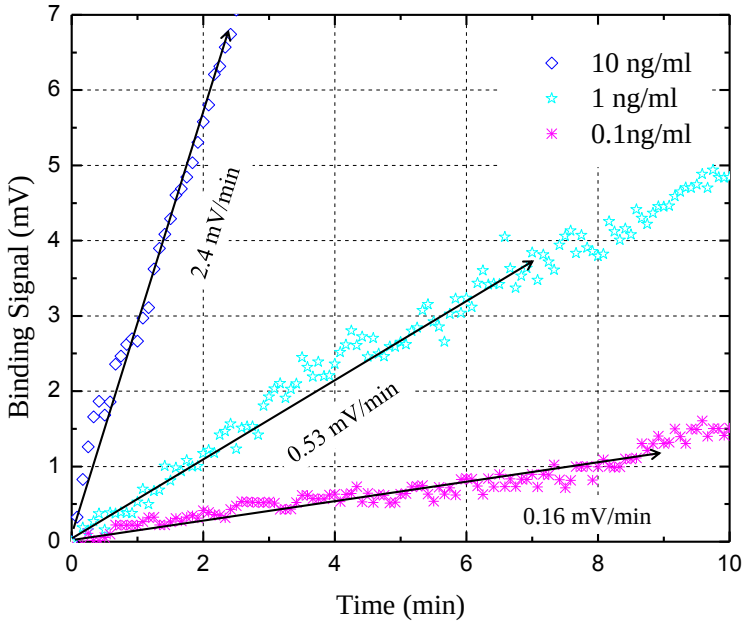

(b)

Figure 5.6. (a), (b) Monitored binding curves of streptavidin solution with different concentrations

Binding slopes taken from six different streptavidin solution measurements are plotted in Figure 5.7 with the red fitted line. The relationship found between initial binding slope and streptavidin concentration was $0.1\ {}^{\mathrm{mV}\cdot\mathrm{ml}}\!/_{\mathrm{ng}\cdot\mathrm{min}}$ or $5\ {}^{\mathrm{mV}}\!/_{\mathrm{nM}\cdot\mathrm{min}}$.

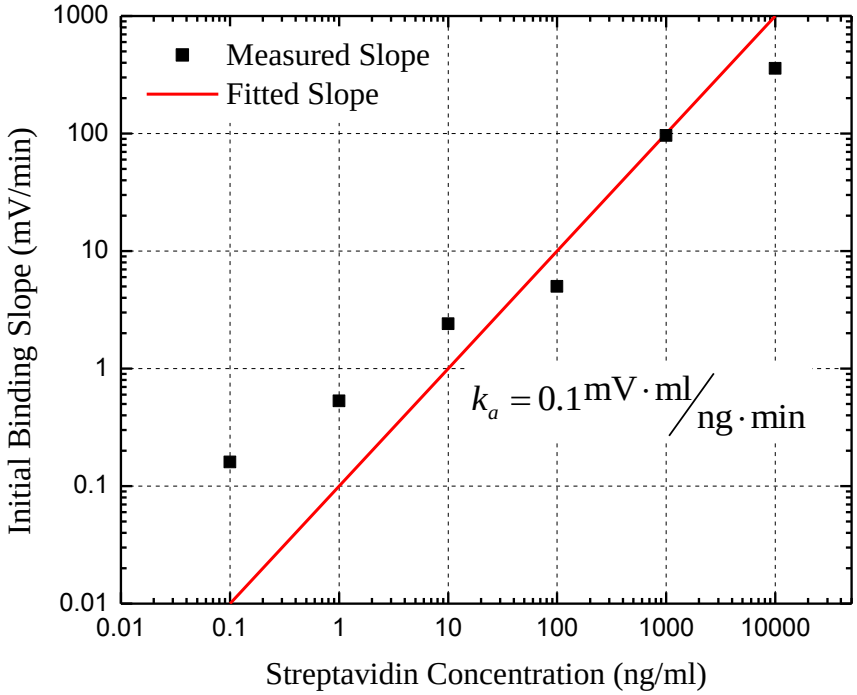

Figure 5.7. Measured and fitted initial binding slopes as a function of streptavidin concentration

To determine the detection limit for surface mass sensing, we can use the results from the bulk refractive index sensing. The refractive index response of 684 V/RIU from Section 5.2 shows that the 1300 mV feedback signal corresponds the refractive index change in cladding by Δn=0.0019, which is due to the waveguide modal index change of Δn_{eff} = 0.00085 based on the simple calculation from Eq. (2.7) by

$$\begin{aligned}\Delta n_{eff} &= \int_0^{\infty} \Delta n(y) f(y) dy \\ &= 0.0019 \int_0^{\infty} f(y) dy \\ &= 0.00085\end{aligned} \tag{5.5}$$

Using the effective index method introduced in Section 3.1.1, we can determine that this corresponds to ~ 1.3 nm surface adsorption on a 3-nm BSA-biotin layer as shown in Figure 5.8, which corresponds to 5×10^9 molecules/mm^2 or ~ 20 % of the maximum surface packing density of one 6-nm streptavidin monolayer [91], [92].

We can also obtain the thickness using the Eq. (2.7) again using the calculated weighting function shown in Figure 3.9 (b) by assuming that it is constant over the thin biolayer:

$$\begin{aligned}\int_0^d dy &= \frac{\Delta n_{eff}}{\Delta n \cdot f} \\ &= \frac{0.00085}{(1.5-1.32)\cdot 3.5\mu m^{-1}} \\ &= 1.3nm\end{aligned} \tag{5.6}$$

In this analysis the refractive index of each protein layer was taken to be n = 1.5 [17]. For the 0.07 mV noise level of our apparatus, this indicates a detection limit of ~ 270,000 streptavidin molecules/mm^2, surface mass density of ~ 24 fg/mm^2, or total mass of ~ 120 ag (~1,400 streptavidin molecules).

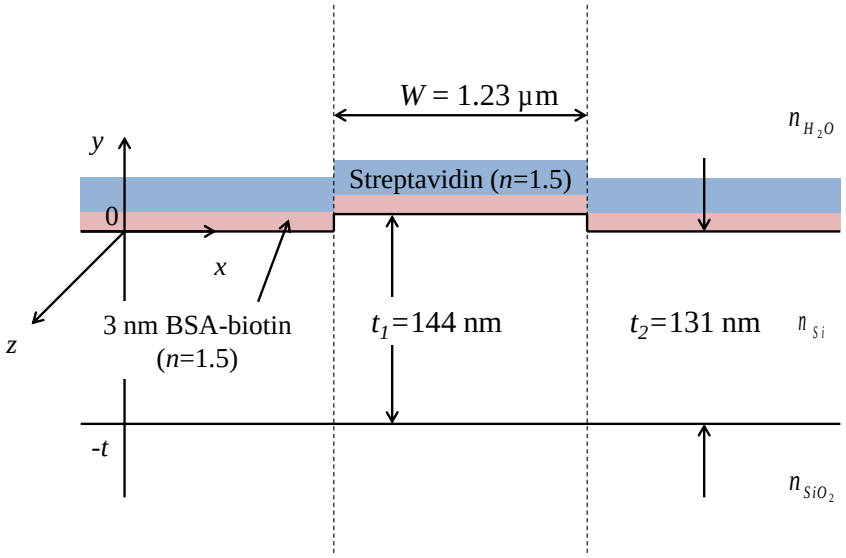

Figure 5.8. Surface adsorption model for the effective index method

Using the relationship between initial binding slope and streptavidin concentration, we can obtain the association rate constant k_a. Since 1300 mV feedback voltage corresponds to 20 % of the maximum surface packing density of one streptavidin monolayer

$$k_a = \frac{5\ \text{mV}}{\text{nM}\cdot\text{min}} \times \frac{20\%}{1300\text{mV}} = 1.28\times10^4 \text{M}^{-1}\ \text{S}^{-1} \tag{5.7}$$

and this shows a good match by within an order of magnitude with a reported number in [93] which is $5.13\times10^4\ \text{M}^{-1}\text{S}^{-1}$. General solution of Langmuir equation given by Eq. (5.2) was used to calculate dissociation rate constant k_d.

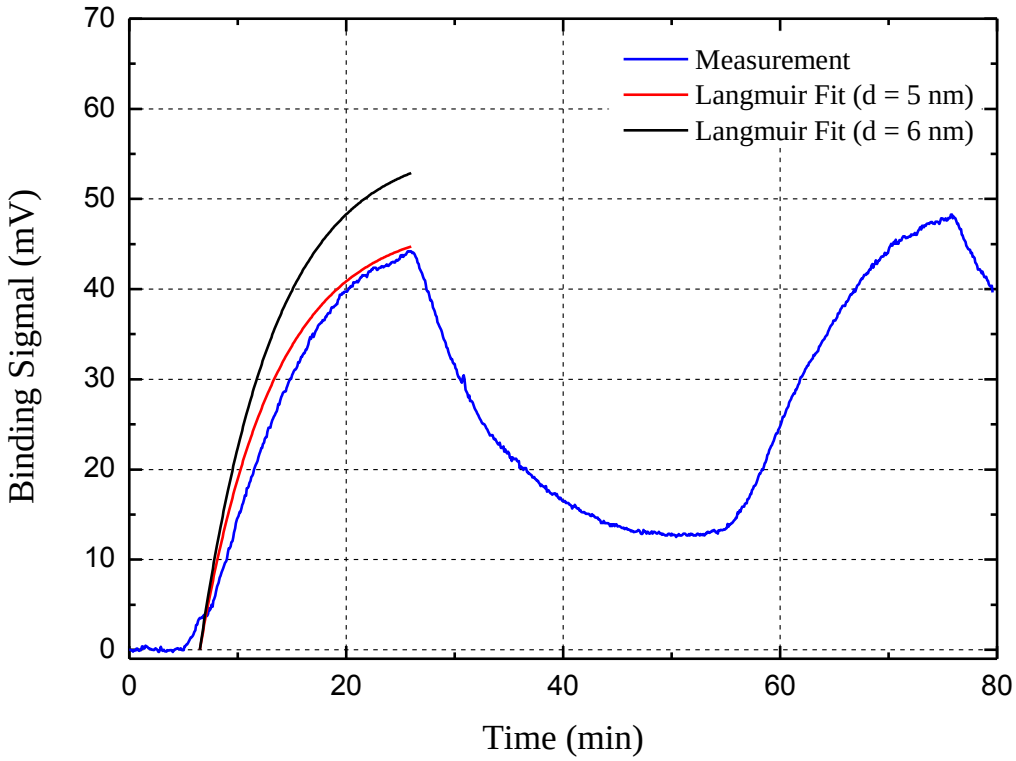

Figure 5.9. Fitted binding curves for two different thicknesses of the streptavidin monolayer

The fitted curves imply k_d =2.4×10^{-3} s^{-1}, and measured and fitted results are plotted together in Figure 5.9. When the streptavidin monolayer thickness was assumed to be 5nm, it generated better accuracy compare to the 6 nm monolayer. As described in Section 5.3.1, 5 nm streptavidin monolayer is still within a good range of reported values.

5.4 Discussion of the Detection Limit

A closed temperature control loop is very essential for the laser temperature control because any small changes in laser temperature can generate a larger signal deviation

than a biosensor signal. For example, DFB lasers typically show 1 GHz optical frequency shift for 0.1 ℃ temperature change, and in contrast TM-mode athermal waveguide shows only 3 MHz shift. For the precise TEC control of DFB LD, a 32 Watt temperature control module (ILX Lightwave, MT [93]) was used. The short term stability of the module was ± 0.004 ℃, which corresponds to laser frequency stability of ± 40 MHz due to a temperature sensitivity of -10 GHz/K [95], and according to Eq. (2.1), this would limit the detection limit to $\Delta n_{eff} \approx 5\times10^{-7}$ RIU. The actual temperature stability was better than the manufacturer's specification, but using better laser temperature controllers would be recommended to further improve the temperature stability.

To illustrate the sensitivity of silicon photonic biosensor that we have developed, a comparison of the sensing performance of optical label-free technologies that have demonstrated most outstanding performances is shown in Table 5.1 below.

*. Based on the extrapolation to an OSA with a better resolution.

Technology		Detection limit	Reference
Surface Plasmon		10^{-7} RIU	[96]
		100 pM	Biacore 4000 [25]
		100 fg/mm^2	
Fiber Grating		5×10^{-6} RIU	[97]
		5 pg/mm^2	
Interferometer*		10^{-7} RIU	[98]
		10 pM (DNA)	
Photonic Crystal		7×10^{-8} RIU	[85]
		24 fg/mm^2	
Si Ring Resonator	D = 30 μm	7.6×10^{-7} RIU	[18]
		60 fM	
	D = 50 μm	300 fg/mm^2	[19]
		20 pM	
My Si Ring Resonator (D = 800 μm)		**1×10^{-7} RIU**	**This work**
		2 pM	
		24 fg/mm^2	

Table 5.1. Detection limits of many practical label-free optical biosensors.

The work that I have shown in this thesis has the relatively low sensitivity for surface sensing compare to the work in [18]. In terms of molar sensitivity, one limiting factor in the designs discussed here remains as the size of ring resonator. Ways to increase the sensitivity based on the shallow ridge waveguide will be discussed in next chapter.

Our shallow ridge waveguides based on CMOS technology have a great potential in terms of integrated optics, for example integration with a Ge photodetector by wafer bonding technique [99] with a lock-in amplifier is shown in Figure 5.10.

An additional advantage of the techniques presented here relates to ease of use. When an end user operates this biosensor, there is no requirement to make any adjustment of settings to find out the signal before use. Since the feedback gain is large enough, and the free spectral range of the ring resonator is suitably matched to the current tuning dynamic range, the lock-in automatically locates and latches onto the coupled signal from the ring resonator. In our laboratory experimental environment, the mounting the PDMS attached Si chip and tube connecting are only tasks required of the end user.

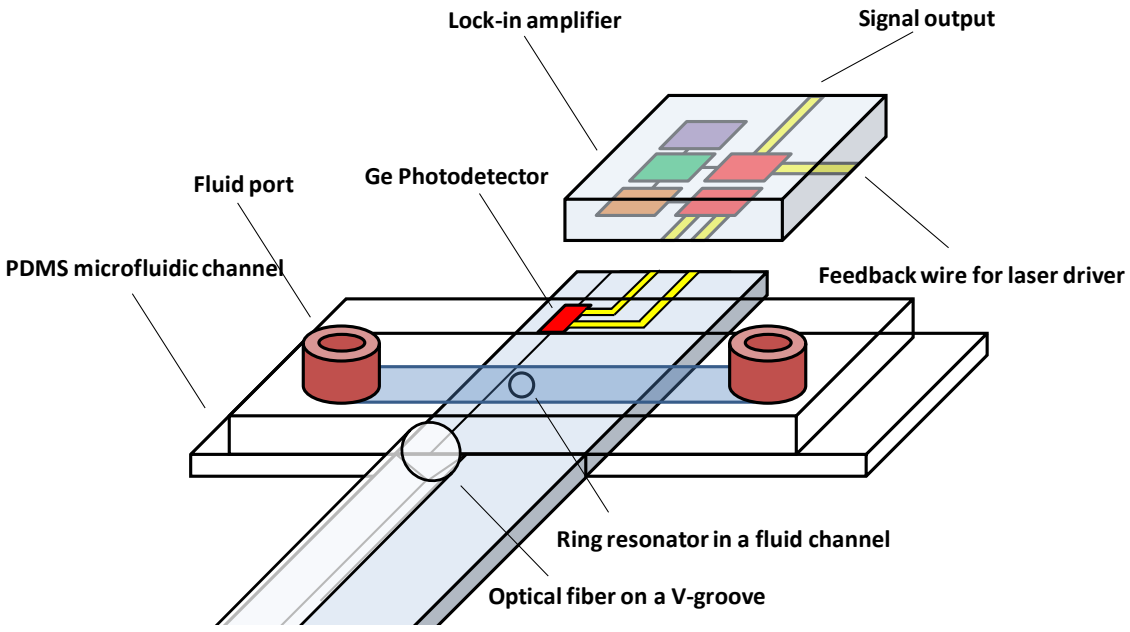

Figure 5.10. Concept of integrated biosensor on CMOS technologies

Chapter 6

Conclusions and Future Works

Silicon photonic biosensors based on a CMOS technology improve the integration density for both optical and electronic functions. Deep submicron ASIC design provides a pathway for low power consumption and cost-effective manufacturability. Also a large index contrast of SOI wafer provides the enhanced surface sensitivity for a TM-mode optical biosensor.

6.1 Summary

Chapter 2 described silicon biosensor modeling and fabrication based on the shallow ridge waveguide geometry. The fabricated 400 μm ring resonator had $Q = 47{,}000$ for TM mode. This was achieved using a magic width design which removes the slab mode leakage that would normally occur due to the mode match between TE and TM modes.

Chapter 3 theoretically and experimentally demonstrated an athermal silicon photonic biosensor for aqueous sensing based on the shallow ridge waveguide. The large optical mode confinement in an aqueous cladding for TM-mode operation provides a cancellation of thermal effects in thin silicon waveguides by using the opposite thermo-

optic coefficients between Si and H_2O. For the experimental demonstration of athermal performance, we scanned the temperature of the biosensor and obtained the temperature independence near 300 K using slightly different thicknesses of waveguide.

In Chapter 4, we developed a novel low-noise measurement platform, the harmonic dithering technique, for a signal readout of biosensor. Conventional measurement techniques for silicon biosensor based on tunable laser instrumentation are bulky, noisy, and expensive and must utilize accompanying reference devices to measure relative wavelength shifts. In contrast, the harmonic dithering only uses a DFB LD and a DSP lock-in amplifier. This technique modulates the laser frequency across Lorentzian lineshape of ring resonator signal at a high frequency (20 kHz in this work) which minimizes the impact of *1/f* noise. Successive low-pass filtering (12 dB/oct in this work) also minimizes the broadband noise. Another benefit of the harmonic dithering technique is the fact that the DSP lock-in amplifier can ultimately be realized on a small silicon chip with biosensors via ASIC technologies.

Chapter 5 explored both bulk refractive and surface sensing. The detection limit for homogeneous bulk refractive index sensing was 1×10^{-7} RIU using a weak NaCl solution. Streptavidin-biotin interaction was used to demonstrate the surface sensing, and 6 different concentration of streptavidin solution were injected into the PDMS microfluidic channel integrated on the biosensor. We detected the concentration of streptavidin solution down to 2 pM using the initial binding curve. From the calculation with the rms

noise of 0.07 mV, we determine detection limits for surface mass density of 24 fg/mm^2 and total adsorbed mass of 120 ag.

6.2 Conclusions

Through calculations, analysis, and measurements, we demonstrated the high-sensitivity silicon photonic microfluidic biosensor which

- is independent on the ambient temperature fluctuation.
- is realized based on the harmonic dithering feedback technique that minimizes *1/f* and broadband noises.
- can detect bulk refractive index change down to 1×10^{-7} RIU
- can detect surface mass density down to 24 fg/mm^2 and total adsorbed mass of 120 ag.

6.3 Future Work

High-sensitivity biosensors were developed, but we can expect further improvement in performance. Some promising areas of research are:

Use of Distributed Bragg Reflector (DBR) Laser

Strong temperature sensitivity of DFB LD (-10GHz/℃) is one of limiting factors in high-sensitivity biosensing. Additionally, a DFB laser has a small tuning range. For example, when the laser bias current is 60 mA, we might have only 90 GHz tuning range when the laser maximum current rating is 150 mA based on the laser's thermal characteristics. This makes hard to measure a large concentration solution, and it also limits the free

spectral range of the resonator if we must guarantee the ability to lock onto a resonance.

Microfluidic Channel Design

Simple rectangular PDMS microfluidic channels were used without optimizing the structure. The dimension of channels used in experiments, 1 mm in width × 50 μm in height, is in the regime of Laminar flow, which means there is no turbulence in the channel [100]. However the fluid induced noise and drift problems could possibly be improved through fluid dynamic analysis of microchannel to develop a deeper understanding of the pressure driven flow with a syringe pump.

Improvement in a CMOS Process

The 400 μm ring resonator was used to evaluate the sensor performance, and its large size is limiting the detection limit for the surface sensing. Simply using 200 μm ring will double the sensitivity, and the fabrication of smaller device at a low loss is possible. Our theoretical calculation and experimental experience show waveguides with ~ 4 dB/cm loss is feasible with 200 μm radius for 144 nm waveguide thickness.

We can also double the cross sectional sensitivity of waveguide by undercutting a BOX layer through etching the inner region of Si ring resonator. Care would be required in following this path because it will likely lead to additional losses and fabrication challenges. Another benefit of undercutting the BOX is the fact that we can use thicker Si of 170 nm to cancel out thermo-optic effect as shown in Figure 6.1. Thicker silicon

thickness improves sensitivity and also provides a smaller bending loss for TM mode, thereby further decreasing the device size.

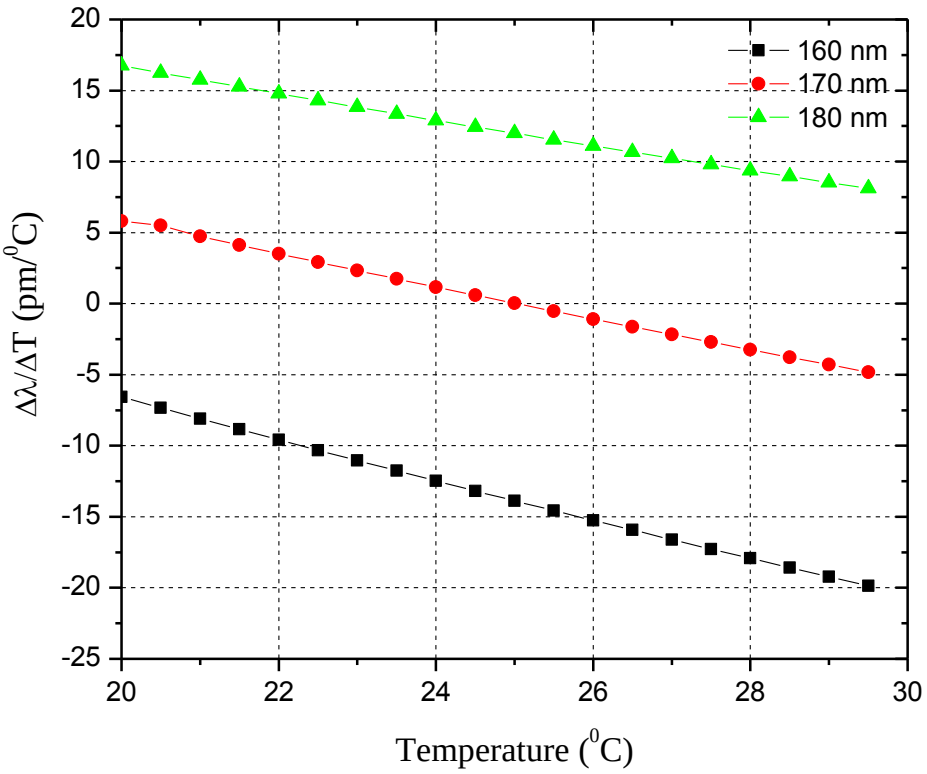

Figure 6.1. Derivative of wavelength to the temperature for the undercut waveguide structure

Appendix A

Refractive Index Models

A.1 Refractive index of Si

The Sellmeier equation is used to describe temperature and wavelength dependent properties of Si. The general form of Sellmeier equation is [56]

$$n^2(\lambda,T) = 1 + \sum_{i=1}^{l} \frac{S_i(T)\lambda^2}{\lambda^2 - \lambda_i^2(T)} \tag{A.1}$$

where S_i are the strengths of the resonance features in the material at wavelengths λ_i. Typically third order forms are good approximations to relate the wavelength dependent phenomena. However, for temperature dependence, fourth order models describe the material property properly, and the Sellmeier equation consequently becomes

$$n^2(\lambda,T) = 1 + \sum_{i=1}^{3} \frac{S_i(T)\lambda^2}{\lambda^2 - \lambda_i^2(T)} \tag{A.2}$$

where

$$S_i(T) = \sum_{j=0}^{4} S_{ij} T^j$$
$$\lambda_i(T) = \sum_{j=0}^{4} \lambda_{ij} T^j \quad \text{(A.3)}$$

Coefficients for the temperature dependent Sellmeier equation for Si for the range of 20 K < T < 300 K and 1.1 μm < λ < 5.6 μm are in Table A.1 [56].

j	S_{1j}	S_{2j}	S_{3j}	λ_{1j}	λ_{2j}	λ_{3j}
0	1.04907E+01	-1.34661E+03	4.42827E+07	2.99713E-01	-3.51710E+03	1.71400E+06
1	-2.08020E-04	2.91664E+01	-1.76213E+06	-1.14234E-05	4.23892E+01	-1.44984E+05
2	4.21694E-06	-2.78724E-01	-7.61575E+04	1.67134E-07	-3.57957E-01	-6.90744E+08
3	-5.82298E-09	1.05939E-03	6.78414E+02	-2.51049E-10	1.17504E-03	-3.93699E+01
4	3.44688E-12	-1.35089E-06	1.03243E+02	2.32484E-14	-1.13212E-06	2.35770E+01

Table A.1. Coefficients for the temperature-dependent Sellmeier fit of the refractive index of Si based on measurement data.

A.2 Refractive index of H_2O

We have used following representation of the wavelength, temperature, and density dependence of the Lorentz-Lorenz function of light water [57]

$$\frac{n^2-1}{n^2+1}\frac{1}{\rho^*} = a_0 + a_1\rho^* + a_2 T^* + a_3\lambda^{*2}T^* + a_4/\lambda^{*2} + \frac{a_5}{\lambda^{*2}-\lambda_{UV}^{*2}} + \frac{a_6}{\lambda^{*2}-\lambda_{IR}^{*2}} + a_7\rho^{*2} \quad \text{(A.4)}$$

where

$$\begin{aligned} \rho^* &= \rho / \rho_0 & \rho_0 &= 1000 \text{ kg/m}^3 \\ \lambda^* &= \lambda / \lambda_0 & \lambda_0 &= 0.589 \text{ μm} \\ T^* &= T / T_0 & T_0 &= 273.15 \text{ K} \end{aligned} \qquad \text{(A.5)}$$

ρ is the density, λ the wavelength and T the absolute temperature. The values of the coefficients a_0 to a_7, and the effective infrared and ultraviolet resonances λ^*_{IR} and λ^*_{UV} respectively are listed in Table A.2. The ranges of three independent variables are

temperature	$0 < t < 225$ °C
density	$0 < \rho < 1060$ kg/m^3
wavelength	$0.2 < \lambda < 2.5$ μm

$a_0 = +0.243905091$	$\lambda^*_{UV} = 0.2292020$
$a_1 = +0.53518094 \times 10^{-3}$	$\lambda^*_{IR} = 5.432937$
$a_2 = -3.64358110 \times 10^{-3}$	
$a_3 = +2.65666426 \times 10^{-4}$	
$a_4 = +1.59189325 \times 10^{-3}$	
$a_5 = +2.45733798 \times 10^{-3}$	
$a_6 = +0.897478251$	
$a_7 = -1.63066183 \times 10^{-2}$	

Table A.2. Coefficients for Eq. (A.4)

A.3 Refractive index of SiO_2

Sellmeier equation is adopted again to represent the refractive index of SiO_2. The thermo-optic effect of SiO_2 is not considered because it is ten times smaller than that of

Si and , H_2O and it is nearly constant ($+11.3\times10^{-6}$/℃) over the wavelength near to mid infrared range.

For Sellmeier equation without temperature effect [63]

$$n^2(\lambda) = 1 + \sum_{i=1}^{3} \frac{S_i \lambda^2}{\lambda^2 - \lambda_i^2} \tag{A.6}$$

coefficients are in Table A.3. The equation is valid for the range of 0.2 μm < λ < 4.5 μm.

i	S_i	λ_i
1	0.6961663	0.0684043
2	0.4079426	0.1162414
3	0.8974794	9.896161

Table A.3 Coefficients for Eq. (A.6)

Appendix B

Intrinsic Electronic Noises

Sensors, detectors, and transducers translate the characteristics of the physical parameters into electrical signals [36]. We process and measure these signals and interpret them to be the reactions taking place such as molecular interactions or telecommunication signals [101]. Since any noises appear on the signal degrades the biosensor performance, we must interface the biosensor with optoelectronic circuit that contributes the minimum of additional noises. So it is important to precisely measure the system noise, understand the contribution of each component, and manage the noise. In our sensor configurations, some noise originates from the electronics and the fluid delivery system, and temperature fluctuation of ambient can also contribute to noise in the system.

This appendix defines the fundamental types of noise present in an optical biosensor system and discusses methods of engineering these sources for the purpose realization of high-sensitivity biosensor. In addition to concepts, spectral analysis of noises is shown.

B.1 Electronic Noises

Noise is a totally random signal which consists of frequency components that is random in amplitude [101]. While we cannot perfectly eliminate the noise, its effect can be

minimized by careful system design. Usually white noise has a Gaussian or normal distribution of instantaneous amplitudes with time [102]. The Gaussian distribution curve is illustrated in Figure B.1 along with a simulated electrical noise.

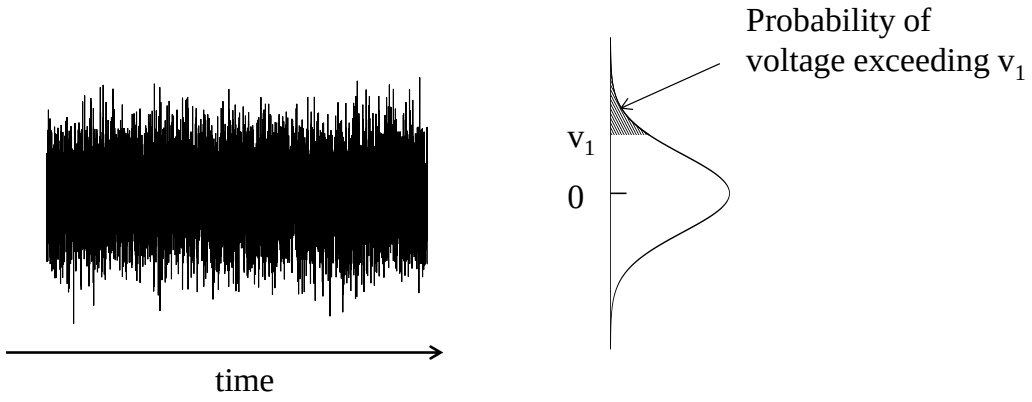

Figure B.1. Gaussian noise waveform and its distribution function

The Gaussian distribution predicts the probability of the measured noise signal having a specific value in time [101]. If one could collect large data points and record the number of occurrences when the noise voltage level is equal to or greater than a particular level, the Gaussian distribution would result [101]

$$f(x) = \frac{1}{\sigma\sqrt{2\pi}} e^{-\frac{(x-\mu)^2}{2\sigma^2}} \tag{B.1}$$

where μ is the mean or average value and σ is the standard deviation or root mean square (rms) value of the variable x. The function $f(x)$ is referred to as the probability density function. The area under the Gaussian curve represents the probability that a particular event will occur. Since probability can only take on values from zero to one, the total area

must equal unity. If we consider a value such as V_1, the probability of exceeding that level at any instant in time is shown by the cross-hatched area in Figure B.1.

The rms voltage is a statistical measure of the magnitude for time varying voltage *v(t)*

$$v_{rms} = \sqrt{\frac{1}{T}\int_0^T v^2(t)dt} \tag{B.2}$$

where *T* is the period of the voltage.

In this section, we will examine and measure each electronic and photonic noise source in our system. All of these noise sources are incoherent, and thus the total noise is the square root of the sum of the squares of all the incoherent noise sources.

B.2 Shot Noise – a beat noise approach

Photogenerated carriers in photodetector show random fluctuations, and this causes noise on output current. It is often useful to think that the noise originates from a photodetector when photons are being absorbed, but this is not the only way to derive shot noise contributions. The random fluctuation can also be understood to stem from the quantum fluctuations of the optical field itself [104].

The minimum additive optical noise is usually referred, in quantum electrodynamics, as the zero-point field fluctuations or the vacuum fluctuations [105]. Here the derivation of shot noise from the interpretation of optical noise beating between the optical field and the zero-point vacuum fluctuations follows the works shown in [105], [106].

Average laser output power of classical complex field amplitude A is $P_L = AA^*$. In quantum mechanics, however, energy of zero-point field fluctuation or vacuum fluctuation of oscillator is

$$E = \frac{h\nu}{2} \tag{B.3}$$

where h is plank's constant. By considering the optical noise with bandwidth B_o, noise amplitude b is defined

$$b = \sqrt{\frac{h\nu}{2} B_o} = \sqrt{S_b B_o} \tag{B.4}$$

where S_b is optical noise power spectral density, and $S_b = h\nu/2$. For example, for 1550 nm corresponding to $\nu = 193.4$ THz, the zero-point field fluctuation S_b is 6.4×10^{-20} W/Hz.

Due to Heisenberg's uncertainty, the smallest field fluctuation b on signal amplitude A can be expressed

$$P = (A+b)(A+b)^* = AA^* + 2\,\mathrm{Re}\{Ab^*\} + bb^* = P_L + \Delta P \tag{B.5}$$

where bb^* is not detectable by photodetector.

The mean squared optical power fluctuation is

$$\left\langle (\Delta P)^2 \right\rangle = 4A^2b^2 = 4P_L S_b B_o = 2P_L h\nu B_o \tag{B.6}$$

considering only the in-phase noise component yields average power of

$$\left\langle (\Delta P)^2 \right\rangle_{in-phase} = P_L h\nu B_o \tag{B.7}$$

The bandwidth of single-sided electrical spectrum is half of optical bandwidth, $B_o = 2B_e$, and thus we have

$$\left\langle (\Delta P)^2 \right\rangle_{in-phase} = 2P_L h\nu B_e \tag{B.8}$$

We can rewrite in terms of electrical current when a detector has responsivity of $R = e\eta / h\nu$

$$\left\langle (\Delta i)^2 \right\rangle = R\left\langle (\Delta P)^2 \right\rangle_{in-phase} = 2e\eta B i_s \tag{B.9}$$

where η is quantum efficiency assumed to be 1 for simplicity and e from bandwidth is dropped for convenience since we will discuss only the electrical bandwidth. e is the electron charge (1.6×10^{-19} Coulomb) and i_s is the signal current. This noise is called shot noise, and has the rms expression:

$$\left\langle i_{shot} \right\rangle = \sqrt{2eBi_s} \tag{B.10}$$

If can write photo current from a photodetector which has the responsivity of R, and lose some power by the absorption α

$$i_s = RP_L e^{-\alpha} \tag{B.11}$$

the signal-to-noise ratio (SNR) of shot-noise limited case at a load impedance of R_L is

$$\frac{v_s^2}{\left\langle v_{shot}^2 \right\rangle} = \frac{i_s^2 R_L^2}{\left\langle i_{shot}^2 \right\rangle R_L^2} = \frac{R_L^2 (RP_L)^2 e^{-2\alpha}}{R_L^2 (2ReP_L) B e^{-\alpha}} = \frac{RP_L e^{-\alpha}}{2eB} \tag{B.12}$$

It is obvious that SNR strongly depends on the incoming optical power into the photodetector. For example, the optical power of 1 mW has the shot noise limit of -155 dBc/Hz, and when we have 10 mW, the shot noise reduces to -165 dBc/Hz. Shot noise shows the slope of 10 dB/dec.

B.3 Thermal Noise

This section follows materials from unpublished notes used in ECE 450, Optoelectronics Physics and Lightwave Technology II, taught by Prof. Thomas L. Koch [107].

The load impedance R_L at the termination of a photodetector introduces another noise because of the thermal motion of electrons even at equilibrium. In thermal equilibrium state, the photon energy from Bose–Einstein statistics is

$$E = \frac{h\nu}{e^{h\nu/kT} - 1} \underset{kT >> h\nu}{\approx} kT \tag{B.13}$$

where k_B is Boltzmann's constant and corresponding power is

$$P = k_B TB \tag{B.14}$$

To help understanding of the thermal noise, a simple perfectly impedance matched circuit model is shown in Figure 6.3. Left resistor can be regarded as a noise generator, and half of noise power will be transmitted to right resistor without any reflection. The voltage noise generated by current noise source in circuit is $v_n = i_n R_L / 2$. However the amount of noise transmitted to right resistor is half of this, and noise power is

$$P_n = \frac{v_n^2}{4R_L} \tag{B.15}$$

and equate to Eq. (B.14), we get the voltage noise of

$$\langle v_n \rangle = \sqrt{4k_B T R_L B} \tag{B.16}$$

Thermal noise voltages were measured in Figure 6.2 for three different resistances which are 10 MΩ, 100 kΩ, and 10 kΩ with corresponding noise voltages of 411, 41, and 13 $\mathrm{nV}/\sqrt{\mathrm{Hz}}$ respectively. Measured values provide the exact match to calculated values, except that we can see a new *1/f* noise component that increases with the large resistance.

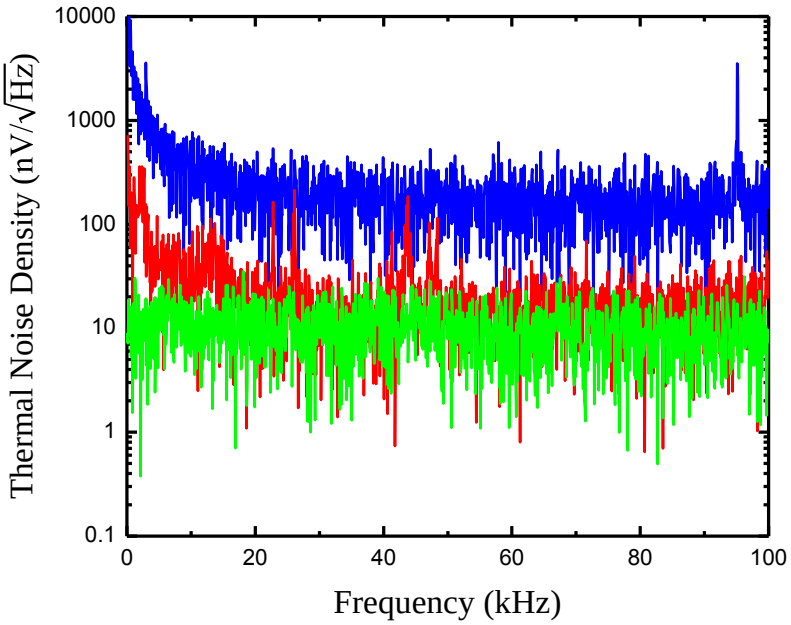

Figure 6.2. Measurement of thermal noise spectra for 10 MΩ (blue), 100 kΩ (red), and 10 kΩ (green).

The noise power is generated at the resistor is

$$P = \frac{\langle v_n^2 \rangle}{R_L} = 4k_B TB \tag{B.17}$$

and regardless of what values of resistor is used, the noise power at room temperature for a 1 Hz bandwidth is $P_{dBm} = -174\text{dBm}$.

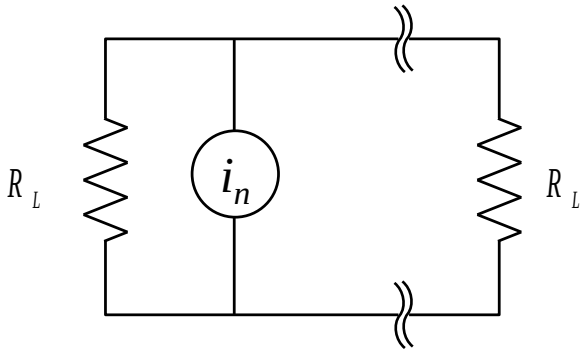

Figure 6.3. Schematic circuit of current noise generator in thermal equilibrium

We can express the thermal noise in current form by

$$\langle i_{therm} \rangle = \sqrt{\frac{4k_B T}{R_L} B} \tag{B.18}$$

The corresponding SNR yields

$$\frac{v_s^2}{\langle v_{them}^2 \rangle} = \frac{i_s^2 R_L^2}{\langle i_{them}^2 \rangle R_L^2} = \frac{(RP_L)^2 e^{-2\alpha} R_L}{4k_B TB} \tag{B.19}$$

We can see that the SNR increases proportionally to R_L. However, we cannot increase R_L infinitely because it limits the bandwidth of photodetector, and the bandwidth of photodetector $\Delta\nu_{3dB}$ can be expressed as,

$$\Delta \nu_{3dB} = \frac{1}{2\pi R_L C} \tag{B.20}$$

where C is the junction capacitance of the photodiode usually ~ 1 pF.

Just as in the case of the shot-noise limited SNR, increasing the optical power increase the SNR of thermal-noise.

B.4 *1/f* Noise

The origin of *1/f* noise is still very complex and differs for different systems [102], [103], but it is commonly related to the defects in semiconductor crystalline structure [102] or the imperfect contact between two conducting materials [108]. The mean *1/f* noise voltage for a bandwidth *B* is

$$\left\langle v_{1/f} \right\rangle = R_L \sqrt{\frac{K_f i_s^m B}{f^n}} \tag{B.21}$$

where K_f is the *1/f* noise coefficient, i_s is the DC signal current, $n \cong 1$, and m is the *1/f* noise exponent. *1/f* noise is also called flicker noise or pink noise.

In modeling of *1/f* noise, typically the value $m=2$ is used [108], and this leads to a relatively simple form, which is Hooge's empirical equation [109]

$$\left\langle v_{1/f} \right\rangle = R_L i_s \sqrt{\frac{K_f B}{f}} \tag{B.22}$$

The dimensionless constant K_f depends on material used for resistors or semiconductors. And especially for CMOS transistors, different geometries such as oxide capacitance,

channel length and width or fabrication processes can also impact on the noise characteristics with a given material [110], [111]. Table B.4 shows the various K_f for different types of materials.

Material type	K_f	Reference
Carbon composite	$10^{-13} – 10^{-15}$	[113]
Metal films Carbon fibers	$6 \times 10^{-17} – 10^{-19}$	[113], [114]
a-Si deposited by RF sputtering	1.2×10^{-11}	[115]
single-walled carbon nanotubes	10^{-9}	[113]

Table B.4. *1/f* noise coefficients for different materials

For resistors, typically carbon composite has the worst *1/f* noise and metal film is the best, and carbon film resistors lying between the two [108].

1/f noise increases as the frequency approaches to 0 Hz, and cause a DC drift. For example, when we try to measure 1 A current at 1 Hz frequency across the 1 kΩ metal film resistor ($K_f = 10^{-17}$), *1/f* noise is 3.2 μV_{rms} for 1 Hz bandwidth. However if we repeat the same measurement at 10 kHz frequency, *1/f* noise reduces to 32 nV_{rms}. The impact of *1/f* noises are shown in Figure 6.2, and note that 10 MΩ resistor has significantly large noise compare to 10 kΩ at a low frequency regime. *1/f* noise is very critical at low frequency as shown in Figure 6.2 and this is why using higher frequency is preferred. Another characteristic is that the noise voltage is proportional to a DC current in

electronic devices. To solve this problem, the current can be kept low enough, but it will decrease the overall SNR in the system.

The *1/f* noise is pervasive in all active and passive devices we use such as light sources and amplifiers. For example, a frequency noise of laser also shows *1/f* noise characteristic and causes performance degradation in sensing, laser spectroscopy, and laser gyroscopes. Thus, the laser frequency stabilization is important to reduce or avoid the *1/f* noise and can be achieved by the lock-in dithering technique through the molecular absorption line [116], [117] which is very similar to what we have shown in Chapter 4. Shay *et al*. [116] increased the frequency stability of laser by 10 times compare to a commercial GaAlAs free-running laser.

It is impossible to fundamentally eliminate the *1/f* noise, but we can expect to reduce it by a better process.

B.5 Relative Intensity Noise (RIN) of laser

Light source shows two types of noise; intensity and phase noise [38]. The phase noise is neglected because the intensity noise converted from the phase noise on the drop port signal is very small compare to other intensity noises in our biosensor [38]. Laser intensity noise refers to the noise generated by the laser and is induced by intensity fluctuations because of spontaneous emissions ideally, but operating conditions such as bias current, modulation frequency, coupling of laser cavity, and external feedback also directly affect the noise [119].

Definition of RIN is [120]

$$RIN = \frac{\left\langle (\Delta P)^2 \right\rangle}{P_L^2} dBc / Hz \tag{B.23}$$

Note that ΔP in (B.23) is not only caused by spontaneous emission this time. The current noise due to the RIN in rms manner is

$$\left\langle i_{RIN} \right\rangle = RP_L e^{-\alpha} \sqrt{(RIN)B} \tag{B.24}$$

We can also find SNR as,

$$\frac{v_s^2}{\left\langle v_{RIN}^2 \right\rangle} = \frac{i_s^2 R_L^2}{\left\langle i_{RIN}^2 \right\rangle R_L^2} = \frac{R_L^2 (RP_L)^2 e^{-2\alpha}}{R_L^2 (RP_L)^2 e^{-2\alpha} (RIN)B} = \frac{1}{(RIN)B} \tag{B.25}$$

which is simply the inverse of RIN.

Electrical spectrum analyzer (ESA) is widely used to measure the frequency spectrum but its frequency is usually available near radio frequency (RF) which is out of our sensor operation. The alternative method is taking advantage of the data acquisition (DAQ) board via the computer. The spectrum can be found after simple mathematics [121], and the calculation steps are shown below.

A measured voltage in time, $v(t)$, and its Fourier transform $V(f)$ are related by

$$V(f) = \int_{-\infty}^{\infty} v(t) e^{-i2\pi ft} dt \tag{B.26}$$

$$v(t) = \int_{-\infty}^{\infty} V(f) e^{i2\pi ft} df \tag{B.27}$$

Since T is finite number, discrete Fourier transform (DFT) of Eq. (B.26) needs to be reconsidered as

$$V_T(f) = \int_{-T/2}^{T/2} v(t)\, \mathrm{e}^{-i2\pi ft}\, dt \tag{B.28}$$

The averaged power from obtained photovoltage in timely manner is

$$P = \frac{1}{T}\int_{-T/2}^{T/2} \frac{|v(t)|^2}{R_L}\, dt = \frac{1}{TR_L}\int_{-T/2}^{T/2} \left\{ v(t) \left[\int_{-\infty}^{\infty} V_T(f) e^{-i2\pi ft} df \right] \right\} dt = \frac{1}{TR_L}\int_{-\infty}^{\infty} |V_T(f)|^2\, df \tag{B.29}$$

The power spectral density is defined from above expression

$$S(f) = \frac{2|V_T(f)|^2}{TR_L} \tag{B.30}$$

and an additional factor of 2 is multiplied in front of Eq. (B.30) since this is single-sided spectrum.

The plot shown in Figure 6.4 (a) is the schematic of experimental setup for RIN measurement. The battery operated ultra-low noise current source (LDX-3620B, ILX Lightwave, MT) was used to run DFB LD at 1.31 μm lasing wavelength (1612A , Emcore, NM) for minimal effects of pump induced noise. Large input noise ($200\ \mathrm{nV}/\sqrt{\mathrm{Hz}}$) of DAQ board (PCI-6281, National Instrument) limits the sensitivity of measurement, so the preamplifier is added after the photodetector to improve the sensitivity of measurement by reducing the overall noise figure. However, still the noise figure for preamplifier is 22.7 dB with the 50 Ω photodetector termination. To suppress

the noise figure down to 11.2 dB, the 1 kΩ impedance was used for the accurate measurement.

Dynamic range of RIN measurements is illustrated in Figure 6.4 (b), and we can see how each noise is affecting the system RIN as a function of photocurrent. The power density for 1 Hz bandwidth is calculated with 1 kΩ photodetector termination including shot, thermal, and instrument input noises we have discussed so far. The maximum SNR achievable can be found by considering detected average power (blue line) and total noise (red line). For 10 mA photocurrent, the dynamic range of RIN measurement was 164.9 dB. If the optical power incident on the photodetector is large enough, the shot noise power dominates the thermal noise and becomes the measurement limit. The shot-noise limit will have the same SNR in any lightwave systems.

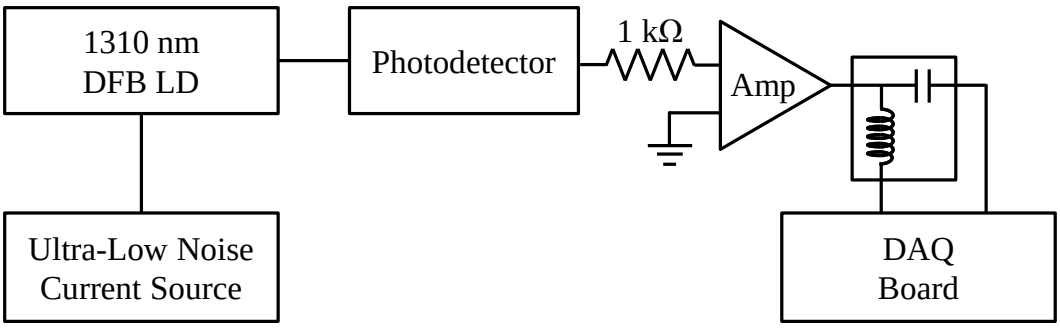

(a)

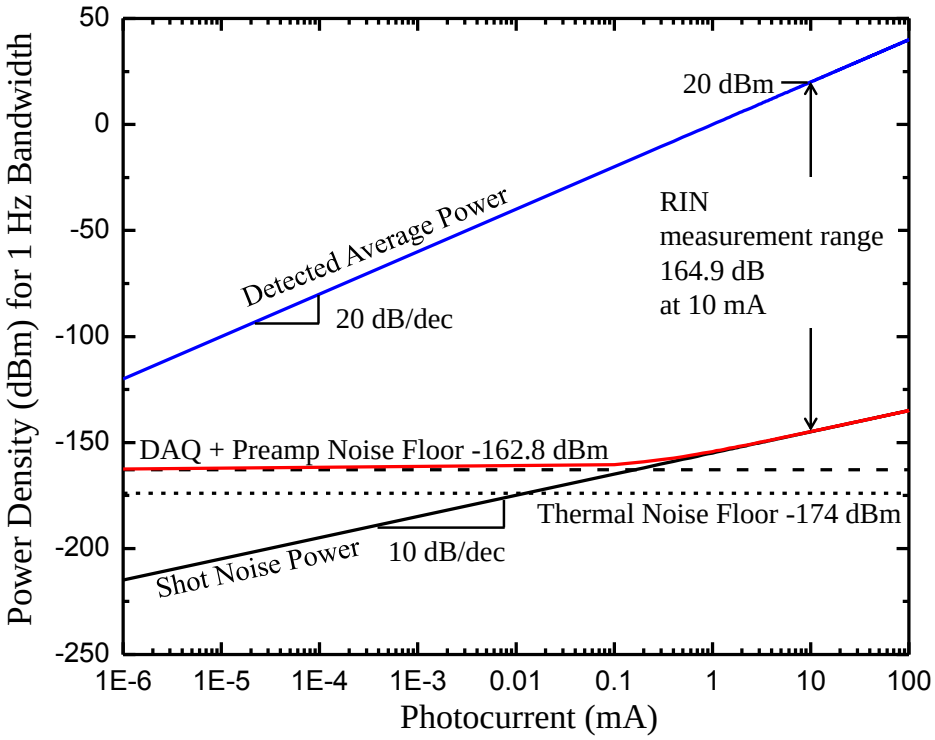

(b)

Figure 6.4. (a) Experimental setup for the RIN measurement using a DAQ board (b) Dynamic range of RIN measurement with 1 kΩ photodetector termination. RIN measurements are limited by shot noise, thermal noise, and total detected power.

The RIN spectrum is measured using the DAQ board a sampling rate of 300 kS/s when P_L =12 mW and plotted in Figure 6.5, with shot noise indicated by a red line. The system RIN includes all the noises from both transmitter and receiver. RIN spectrum shows significant reduction in noise at higher frequency because contribution from the *1/f* noise decreases, and it has flat white noise nearly -140 dBc/Hz. Spikes in spectrums are cause

by harmonics of in-line noise at 60 Hz. The calculated shot noise floor is -165 dBc/Hz, and we can say that the additional 25 dB penalty is due to the RIN of laser.

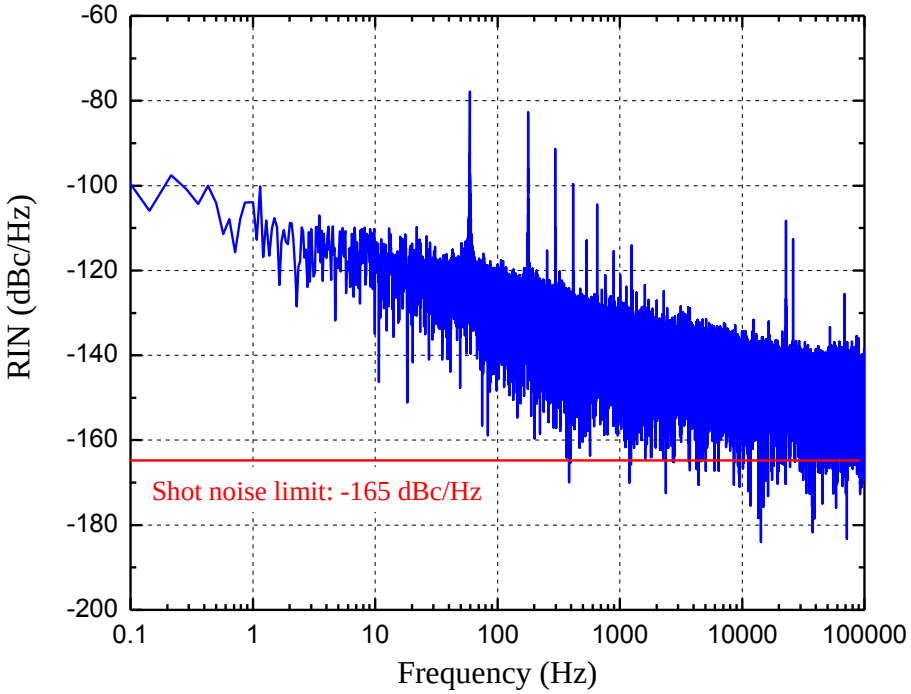

Figure 6.5. Measured RIN spectrum shown together with red lined shot noise limit of -164.8 dBc/Hz for P_L =12 mW. Noise near 20 kHz is transmitted trigger signals due to the finite isolation between DAQ channels.

B.6 Detector Noise

There are other noises associated with the photodiode itself which are dark current and noise equivalent power (NEP) [120].

Dark current is the noise generated in a photodetector in the absence of any optical signal and originates from the stray light or from thermally generated electron-hole pairs [107].

For a good photodetector, the dark current is very small (< 1nA). The problem of dark current is the fact that it also generates shot noise, but in our case the contributions are negligible compare to the signal induced shot noise, so that we do not consider in this thesis.

NEP is the minimum optical signal requires on a photodetector generating a photocurrent equal to the total photodiode noise current [122], and the photodetector we use have NEP of $1\ \mathrm{fW}/\sqrt{\mathrm{Hz}}$. This, also, negligible compare to other noises caused by signal level we use.

B.7 Total Noise

The SNR with total contribution of each noise in addition to instrument input noise is

$$\frac{v_s^2}{\langle v_N^2 \rangle} = \frac{i_s^2 R_L^2}{\langle i_N^2 \rangle R_L^2} = \frac{R_L^2 (RP_L)^2 e^{-2\alpha}}{R_L^2 (2ReP_L) B e^{-\alpha} + 4k_B T R_L B + R_L^2 (RP_L)^2 e^{-2\alpha} (RIN) B + R_L^2 \langle i_{1/f}^2 \rangle + \langle v_{input}^2 \rangle B} \tag{B.31}$$

The input noise of preamp we used is $6\ \mathrm{nV}/\sqrt{\mathrm{Hz}}$, and this is approximately the thermal noise from a 2 kΩ resistor. For the photodetector termination below 2 kΩ, noise will be dominated by the input noise of preamp, and hence we need to make sure to use the impedance larger than 2 kΩ. If we operate the sensor at high frequency, we can get rid of the *1/f* noise (Chapter 5), and the large input impedance overcomes the input noise of preamplifier. In this situation, Eq. (B.31) can be a simpler formulation

$$\frac{v_s^2}{\left\langle v_N^2 \right\rangle} \cong \frac{R_L (RP_L)^2 e^{-2\alpha}}{R_L (2ReP_L) B e^{-\alpha} + 4k_B TB + R_L (RP_L)^2 e^{-2\alpha} (RIN) B} \tag{B.32}$$

Bibliography

[1] D. W. Kimmel, G. LeBlanc, M. E. Meschievitz, and D. E. Cliffel, "Electrochemical Sensors and Biosensors," Anal. Chem., vol. 84, pp. 685–707 (2012).

[2] J. Wang, "Electrochemical biosensors: Towards point-of-care cancer diagnostics," Biosensors and Bioelectronics, vol. 21, pp. 1887–1892 (2006).

[3] "Biosensors in Medical diagnostics," Global Industry Analysts, Inc. (2011).

[4] X. Fan, I. M. White, S. I. Shopova, H. Zhu, J. D. Suter, and Y. Sun, "Sensitive optical biosensors for unlabeled targets: A review," Analytica Chimica Acta, vol. 620, pp. 8-26 (2008).

[5] J. Wang, "Electrochemical Glucose Biosensors," Chem. Rev., vol. 108, pp. 814-825 (2008).

[6] "Screening for Type 2 Diabetes," Report of a World Health Organization and International Diabetes Federation meeting, Geneva (2003).

[7] J. A. Wells and C. L. McClendon, "Reaching for high-hanging fruit in drug discovery at protein-protein interfaces," Nature, vol. 450, pp. 1001-1009 (2007).

[8] J. Park , J. Yang, G. Lee, C. Y. Lee, S. Na, S. W Lee, S. Haam, Y. -M. Huh, D. S. Yoon, K. Eom, T. Kwon, "Single-Molecule Recognition of Biomolecular Interaction via Kelvin Probe Force Microscopy," ACS Nano, vol. 5, pp. 6981-6990 (2011).

[9] P. M. Dean, E. D. Zanders and D. S. Bailey, "Industrial-scale, genomics-based drug design and discovery," TRENDS in Biotechnology, vol. 19, pp. 228-292 (2001).

[10] J. L. Arlett, E. B. Myers, and M. L. Roukes, "Comparative advantages of mechanical biosensors," Nature Nanotechnology, vol. 6, pp. 203-215 (2011).

[11] V. M. N. Passaro, F. Dell'Olio, B. Casamassima, and F. D. Leonardis, "Guided-Wave Optical Biosensors," Sensors, vol. 7, pp. 508-536 (2007).

[12] A. M. Armani, R. P. Kulkarni, S. E. Fraser, R. C. Flagan, and K. J. Vahala, "Label-Free, Single-Molecule Detection with Optical Microcavities," Science, vol. 317, pp. 783-786 (2007).

[13] J. Hartigan, C. Liu and W. Downey, "Moving forward with label-free technology", Drug Discovery World, Winter Edition, pp. 41-48 (2010).

[14] H. -S. P. Wong, D. J. Frank, P. M. Solomon, C. H. J. Wann, J. J. Welser, "Nanoscale CMOS," Proceedings of the IEEE, vol. 87, pp. 537-570 (1999).

[15] F. Tavernier and M. Steyaert, "High-Speed Optical Receivers with Integrated Photodiode in Nanoscale CMOS," Springer, New York (2011).

[16] B. Jalali, S. Yegnanarayanan, T. Yoon, T. Yoshimoto, I. Rendina, and F. Coppinger, "Advances in Silicon-on-Insulator Optoelectronics," JSTQE, IEEE, vol. 4, pp. 938-947 (1998).

[17] A. Densmore, D. -X. Xu, P. Waldron, S. Janz, P. Cheben, J. Lapointe, A. Delâge, B. Lamontagne, J. H. Schmid, and E. Post, "A silicon-on-insulator photonic wire based evanescent field sensor," IEEE Photon. Technol. Lett., vol. 18, pp. 2520-2522 (2006).

[18] M. Iqbal, M. A. Gleeson, B. Spaugh, F. Tybor, W. G. Gunn, M. Hochberg, T. Baehr-Jones, R. C. Bailey, and L. Cary Gunn, "Label-Free Biosensor Arrays Based on Silicon Ring Resonators and High-Speed Optical Scanning Instrumentation," JSTQE, IEEE, vol. 16, pp. 654-661 (2010).

[19] D. -X. Xu, M. Vachon, A. Densmore, R. Ma, A. Delâge, S. Janz, J. Lapointe, Y. Li, G. Lopinski, D. Zhang, Q. Y. Liu, P. Cheben, and J. H. Schmid, "Label-free biosensor array based on silicon-on-insulator ring resonators addressed using a WDM approach," Opt. Lett. vol. 35, pp. 2771-2773 (2010).

[20] J. Hu and D. Da, "Cascaded-Ring Optical Sensor With Enhanced Sensitivity by Using Suspended Si-Nanowires," PTL, IEEE, vol. 23, pp. 842-844 (2011).

[21] M. A. Webster, R. M. Pafchek, A. Mitchell, and T. L. Koch, "Width Dependence of Inherent TM-Mode Lateral Leakage Loss in Silicon-On-Insulator Ridge Waveguides," PTL, IEEE, vol. 19, pp. 429-431 (2007).

[22] J. P. R. Lacey and F. P. Payne, "Radiation loss from planar waveguides with random wall imperfections," IEE Proceedings J. Optoelectronics, vol. 137, p. 282-288 (1990).

[23] J. Comley, "Progress in the implementation of LABEL-FREE DETECTION, part 2: binding analysis assays," Drug Discovery World, Fall Edition, pp. 28-49 (2008).

[24] X. D. Hoa, A. G Kirk, M. Tabrizian, "Towards integrated and sensitive surface plasmon resonance biosensors: A review of recent progress," Biosens. Bioelectron., vol. 23, pp. 151-160 (2007).

[25] GE Healthcare Ltd., Chalfont St. Giles, Buckinghamshire, United Kingdom, www.gehealthcare.com

[26] D. Harrison, H. Kjellberg, "Segmenting a market in the making: Industrial market segmentation as construction," Ind. Mark. Manage. vol. 39, pp. 784-792 (2010).

[27] M. A. Cooper, "Optical biosensors in drug discovery," Nature Reviews Drug Discovery vol. 1, pp. 515-528 (2002).

[28] S. Arnold, M. Khoshima, I. Teraoka, S. Holler, and F. Vollmer, "Shift of whispering-gallery modes in microspheres by protein adsorption," OSA Opt. Lett. , vol. 28, pp. 272–274 (2003).

[29] N. Hanumegowda, C. Stica, B. Patel, I. White, and X. Fan, "Refractometric sensors based on microsphere resonators," Apl. Phys. Lett. , vol. 87, pp. 201107 (2005).

[30] A. Armani, R. Kulkarni, S. Fraser, R. Flagan, and K. Vahala, "Label-free, single-molecule detection with optical microcavities," Science, vol. 213, pp. 783–787, (2007).

[31] R. Boyd and J. Heebner, "Sensitive disk resonator photonic biosensor," OSA Appl. Opt. , vol. 40, pp. 5742–5747 (2001).

[32] E. Krioukov, D. Klunder, A. Driessen, C. Otto, and J. Greve, "Sensors based on an integrated optical microcavity," OSA Opt. Lett. , vol. 27, pp. 512–514 (2002).

[33] T. Lu, H. Lee, T. Chen, S. Herchak, J. -H. Kim, S. E. Fraser, R. C. Flagan, and K. Vahala, "High sensitivity nanoparticle detection using optical microcavities," PNAS, vol. 108, pp. 5976-5979 (2011).

[34] Y. Guo, C. Divin, A. Myc, F. L. Terry Jr. , J. R. Baker Jr. , T. B. Norris, and J. Y. Ye, "Sensitive molecular binding assay using a photonic crystal structure in total internal reflection," Opt. Express, vol. 16, pp. 11741-11749 (2008).

[35] Genalyte Inc., 3030 Bunker Hill St., San Diego, CA 92109, USA, www.genalyte.com

[36] S. P. Mohanty and E. Kougianos, "Biosensors: A tutorial review," IEEE Potentials vol. 25, pp. 35-40 (2006).

[37] D. -X. Xu, M. Vachon, A. Densmore, R. Ma, S. Janz, A. Delâge, J. Lapointe, P. Cheben, J. H. Schmid, E. Post, S Messaoudène, and J. -M. Fédéli, "Real-time cancellation of temperature induced resonance shifts in SOI wire waveguide ring resonator label-free biosensor arrays," Optics Express, vol. 18, pp. 22867-22879 (2010).

[38] I. M. White and X. Fan, "On the performance quantification of resonant refractive index sensors," Optics Express, vol. 16, pp. 1020-1028 (2008).

[39] C. Gunn and T. L. Koch, "Silicon photonics," in Optical Fiber Communications: Components and Subsystems, vol. 5, Elsevier Inc. , Oxford (2008).

[40] A. Densmore, D. -X. Xu, S. Janz, P. Waldron, J. Lapointe, T. Mischki, G. Lopinski, A. Delâge, J. H. Schmid, and P. Cheben, "Sensitive Label-Free Biomolecular Detection Using Thin Silicon Waveguides," Advances in Optical Technologies, vol. 2008, Article ID 725967, 9 pages, (2008).

[41] R. M. Pafchek, R. S. Tummidi, J. Li, M. A. Webster, E. Chen and T. L. Koch, "Low-loss SOI Shallow-Ridge TE and TM Waveguides Formed Using Thermal Oxidation," Applied Optics, vol. 48, pp. 958-963 (2009).

[42] G. P. Agrawal, "Fiber-Optic Communication Systems," 3rd edition, Wiley-Interscience, New York (2002).

[43] L. Kou, D. Labrie, and P. Chylek , "Refractive indices of water and ice in the 0. 65- to 2.5-μm spectral range," Applied Optics, vol. 32, pp. 3531-3540 (1993).

[44] M. A. Webster , R. M. Pafchek, A. Mitchell, and T. L. Koch, "Experimental observation of precision widths mitigating inherent leakage in silicon-on-insulator ridge waveguides," IEEE LEOS Annual Meeting, Montreal, Canada, Post-Deadline Paper PD 1. 5 (2006).

[45] S. T. Peng, and A. A. Oliner, "Guidance and Leakage Properties of a Class of Open Dielectric Waveguides: Part I-Mathematical Formulations," IEEE Transactions on Microwave Theory and Techniques, vol. 29, pp. 843-855 (1981).

[46] A. A. Oliner, S. T. Peng, T. I. Hsu, and A. Sanchez, "Guidance and Leakage Properties of a Class of Open Dielectric Waveguides: Part II--New Physical Effects," Microwave Theory and Techniques, IEEE Transactions on, vol. 29, pp. 855- 869 (1981).

[47] K. Ogusu, "Optical strip waveguide-A detailed analysis including leaky modes," Optical Society of America, Journal, vol. 73, pp. 353-357 (1983).

[48] Comsol, Inc., 1 New England Executive Park, Suite 350,Burlington, MA 01803, USA, www.comsol.com

[49] Soitec S.A., Parc Technologique Des Fontaines, Bernin 38190, France, www.soitec.com

[50] G. T. Reed and A. P. Knights, "Silicon Photonics: An Introduction," John Wiley & Sons, Hoboken (2004).

[51] American Dicing Inc., 7845 Maltlage Dr., Liverpool, NY, USA, www.americandicing.com

[52] D. T. Eddington, J. P. Puccinelli, and D. J. Beebe, "Thermal aging and reduced hydrophobic recovery of polydimethylsiloxane," Sensors and Actuators B, vol. 114, pp. 170-172 (2006).

[53] A. Yariv, "Universal relations for coupling of optical power between microresonators and dielectric waveguides," Electronics Letters, vol. 36, pp. 321-322 (2000).

[54] RSoft Design Group Inc., 400 Executive Boulevard, Suite 100, Ossining, NY 10562, USA, www.rsoftdesign.com

[55] H. Kogelnik, "Theory of dielectric waveguides," in Integrated Optics, Springer-Verlag, Berlin (1975).

[56] B. J. Frey, D. B. Leviton, T. J. Madison, "Temperature-dependent refractive index of silicon and germanium," Proceedings of the SPIE, Volume 6273, pp. 62732J (2006).

[57] P. Schiebener, J. Straub, J. M. H. Levelt Sengers, and J. S. Gallagher, "Refractive index of water and steam as function of wavelength, temperature and density," J. Phys. Chem. Ref. Data, vol. 19, pp. 677-717 (1990).

[58] C. -Y. Chao, W. Fung, and L. J. Guo. "Polymer Microring Resonators for Biochemical Sensing Applications," JSTQE, IEEE, vol. 12, pp. 134-142 (2006).

[59] G. G. Nenninger, P. Tobĭska, J. Homola, S. S. Yee, "Long-range surface plasmons for high-resolution surface plasmon resonance sensors," Sens. Actuators B Chem. vol. 74, pp. 145-151 (2001).

[60] R. Slavík, J. Homola, "Ultrahigh resolution long range surface plasmon-based sensor," Sens. Actuators B Chem. vol. 123, pp. 10-12 (2007).

[61] Y. Wang, H. Li, Z. Cao, T. Yu, Q. Shen, and Ying He, "Oscillating wave sensor based on the Goos–Hänchen effect," Appl. Phys. Lett. vol. 92, 061117 (2008)

[62] N. M. Hanumegowda, C. J. Stica, B. C. Patel, I. M. White, and X. Fan, "Refractometric sensors based on microsphere resonators," Appl. Phys. Lett. vol. 87, 201107 (2005).

[63] P. Klocek, "Handbook of infrared optical materials," Marcel Dekker, New York (1991).

[64] Pochi Yeh, "Optical Waves in Layered Media," John Wiley & Sons, Hoboken (1998).

[65] K. Kim, R. M. Pafchek, and T. L. Koch, "Athermal silicon waveguides for aqueous evanescent biosensor applications," WD4, Photonics Conference (PHO), IEEE (2011).

[66] M. M. Milošević, N. G. Emerson, F. Y. Gardes, X. Chen, A. A. D. T. Adikaari, and G. Z. Mashanovich, "Athermal waveguides for optical communication wavelengths," Opt. Lett. , vol. 36, pp. 4659-4661 (2011).

[67] J. Teng, P. Dumon, W. Bogaerts, H. Zhang, X. Jian, X. Han, M. Zhao, G. Morthier, and R. Baets, "Athermal Silicon-on-insulator ring resonators by overlaying a polymer cladding on narrowed waveguides," Opt. Express, vol. 17, pp. 14627-14633 (2009).

[68] K. Kim, R. M. Pafchek, and T. L. Koch, "Demonstration and analysis of the harmonic dithering technique for a high-sensitivity silicon waveguide biosensor," APS March Meeting (2012).

[69] P. Correc, O. Girard,and, and I. F. de Faria, Jr., "On the Thermal Contribution to the FM Response of DFB Lasers: Theory and Experiment," IEEE JOURNAL OF QUANTUM ELECTRONICS, vol. 30, pp. 2485-2490 (1994).

[70] G. Jacobsen, H. Olesen, F. Birkedahl and B. Tromsborg, "Current/frequency-modulation characteristics for directly optical frequency modulated injection lasers at 830nm and 1. 3μm", Elec. Lett. , vol. 18, pp. 874-876 (1982).

[71] R. W. M. Smith, I. L. Freeston, B. H. Brown, and A. M. Sinton, “Design of a phase-sensitive detector to maximize signal-to-noise ratio in the presence of Gaussian wideband noise,” Meas. Sci. Technol. , vol. 3, pp. 1054-1062 (1992).

[72] S. K. Sengupta , J. M. Farnham and J. E. Whitten, “A Simple Low-Cost Lock-In Amplifier for the Laboratory. ” J. Chem. Educ. , vol. 82, p 1399-1401 (2005).

[73] Y. Guo, J. Y. Ye, C. Divin, B. Huang, T. P. Thomas, J. R. Baker, Jr. and T. B. Norris, "Real-Time Biomolecular Binding Detection Using a Sensitive Photonic Crystal Biosensor," Anal. Chem. , vol 82 , pp 5211–5218 (2010).

[74] M. S. T Goncalves, “Fluorescent labeling of biomolecules with organic probes. ” Chem. Rev. , vol. 109, pp. 190-212 (2009).

[75] S. Ray, G. Mehta, and S. Srivastava, “Label-free detection techniques for protein microarrays: Prospects, merits and challenges,” Proteomics, vol. 10, pp. 731-748 (2010).

[76] New Era Pump Systems Inc., 2517 Bayview Ave, Wantagh, NY 11793, www.syringepump.com

[77] M. -E. Brett, S. Zhao, J. L. Stoia, and D. T. Eddington, “Controlling flow in microfluidic channels with a manually actuated pin valve,” Biomed. Microdevices, vol. 13, pp. 633-639 (2011).

[78] A. Günther and M. T. Kreutzer, “Fluid Dynamics in Microchannels,” Micro Process Engineering: A Comprehensive Handbook, Wiley-VCH, Weinheim (2009).

[79] VALCO INSTRUMENTS COMPANY, INC., 7811 Westview Dr. Houston, TX 77055, USA, www.vici.com

[80] H. Gai, L. Yu, Z. Dai, Y. Ma, and B. Lin, "Injection by hydrostatic pressure in conjunction with electrokinetic force on a microfluidic chip," ELECTROPHORESIS, vol. 25, pp. 1888-1894 (2004).

[81] J. A. Woollam Co., 645 M St., Lincoln, NE 68508, USA, www.jawoollam.com

[82] Thermo Scientific, Protein Methods Library > Avidin-Biotin Interaction, www. piercenet. com

[83] T. Sano, G. Reznik, S. Vajda, C. R. Cantor and C. L. Smith, "Properties and Applications of Genetically Engineered Streptavidins," Scientific and Clinical Applications of Magnetic Carriers, Plenum Press, New York, pp. 295-301 (1997).

[84] J. N. Herron, W. Mueller, M. Paudler, H. Riegler, H. Ringsdorf, and P. A. Suci, "Specific recognition-induced self-assembly of a biotin lipid/streptavidin/Fab fragment triple layer at the air/water interface: ellipsometric and fluorescence microscopy investigations," Langmuir, vol. 8, pp. 1413–1416 (1992).

[85] Y. Guo, J. Y. Ye, C. Divin, T. P. Thomas, A. Myc, T. F. Bersano-Begey, J. R. Baker, Jr. , and T. B. Norris, "Label-free biosensing using a photonic crystal structure in a total-internal-reflection geometry," Proc. SPIE, vol. 16, pp. 71880B–71880B12 (2009).

[86] V. Prez-Luna, M. O'Brien, K. Opperman, P. Hampton, G. Lpez, L. Klumb, and P. Stayton, "Molecular recognition between genetically engineered streptavidin and surface-bound biotin," J. M. Chem. Soc., vol. 27, pp. 6469–6478 (1999).

[87] R. P. Haugland and W. W. You, "Coupling and Antibodies With Biotin," Avidin-Biotin Interactions: Methods and Applications, pp. 13-23, Springer, Clifon (2008)

[88] R. M. A. Azzam and N. M. Bashara, "Ellipsometry and Polarized Light," North-Holland PL (1987).

[89] U. Böhme and U. Scheler, "Effective charge of bovine serum albumin determined by electrophoresis NMR," Chem. Phys. Lett. , vol. 435, pp. 342–345 (2007).

[90] D. S. Karpovich and G. J. Blanchard, "Direct Measurement of the Adsorption Kinetics of Alkanethiolate Self-Assembled Monolayers on a Microcrystalline Gold Surface," Langmuir, vol. 10, pp. 3315-3322 (1994).

[91] J. S. Shurnaker-Parry and C. T. Campbell, "Quantitative methods for spatially resolved adsorption/desorption measurements in real time by surface plasmon resonance microscopy," Anal. Chem., vol. 76, pp. 907-917 (2004).

[92] L. S. Jung, K. E. Nelson, P. S. Stayton, and C. T. Campbell, "Binding and dissociation kinetics of wild-type and mutant streptavidins on mixed biotin-containing alkylthiolate monolayers," Langmuir, vol. 16, pp. 9421-9432 (2000).

[93] R.-B. Jiang and U. Lei "Biosensor regeneration via substrate electric potential: A physical mechanism," Appl. Phys. Lett., vol. 96, pp. 263701 (2010).

[94] ILX Lightwave Corporation, 31950 E. Frontage Rd., Bozeman, MT 59715, www.ilxlightwave.com

[95] C. K. Laue, R. Knappe, K. -J. Boller, and R. Wallenstein, "Wavelength tuning and spectral properties of distributed feedback diode lasers with a short external optical cavity," Applied Optics, vol. 40, pp. 3051-3059 (2001).

[96] J. Homola, "Surface Plasmon Resonance Sensors for Detection of Chemical and Biological Species," Chem. Rev. , vol. 108, pp. 462-493 (2008).

[97] P. Pilla, V. Malachovská, A. Borriello, A. Buosciolo, M. Giordano, L. Ambrosio, A. Cutolo, and A. Cusano, "Transition mode long period grating biosensor with functional multilayer coatings," Opt. Express, vol. 19, pp. 512-526 (2011).

[98] K. Zinoviev, L. G. Carrascosa, J. S. Rio, M. Moren, F. J. Blanco, K. Mayora, C. Domiınguez, and L. M. Lechuga, "Optical biosensor microsystems based on the integration of highly sensitive Mach–Zehnder interferometer devices," J. Opt. A: Pure Appl. Opt. vol. 8, pp. 561–566 (2006).

[99] L. Chen, P. Dong, and M. Lipson, "High performance germanium photodetectors integrated on submicron silicon waveguides by low temperature wafer bonding," Optics Express, vol. 16, pp. 11513-11518 (2008).

[100] J. O. Wilkes and S. G. Bike, "Fluid Mechanics for Chemical Engineers with Microfluidics and CFD," 2nd ed, Prentice Hall PTR, Upper Saddle River (2005).

[101] C. D. Motchenbacher and J. A. Connelly , "Low-noise electronic design," John Wiley & Sons, New York (1973).

[102] B. Carter, "Op Amp Noise Theory and Applications," Op Amps for Everyone, 3rd edition, Newnes, Boston (2009).

[103] F. N. Hooge, T. G. M. Kleinpenning, and L. K. J. Vandamme, "Experimental studies on 1/f noise," Rep. Prog. Phys., vol. 44, pp. 479-532 (1981).

[104] B. O. Nilsson, "Noise Mechanism in Laser Diodes," IEEE Transactions on Electron Devices, vol. 41, pp. 2139-2150 (1994).

[105] J. Chesnoy, "Undersea fiber communication systems," Academic Press, Boston (2002).

[106] P. B. Gallion, "Classical phase-amplitude description of optical amplifier noise: application to noise figure derivation for distributed optical amplifiers," Proc. SPIE 5260, 96 (2003).

[107] T. L. Koch, "Class notes for Lehigh University Course ECE 450 and PHY 497, Optoelectronics Physics and Lightwave Technology II," Unpublished.

[108] W. M. Leach, Jr., "Fundamentals of Low-Noise Analog Circuit Design," Proc. of IEEE, vol. 82, pp. 1515-1538 (1994).

[109] F. N. Hooge, "*1/f* noise is no surface effect," Physics Letters A, vol. 29, pp. 139-140 (1969).

[110] Y. Nemirovsky, I. Brouk, and C. G. Jakobson, "1/f Noise in CMOS Transistors for Analog Applications," IEEE TRANSACTIONS ON ELECTRON DEVICES, vol. 48, pp. 921-927 (2001).

[111] K. K. Hung, P. K. Ko, C. Hu, and Y. C. Cheng, "A unified model for the flicker noise in metal-oxide-semiconductor field-effect transistors," Electron Devices, IEEE Transactions on, vol. 37, pp. 654-665 (1990).

[112] J. Zheng, "Optical frequency-modulated continuous-wave (FMCW) interferometry," Springer, New York (2005).

[113] Philip G. Collins, M. S. Fuhrer, and A. Zettl, "1/f noise in carbon nanotubes," Appl. Phys. Lett., vol. 76, pp.894-896 (2000).

[114] S. Demolder, M. Vandendriessche and A. V. Calster, "The measuring of l/f noise of thick and thin film resistors," J. Phys. E: Sci. Instrum., vol. 13, pp. 1323-1327 (1980).

[115] M. Ahmed, M. M. Chitteboyina, D. P. Butler, and Z. Celik-Butler, "Temperature sensor in a flexible substrate," Sensors Journal, IEEE, 5324 (2011).

[116] T. M. Shay and Y. C. Chung, "400 Hz frequency stability of a GaAlAs laser frequency locked to the Rb (D_2) line," Optical Engineering, vol. 29, pp. 681-683 (1990).

[117] D. S. Bomse, "Dual-modulation laser line-locking scheme," Applied Optics, vol. 30, pp. 2922-2924 (1991).

[118] C. H. Henry and R. F. Kazarinov, "Quantum noise in photonics," Rev. Mod. Phys. vol. 68, pp. 801–853 (1996).

[119] R. Paschotta, "Encyclopedia of laser physics and technology," Wiley-VCH, Weinheim (2008).

[120] P. W. Milonni and J. H. Eberly, "Laser Physics," John Wiley & Sons, Hoboken (2010).

[121] A. Yariv, "Optical Electronics in Modern Communcations," 5th edition, Oxford, New York (1997).

[122] P. L. Richards, "Bolometers for infrared and millimeter waves," Journal of Applied Physics, vol. 76, pp. 1-24 (1994).

KANGBAEK KIM, PH.D.

7 Asa Dr., Sinclair Laboratory, Lehigh University, Bethlehem, PA 18015
kak207@lehigh.edu • +1-610-758-2896 • http://www.linkedin.com/in/kangbaek

- Optical system design for fast and accurate 3D measurements
- CMOS/III-V nano-photonic and optoelectronic device design, fabrication, and characterization for optical telecommunication and biosensor applications

RESEARCH AND PROFESSIONAL EXPERIENCES

FARO Technologies
Optical Systems Engineer **Apr 2012 - Present**

- Performing functions to develop, model, and design 3D laser scanning measurement systems and products
- Strong knowledge of solid state physics and CCD camera readout systems

Center for Optical Technologies, Lehigh University
Research Assistant **Aug 2007 – Mar 2012**

- Laid out 6″ mask design and fabrication for CMOS waveguides
- Researched high-performance silicon photonic biosensor on ring resonator
- Developed athermal SOI waveguide biosensors
- Demonstrated a low-noise measurement platform, the harmonic dithering feedback technique (optical servo)
- Expertise in photonic device modeling using Matlab, RSOFT, Mathematica, and C/C++
- Skillful in computer-controlled instrumentation and computer-based data acquisition

Hanyang University, Korea
Research Assistant **Mar 2006 – May 2007**

- Performed extensive modeling and characterization of InP MQW EAMs
- Development of GUI simulator for lithography fabrication process and RCWA based mask pattern analysis

EDUCATION

- Ph.D., Lehigh University, 2012
- B.S., Hanyang University, Korea, 2006

JOURNAL AND CONFERENCE PUBLICATIONS

- K. Kim, R. M. Pafchek, and T. L. Koch, ***Label-free biosensors based on athermal silicon-on-insulator waveguides and a harmonic dithering technique***, CTh4L.7, CLEO (2012)

- K. Kim, R. M. Pafchek, and T. L. Koch, ***Athermal Silicon Waveguides for Aqueous Evanescent Biosensor Applications***, WD4, IEEE Photonics Conference (2011)
- K. Kim and D.-S. Shin, ***Sensitivities of the InGaAs/InGaAsP/InGaAsP Intrastep Quantum Well to Thickness and Composition Variations for Realizing Efficient Electroabsorption Modulators***, Jpn. J. Appl. Phys., vol. 47, pp. 6361-6363 (2008)
- K. Kim and D.-S. Shin, ***Comparison of Quantum Wells based on InGaAs(P)/InP and InGa(Al)As/InAlAs Material Systems in View of Carrier Escape Times for High-saturation-Optical-Power Electroabsorption Modulators***, J. Opt. Soc. Korea, vol. 11, pp. 133-137 (2007)
- K. Kim, D.-S. Shin, Y.-D. Chung, K.-S. Choi, J.-S. Sim, and J. Kim, ***Improving the Noise Figure of the 60-GHz Radio-over-Fiber System using a System-on-Package EAM Module with Two-Stage LNAs***, Microwave Photonics, 2007 IEEE International Topical Meeting on
- K. Kim, S. H. Hwang, D.-S. Shin, Y.-D. Chung, K.-S. Choi, and J. Kim, ***Analysis of the Noise Figure for the 60-GHz Radio-over-Fiber Links***, Tech. Digest 2007 Asia-Pacific Microwave Photonics Conference